High Frequency Injection Sensorless Control for a Permanent Magnet Synchronous Machine Driven by an FPGA Controlled SiC Inverter

A Thesis Presented for the

Master of Science

Degree

The University of Tennessee, Knoxville

Jared D. Walden

August 2021

ACKNOWLEDGEMENTS

I am very grateful to all who enabled me to achieve my academic and career goals. I have been blessed with loving and supportive people throughout my academic career, and I have been encouraged by so many. My parents have always invested and believed in me, making engineering an enjoyable pursuit. My brothers have been amazing role models who have always encouraged me to be the best version of myself. Finally, my wife has supported me so well along this journey every step of the way and will always be my better half.

Three exceptional electrical engineers and scholars have been incredibly influential in my academic career, each at different periods of time in my life. The late John Newman sparked my interest in electrical engineering at a young age; Dr. Farhad Ashrafzadeh provided mentorship during my undergraduate experience that I will forever hold tight; and Dr. Hua Bai has contributed significantly to my future career as a power electronics engineer while in graduate school at the University of Tennessee - Knoxville.

I would also like to thank CURENT for the support provided to students at the University of Tennessee – Knoxville and Dr. Leon Tolbert for the opportunity provided by the Wide Bandgap Traineeship. Additionally, I want to extend my gratitude to the graduate students, Yang Huang, Yu Yan, Ziwei Liang, Kamal Sabi, Quillen Blalock, Jared Baxter, and Andrew Foote for the wisdom and friendship each has provided me.

ABSTRACT

As motor drive inverters continue to employ Silicon Carbide (SiC) and Gallium Nitride (GaN) devices for power density improvements, sensorless motor control strategies can be developed with field-programmable gate arrays (FPGA) to take advantage of high inverter switching frequencies. Through the FPGA's parallel processing capabilities, a high control bandwidth sensorless control algorithm can be employed. Sensorless motor control offers cost reductions through the elimination of mechanical position sensors or more reliable electric drive systems by providing additional position and speed information of the electric motor. Back electromotive force (EMF) estimation or model-based methods used for motor control provide precise sensorless control at high speeds; however, they are unreliable at low speeds. High frequency injection (HFI) sensorless control demonstrates an improvement at low speeds through magnetic saliency tracking. In this work, a sinusoidal and square-wave high frequency injection sensorless control method is utilized to examine the impact an interior permanent magnet synchronous machine's (IPMSM) fundamental frequency, injection frequency, and switching frequency have on the audible noise spectrum and electrical angle estimation. The audible noise and electrical angle estimation are evaluated at different injection voltages, injection frequencies, switching frequencies, and rotor speeds. Furthermore, a proposed strategy for selecting the proper injection frequency, injection voltage, and switching frequency is given to minimize the electrical angle estimation error.

TABLE OF CONTENTS

LIST OF TABLES

LIST OF FIGURES

CHAPTER ONE

INTRODUCTION

Electric Vehicle Traction Inverters

As the demand for electric vehicles (EV) and hybrid electric vehicles (HEV) continues to increase, the need for high power density motor drive inverters is paramount. According to the Department of Energy (DOE) Office of Energy Efficiency and Renewable Energy (EERE), the power density of electric drives should be increased tenfold by 2025 compared to 2015 specifications while the cost should be reduced by half; furthermore, the lifetime of the drive system should be doubled [1]. When looking at more recent targets, the net change from 2020 to 2025 includes an 18% cost reduction and an improvement of 86% in power density. Technical targets for the main traction inverter's power electronics are presented in Table 1.1. HEV and EV traction inverters are composed of several components: power semiconductor devices; semiconductor gate drivers; DC link capacitors; current, voltage, and temperature sensors; control unit; and heat sinks. Also, a DC-DC boost converter may be included to meet the voltage demand of the attached electric motor if the battery voltage is too low. Figure 1.1 displays a high-voltage EV traction inverter from Eaton Corporation [2]. To complete the full traction drive system, a single traction drive electric motor is included. Table 1.2 compares the DOE technical targets between 2020 and 2025.

Table 1.1. Technical Targets for EV High Voltage Power Electronics [3]

Parameter	2015 Target	2020 Target	2025 Target
Cost	≤$5/kW	≤$3.3/kW	≤$2.7/kW
Power Density	≥10 kW/liter	≥13.4 kW/liter	≥100 kW/liter

Table 1.2. Electric Drive System Technical Targets [3]

Parameter	2020 Target	2025 Target
Cost	≤$8/kW	≤$6/kW
Power Density	≥4 kW/liter	≥33 kW/liter

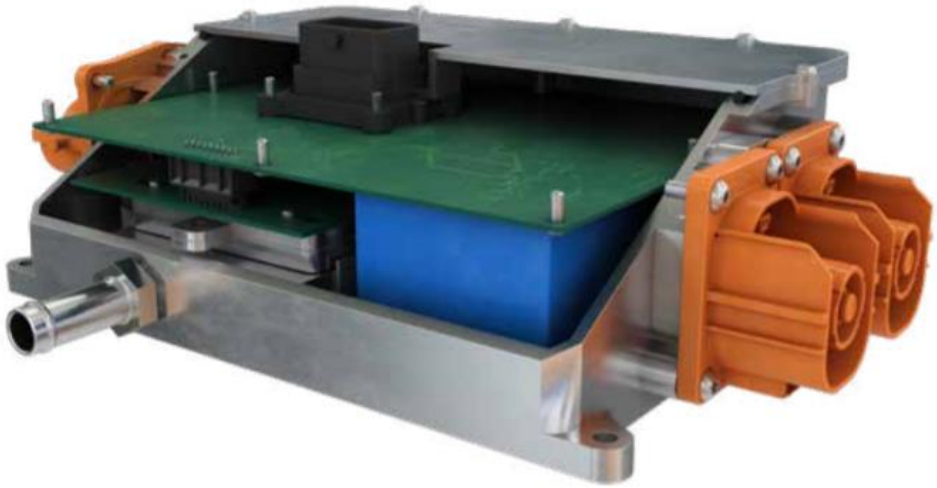

Figure 1.1. Eaton Corporation High-Voltage Traction Inverter [2]

There is a 25% cost reduction from 2020 to 2025 and there is an 88% volume reduction. A block diagram is presented on the next page in Figure 1.2 to show the fully integrated electric motor drive system [4]. The inverter is controlled with gate drive circuitry to command the operation of each power semiconductor device; this is labeled as the driving stage in Figure 1.2, allowing each of the power devices to create a conducting current channel or block an external voltage. A high-voltage battery pack provides a voltage source for the three phase DC/AC inverter, which is then connected to the electric motor from the three phase terminals, as shown in Figure 1.3. To complete the control loop, current and position signals are obtained from the electric motor through mechanical position sensors and are then processed by the onboard microcontroller (MCU). Current sensing and signal conditioning circuits may be used to create a readable signal for the MCU, which is the main part of the control unit. Figure 1.3 references a three-phase inverter with insulated-gate bipolar transistors (IGBT). Typical traction inverters that will operate at a switching frequency near or below 10 kHz employ IGBT power modules to meet high-voltage and high-current demands. However, the IGBT turn-off transition exhibits a phenomenon known as current tailing [5]. Current tailing leads to a longer turn-off time, increasing associated switching losses. This characteristic makes IGBT power modules at high switching frequencies undesirable. An example of IGBT switching losses can be seen in Figure 1.4. The shaded region in Figure 1.4 demonstrates the switching losses due to current tailing.

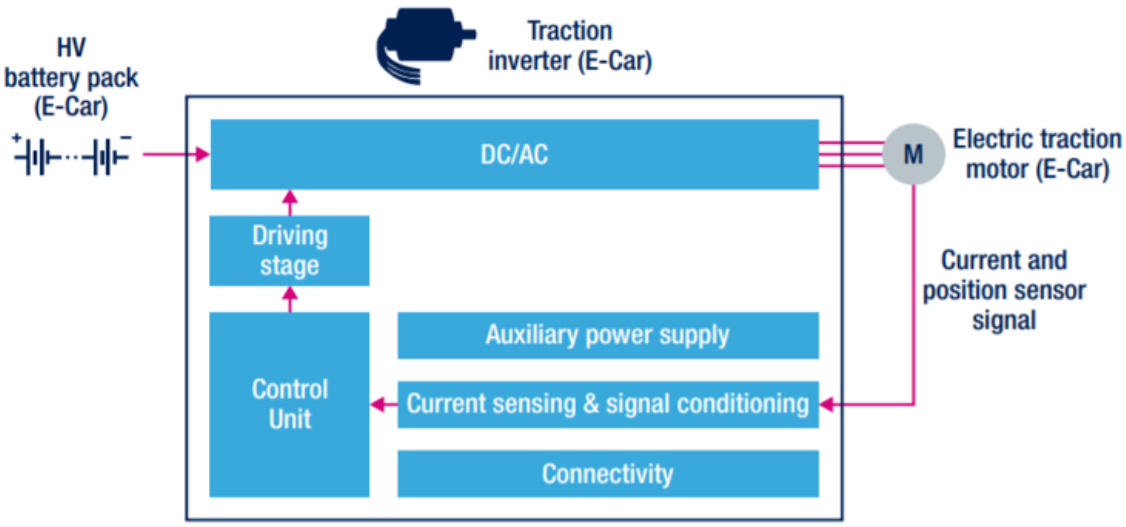

Figure 1.2. Electric Drive System Diagram (STMicroelectronics) [4]

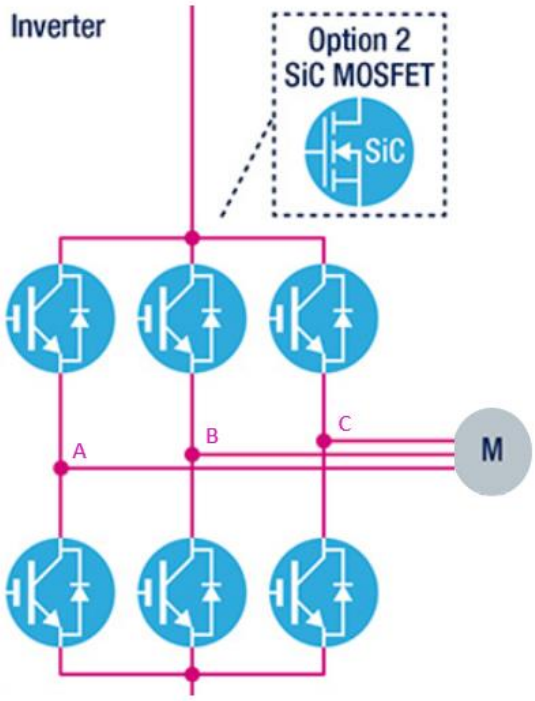

Figure 1.3. Three Phase Inverter Power Semiconductor Devices (STMicroelectronics) [4]

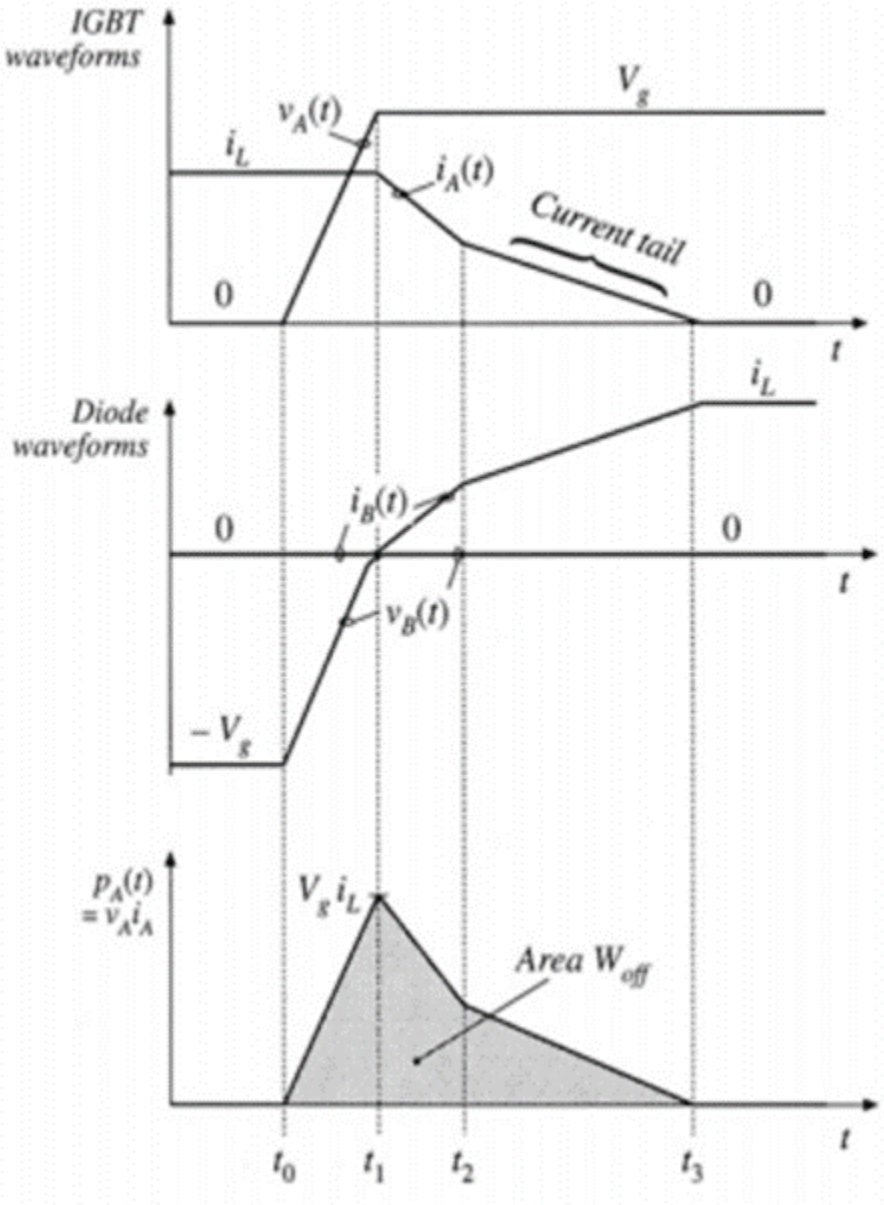

Figure 1.4. IGBT Turn-Off Transition [5]

Figure 1.5 displays a 1200V/380A motor drive inverter with IGBT power modules, which are located directly above the heat sink and below the green printed circuit boards (PCB), from Infineon Technologies; this design has an optimal switching frequency of 8 kHz [6]. The heat sink contains a direct cooled base plate to improve heat dissipation for the power module. The side view of the utilized IGBT power module is shown in Figure 1.6 [6]. This module contains two individual IGBTs in a half-bridge configuration. Connections are made available for control signals and protection circuits. When operating at a low switching frequency, passive components such as inductors and capacitors that are used for reducing current and voltage ripple will need to be large to meet the anticipated electrical requirements. Based on these technical targets and the present limitations of IGBT power devices - with an emphasis on the power density - wide bandgap (WBG) semiconductor devices can be utilized. WBG power semiconductors can provide advantages when observing material drift velocity, doping density, thermal conductivity, and electric breakdown field. The next section will feature characteristics of Silicon Carbide (SiC) and Gallium Nitride (GaN) devices and display WBG power modules.

Figure 1.5. Hybrid Kit Drive 1200V Automotive Inverter (Infineon Technologies) [6]

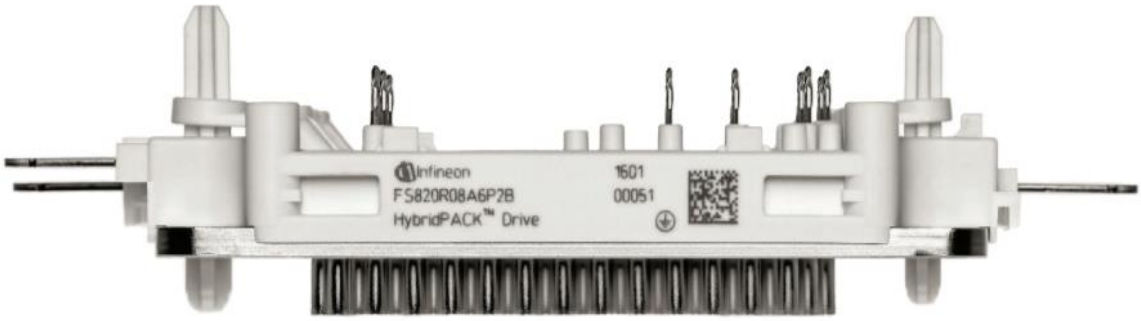

Figure 1.6. HybridPack Power Module (Infineon Technologies) [6]

Wide Bandgap Devices

As silicon (Si) power devices near technology maturation, the need for lower conduction and switching losses for power semiconductor devices as society continues electrifying the transportation industry has led to the development of SiC and GaN power modules for EV traction inverters. Specific material properties have led to this transition from Silicon based traction inverters to WBG traction inverters; these properties can be seen in Table 1.3 [7]. The main driving force of power device innovations is the desire to achieve more current for a given chip area and breakdown voltage [8].

Several physical characteristics of semiconductors can detail the operation of a power device. When observing the high electric breakdown field for SiC and GaN compared to Si, these WBG devices will have a higher breakdown voltage. A power device with a high breakdown voltage can then be used for high power applications. Likewise, a larger critical electric field can allow for a shorter drift width that reduces the on-state resistance. For a higher electron mobility, the on-state resistance can also be lowered, creating lower conduction losses for the power device; Figure 1.7 displays an on-state resistance comparison for a one square millimeter device versus blocking voltage for Si, SiC and GaN [9]. Pertaining to thermal conductivity, SiC is well suited for high operation temperatures compared to Si, meaning the size of heat sinks can be reduced or the devices can operate reliably in high temperature applications.

Table 1.3. Physical Characteristics of Semiconductors [7]

Property	Si	4H-SiC	GaN	Diamond
Bandgap (eV)	1.12	3.26	3.45	5.45
Dielectric Constant (ε_r)	11.9	10.1	9	5.5
Breakdown Field (kV/cm)	300	2200	2000	10000
Electron Mobility (cm^2/ V·s)	1500	1000	1250	2200
Hole Mobility (cm^2/ V·s)	600	115	850	850
Thermal Conductivity (W/ cm·K)	1.5	4.9	1.3	22
Saturated Electron Drift Velocity (cm/s)	$1 \cdot 10^7$	$2 \cdot 10^7$	$2.2 \cdot 10^7$	$2.7 \cdot 10^7$

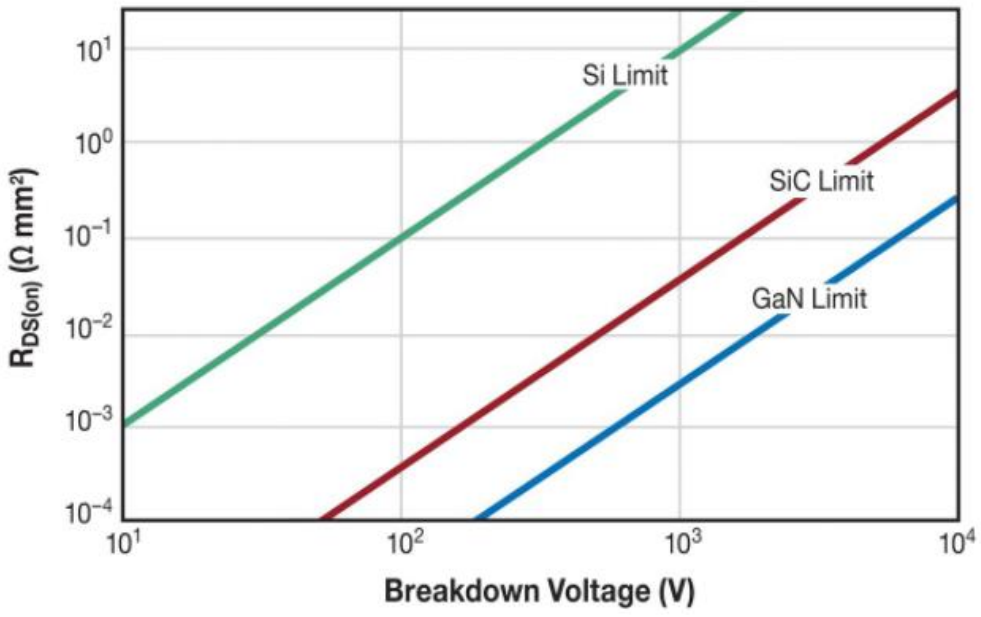

Figure 1.7. Theoretical On-Resistance of a One Square Millimeter Device [9]

Furthermore, both SiC and GaN provide opportunities to increase the switching frequency of a Si-based traction inverter. The smaller dielectric constant with a low junction capacitance creates a faster switching device. As previously mentioned, traction inverter power density targets for 2025 are greater than 100 kilowatts per liter; therefore, operating at a high switching frequency is essential. The following section will provide further details on SiC and GaN technologies.

Silicon Carbide

The application space for SiC power devices covers consumer electronics, automotive, and industrial areas [10]. However, the core focus for SiC is within the automotive and industrial applications. Automotive applications, ranging from 10 kW to 350 kW, include the onboard DC/DC charger and DC/AC motor drive inverter. Industrial applications, ranging from 100 kW to 1 MW, include industrial motor drive systems and wind turbines. For two-level traction inverter applications, the SiC MOSFET selection is dependent on the DC bus voltage. For 400 V systems, 650 V SiC MOSFETs can be employed; for 800 V systems, 1200 V SiC MOSFETS can be used. Several companies provide SiC power modules, including Cree and Infineon. Provided below are example packages for high voltage and high current applications. Figure 1.8 displays multiple 1200 V Half-Bridge power modules with a current rating of 325 A and 400 A [11]. Lower current rated power devices can be found in discrete packaging, which can be seen in Figure 1.9.

Figure 1.8. 1200V Half-Bridge Power Modules (Cree) [11]

Figure 1.9. 1200 V Discrete SiC MOSFETs (Cree) [12]

Figure 1.9 displays 1200 V discrete SiC MOSFETs with a current rating of 66 A in a TO-247-3 package, 66 A in a TO-247-4 package, and 68 A in a TO-063-7 package [12]. For the inverter design presented in this thesis, discrete SiC MOSFETs are used in a TO-247-3 package. Both TO-247-4 and TO-063-7 packages offer a kelvin source connection to lower the parasitic inductance within the gate driving loop. Lowering the parasitic inductance within the gate driving loop will reduce voltage spikes and oscillations as the gate driver turns on and off the power devices. As SiC is able to meet both high voltage and high current demands for traction inverters with a more efficient operation than the Si IGBT, there is rising adoption for SiC in the automotive market.

Gallium Nitride

The application space for GaN power devices covers consumer electronics and automotive sector [10]. For consumer electronics, GaN is competing with Si MOSFETs and is displaying tremendous strides in improving the power density of uninterruptible power supplies (UPS) and other power processing units (PPU) below 5 kW. Within the automotive industry, GaN is now competing with Si and SiC power devices. Considering 48 V motor drive inverters for mild HEVs, there are GaN power devices widely available to accommodate the several kilowatts of power needed. Efficient Power Conversion (EPC) provides a line of devices suitable for motor drive applications with an 80 V rating [13]. Additionally, GaN Systems provides 100 V products with current capabilities up to 90 A [14]. Higher voltage GaN devices are available from companies such as Infineon, GaN

Systems, Nexperia, and Transphorm. Infineon provides 600 V devices while GaN Systems, Nexperia, and Transphorm deliver 650 V devices. Figure 1.10 shows a three phase power module rated for 650 V and 300 A from GaN Systems [15]. This module includes paralleled 150 A dies to achieve a specified power rating of 75 kW. Evident by a voltage rating of 650 V, these GaN power devices are limited to 400 V battery systems for a two-level inverter for the motor drive system. Multi-level inverters make GaN devices suitable for 800 V systems; however, the design is now more complex and may reduce the power density while increasing the cost with additional semiconductor devices and control circuits. To summarize the opportunities for WBG power modules, Figure 1.11 displays the applications of SiC and GaN for a performance criteria based on switching frequency, efficiency, and power density with respect to the breakdown voltage [16]. GaN is desirable at lower voltages where there is a demand for high frequency, efficiency, and power density operations. SiC is desirable at higher voltages where there is a demand for high frequency, efficiency, and power density operations. The darker regions in Figure 1.11 show the application overlap between semiconductor materials. Having reviewed the importance and capabilities of WBG devices in motor drive inverters to improve its power density by operating at a higher switching frequency than Si-based inverters, the next section will discuss why WBG devices are beneficial for low-speed sensorless motor control strategies.

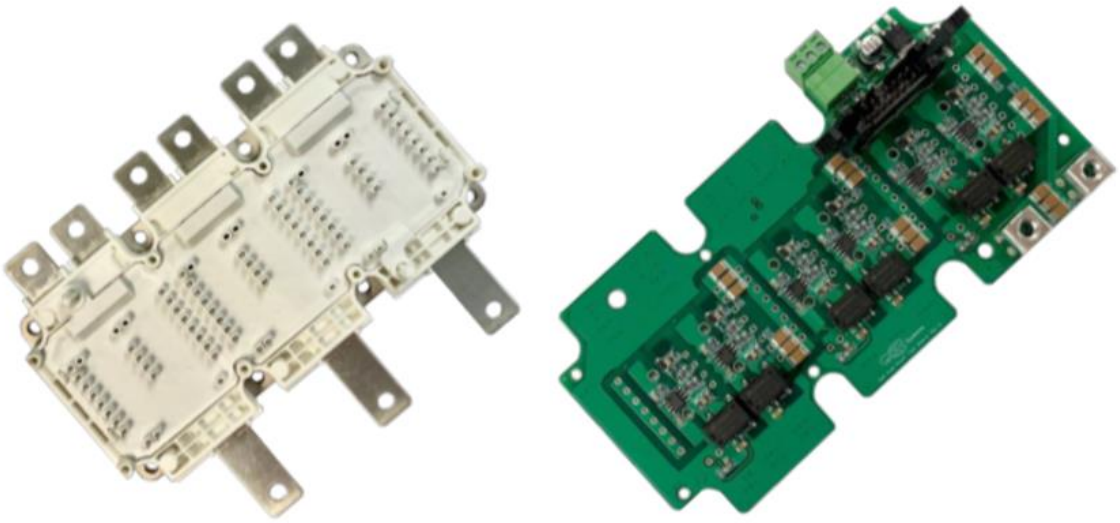

Figure 1.10. Three Phase 650 V 300 A Power Module (GaN Systems) [15]

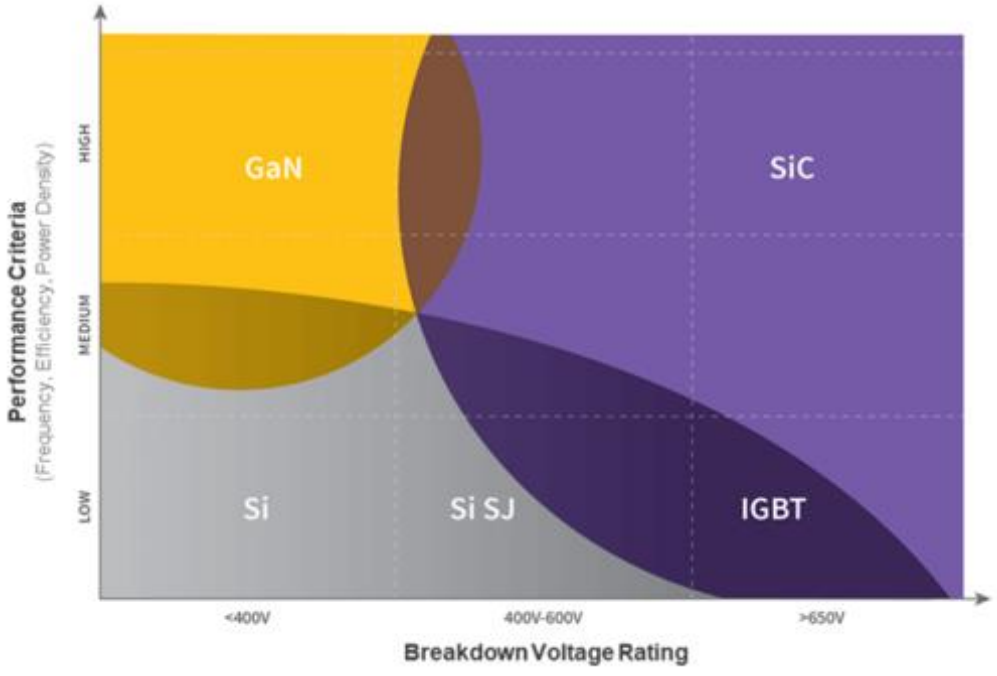

Figure 1.11. Material Performance Criteria versus Breakdown Voltage [16]

Sensorless Control

Once the EV traction inverter is developed, motor control algorithms are formulated to complete the electric drive system. The motor drive system will include a position sensor that is necessary for effective motor control. This mechanical position sensor can be comprised of an optical encoder, electromagnetic resolver, magnetic encoder, or linear hall-effect sensor [17]. Figure 1.12 displays an example layout for an electromagnetic resolver used to extract the position information of an electric motor [18]. An electromagnetic resolver will have a sinusoidal excitation signal as its input, and it will have two sinusoidal signals returning. The output signals originate from two different windings that are offset mechanically by 90 degrees. Position sensors in motor control are critical for the safe and reliable operation of an EV or HEV. Therefore, they must be properly installed and verified for signal accuracy, leading to high costs for position sensors within a motor drive system. Additional electrical circuits are also needed for further filtering and transferring the resolver outputs to the resolver-to-digital converter (RDC). Figure 1.13 shows an example circuit to convert the resolver signals to a digital value comprehensible for the microcontroller, which includes a third order low-pass filter between the resolver output and the RDC [18].

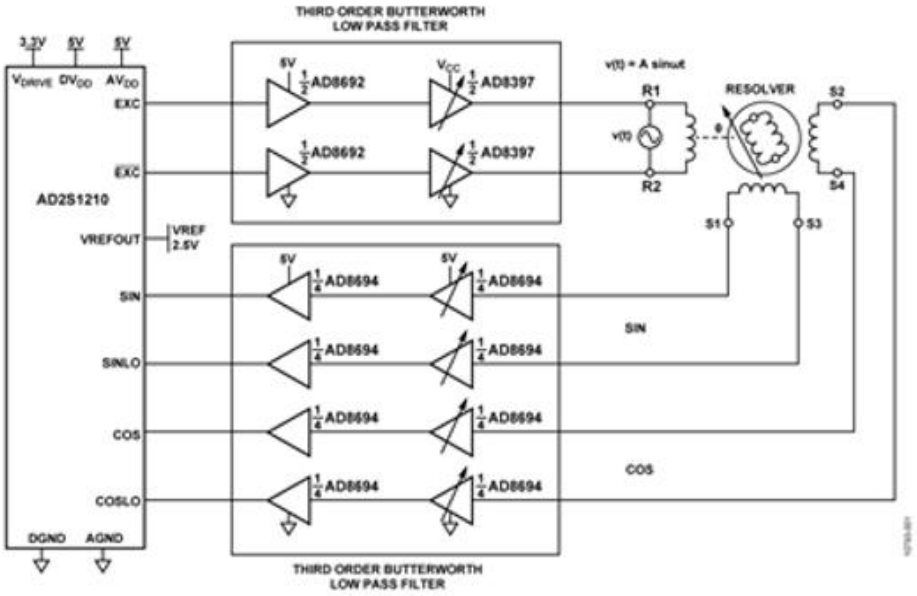

Figure 1.12. Electromagnetic Resolver Schematic [18]

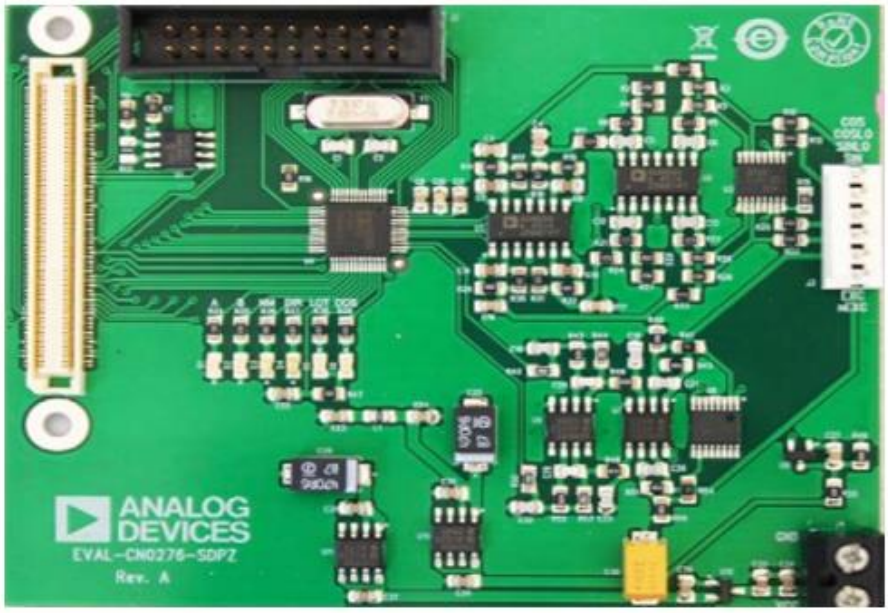

Figure 1.13. Resolver to Digital Converter (Analog Devices) [18]

For sensorless control of AC motor drives, a position estimation is made without the mechanical position sensor. For large EV drive motors, sensorless control methods do not remove the installed position sensor but add an additional measure of reliability for the motor drive system. However, for small motors performing ancillary services, sensorless position estimation can be used to remove the position sensor. By eliminating the position sensor and processing units, the cost of a motor drive system can be reduced, and the structure of the electric motor can be simplified. Therefore, the sensorless control algorithm must be accurate for position estimates at varying speed ranges while providing the desired torque command once the position sensor is eliminated. Reviewed in chapter three, there are different methods available to track the motor position for specific speed ranges. Some methods work well at high speeds, while performing poorly at low speeds. Other methods are more suitable for low speed ranges. In this thesis, the operation of a motor drive system at a low speed range is investigated using a high frequency injection method to estimate the motor position and angular velocity.

The sensorless position estimate is made possible through sampling the three phase current and then developing computationally intensive observers to provide the final position estimation. This high frequency injection method introduces a sinusoidal or square-wave voltage injection onto the motor windings. Present research shows this injected signal is typically 500 Hz but can be increased. In order to achieve such injected frequencies, the switching frequency

of the inverter should be much greater than the injected frequency. For a 2 kHz injected signal, a switching frequency of 10 kHz may be too low to provide a high resolution sinusoidal injection signal onto the motor – determining the proper injection and switching frequency will be discussed further in this thesis. Additionally, frequencies below 20 kHz significantly contribute to the audible noise within the motor drive. To reduce this acoustic noise, it is clear that a motor drive inverter should be increasing its switching frequency beyond 20 kHz. With the combination of providing a high frequency injected signal and increasing the switching frequency beyond 20 kHz, SiC or GaN power devices can be implemented in the motor drive inverter without sacrificing inverter efficiency.

FPGA Control

Implementing sensorless Field Oriented Control (FOC) to command the speed and torque of a permanent magnet synchronous machine (PMSM) requires a microcontroller (MCU) interacting with the motor drive inverter. Often, FOC is programmed in a Digital Signal Processor (DSP). A single-core DSP operates with a series instruction set to perform complex control algorithms of sensorless FOC. As the computational requirements are increased, the control bandwidth becomes constrained. If the desired switching frequency is set to 5 kHz, the DSP must complete a full control loop cycle within 5 kHz before updating the duty cycles of the inverter power modules. For high frequency sinusoidal injection sensorless control, it is necessary to impose a high resolution sinusoidal waveform onto the direct axis of the motor. Therefore, a limited control bandwidth

due to a serial instruction set and low switching frequency do not provide optimal sensorless control. Field Programmable Gate Arrays (FPGA) allow for ultra-fast inverter motor control loops to achieve high switching frequencies due to their inherent parallel processing capabilities, extending the control bandwidth beyond 200 kHz.

Thesis Summary

Future motor drive inverters will be operating at switching frequencies greater than 10 kHz, which will allow the high frequency injection sensorless control method to implement a wider range of injection frequencies. This thesis aims to explore the impact of different injection and switching frequencies on the position estimation alongside the introduced audible noise from these signals. The amplitude of the voltage injected, and the type of injection method will also be analyzed, ultimately relating each parameter of interest to the final position estimation. Furthermore, this sensorless control investigation utilizes a SiC inverter controlled by an FPGA. The FPGA processing capabilities will be demonstrated to facilitate the sensorless control algorithm. Chapter two will discuss FOC, which is the framework for motor control, while chapter three introduces a review of present sensorless control methods. After reviewing information in those two chapters, chapter four provides sensorless control simulation results and chapter five generates experimental results.

CHAPTER TWO

FIELD ORIENTED CONTROL

Permanent Magnet Synchronous Machine

The permanent magnet synchronous machine (PMSM) is widely used for variable speed applications. PMSMs offer high efficiency, high torque at low speeds, and compact size [19]. A PMSM contains a rotor and stator; the rotor houses the permanent magnets while the stator populates the phase current windings connected to the motor drive inverter. Modeling of the PMSM will be presented, and then this chapter will conclude with the execution of FOC.

PMSM Mathematical Modeling

Electrical calculations of a three-phase PMSM can be seen in the following equations [20]. V_{sabc} represents the three-phase stator voltage, which is dependent on the stator resistance, R_s, three-phase stator currents, I_{sabc}, and the stator fluxes, ψ_{sabc}. ψ_{sabc} is reliant on the machine inductance, L_{ss} , and the flux contribution from the permanent magnets, ψ_{rabc}. The rotor flux impact is determined by the amplitude of the flux generated by the permanent magnets, ψ_r, the rotor position angle, θ_m, and the number of pole pairs, p_p.

$$[V_{sabc}] = R_s[I_{sabc}] + \frac{d[\psi_{sabc}]}{dt} \tag{2.1}$$

$$[\psi_{sabc}] = [L_{ss}][I_{sabc}] + [\psi_{rabc}] \tag{2.2}$$

$$\begin{bmatrix}\psi_{ra}\\ \psi_{rb}\\ \psi_{rc}\end{bmatrix} = \psi_r \begin{bmatrix}\cos(p_p\theta_m)\\ \cos(p_p\theta_m - {}^{2\pi}/_{3})\\ \cos(p_p\theta_m + {}^{2\pi}/_{3})\end{bmatrix} \tag{2.3}$$

L_{ss} is an inductance matrix that depends on the mutual inductances between each phase, as shown in Equation (2.4).

$$[L_{ss}] = \begin{bmatrix}L_{aa} & M_{ab} & M_{ac}\\ M_{ba} & L_{bb} & M_{bc}\\ M_{ca} & M_{cb} & L_{cc}\end{bmatrix} \tag{2.4}$$

Furthermore, L_{ss} can be expressed into parameters dependent on the saliency of the machine.

$$[L_{ss}] = [L_{so}] + [L_{sv}] \tag{2.5}$$

$$[L_{so}] = \begin{bmatrix}L_{so} & M_{so} & M_{so}\\ M_{so} & L_{so} & M_{so}\\ M_{so} & M_{so} & L_{so}\end{bmatrix} \tag{2.6}$$

$$[L_{sv}] = L_{sv}\begin{bmatrix}\cos(2p_p\theta_m) & \cos(2p_p\theta_m - {}^{2\pi}/_{3}) & \cos(2p_p\theta_m + {}^{2\pi}/_{3})\\ \cos(2p_p\theta_m - {}^{2\pi}/_{3}) & \cos(2p_p\theta_m + {}^{2\pi}/_{3}) & \cos(2p_p\theta_m)\\ \cos(2p_p\theta_m + {}^{2\pi}/_{3}) & \cos(2p_p\theta_m) & \cos(2p_p\theta_m - {}^{2\pi}/_{3})\end{bmatrix} \tag{2.7}$$

Now, the three-phase stator voltage in Equation (2.1) can be rewritten as a function of the inductance matrix and rotor flux.

$$[V_{sabc}] = R_s[I_{sabc}] + \frac{d}{dt}\{[L_{ss}][I_{sabc}] + [\psi_{rabc}]\} \tag{2.8}$$

An equivalent two-phase representation can be made by utilizing Clarke and Park transformations. The Clarke transformation can be seen in Equation (2.9) and can be carried through to yield a PMSM electromagnetic model in the two-phase fixed frame [21].

Figure 2.1 shows the transition from a three-phase fixed frame to a two-phase fixed frame [22]. Figure 2.2 then demonstrates the Park transformation. $I_{s\alpha}$ is aligned with stator current I_{sa} while $I_{s\beta}$ is comprised of stator currents I_{sb} and I_{sc}. The inductance matrix, L_{ss}, must also be converted into the two-phase domain. This transformation takes place in Equation (2.11), and an equivalent inductance matrix is created in Equation (2.12). Additionally, ψ_{rabc} is translated into the two-phase frame to account for the adjusted rotor flux according to Equation (2.14). ω_v represents the angular velocity of the rotor, which is the time derivative of the angular position.

$$\begin{bmatrix} I_{s\alpha} \\ I_{s\beta} \end{bmatrix} = \frac{2}{3} \begin{bmatrix} 1 & -\frac{1}{2} & -\frac{1}{2} \\ 0 & \frac{\sqrt{3}}{2} & -\frac{\sqrt{3}}{2} \end{bmatrix} \begin{bmatrix} I_{sa} \\ I_{sb} \\ I_{sc} \end{bmatrix} \tag{2.9}$$

$$\left[V_{s\alpha\beta}\right] = R_s\left[I_{s\alpha\beta}\right] + \frac{d[\Lambda_{ss}]}{dt}\left[I_{s\alpha\beta}\right] + \frac{d\left[I_{s\alpha\beta}\right]}{dt}[\Lambda_{ss}] + \frac{d\left[\psi_{r\alpha\beta}\right]}{dt} \tag{2.10}$$

$$[\Lambda_{ss}] = \frac{2}{3} \begin{bmatrix} 1 & -\frac{1}{2} & -\frac{1}{2} \\ 0 & \frac{\sqrt{3}}{2} & -\frac{\sqrt{3}}{2} \end{bmatrix} [L_{ss}] \frac{2}{3} \begin{bmatrix} 1 & 0 \\ -\frac{1}{2} & \frac{\sqrt{3}}{2} \\ -\frac{1}{2} & -\frac{\sqrt{3}}{2} \end{bmatrix} \tag{2.11}$$

$$[\Lambda_{ss}] = \begin{bmatrix} L_\alpha & L_{\alpha\beta} \\ L_{\alpha\beta} & L_\beta \end{bmatrix} \tag{2.12}$$

$$\frac{d[\Lambda_{ss}]}{dt} = L_{sv} p_p \omega_v \begin{bmatrix} -\sin(2p_p\theta_m) & \cos(2p_p\theta_m) \\ \cos(2p_p\theta_m) & \sin(2p_p\theta_m) \end{bmatrix} \tag{2.13}$$

$$\begin{bmatrix} \psi_{r\alpha} \\ \psi_{r\beta} \end{bmatrix} = \frac{2}{3} \begin{bmatrix} 1 & -\frac{1}{2} & -\frac{1}{2} \\ 0 & \frac{\sqrt{3}}{2} & -\frac{\sqrt{3}}{2} \end{bmatrix} \psi_r \begin{bmatrix} \cos(p_p\theta_m) \\ \cos(p_p\theta_m - 2\pi/3) \\ \cos(p_p\theta_m + 2\pi/3) \end{bmatrix} \tag{2.14}$$

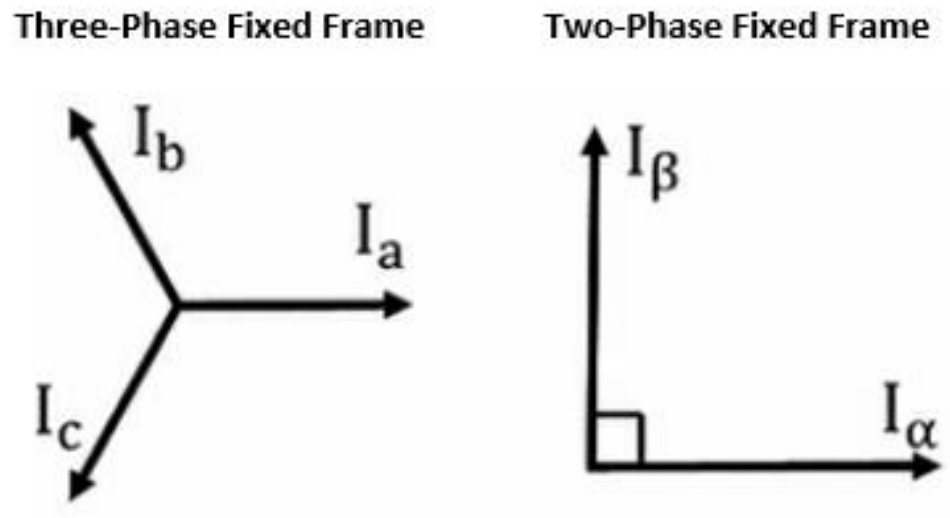

Figure 2.1. Clarke Transformation [22]

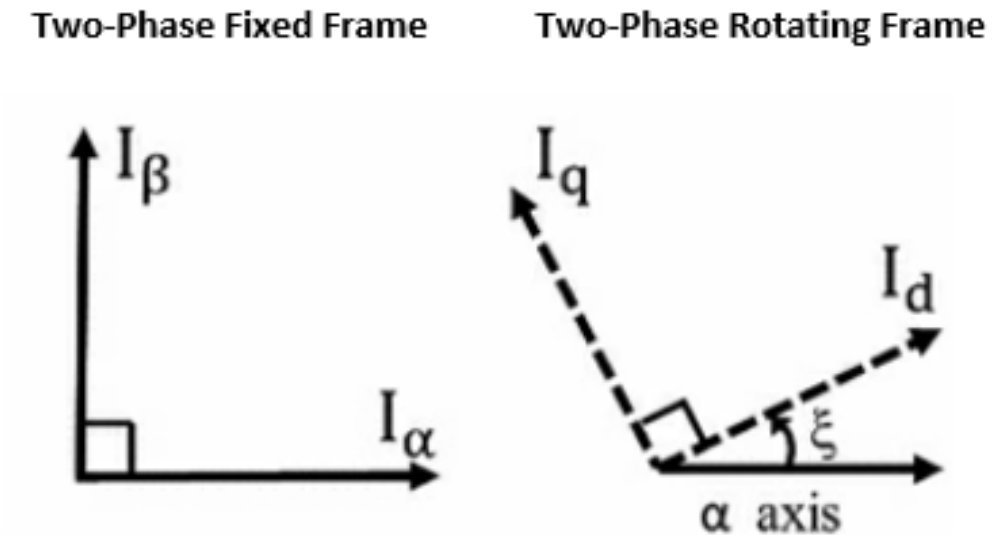

Figure 2.2. Park Transformation [22]

$$\begin{bmatrix} \frac{d\psi_{r\alpha}}{dt} \\ \frac{\psi_{r\beta}}{dt} \end{bmatrix} = \begin{bmatrix} -p_p\omega_v\psi_{r\beta} \\ p_p\omega_v\psi_{r\alpha} \end{bmatrix} \tag{2.15}$$

Furthermore, Equation (2.16) displays the final stationary frame PMSM model. This PMSM model accounts for the two-phase inductance matrix, Λ_{ss}. However, Equation (2.16) can be simplified when there are no saliency effects introduced by the rotor, evident in Equation (2.17).

$$\begin{bmatrix} \frac{d[I_{s\alpha\beta}]}{dt} \\ \frac{d\psi_{r\alpha\beta}}{dt} \end{bmatrix} = \begin{bmatrix} [\Lambda]^{-1}\left\{-\left[R_s + \frac{d[\Lambda_{ss}]}{dt}\right][I_{s\alpha\beta}] + p_p\omega_v\begin{bmatrix} 0 & 1 \\ -1 & 0 \end{bmatrix}[\psi_{r\alpha\beta}] + [V_{s\alpha\beta}]\right\} \\ -p_p\omega_v\begin{bmatrix} 0 & 1 \\ -1 & 0 \end{bmatrix}[\psi_{r\alpha\beta}] \end{bmatrix} \tag{2.16}$$

$$\begin{bmatrix} L_s\frac{d[I_{s\alpha\beta}]}{dt} \\ \frac{d\psi_{r\alpha\beta}}{dt} \end{bmatrix} = \begin{bmatrix} \left\{-R_s[I_{s\alpha\beta}] + p_p\omega_v\begin{bmatrix} 0 & 1 \\ -1 & 0 \end{bmatrix}[\psi_{r\alpha\beta}] + [V_{s\alpha\beta}]\right\} \\ -p_p\omega_v\begin{bmatrix} 0 & 1 \\ -1 & 0 \end{bmatrix}[\psi_{r\alpha\beta}] \end{bmatrix} \tag{2.17}$$

Once a model is generated in the two-phase stationary frame, a Park Transformation can made to create a two-phase rotating frame [21]. Equation (2.18) shows the transformation from a two-phase fixed frame to a two-phase rotating frame and was shown in Figure 2.2, while Equation (2.19) demonstrates the park transformation from a three-phase fixed frame to a two-phase rotating frame. The d-axis components, known as the direct axis, are intended to be aligned with the rotor flux. The q-axis components, known as the quadrature axis, will interact with the magnetic flux in the direct axis to produce torque [23]. I_{sd} is the direct axis current and I_{sq} is the quadrature current.

$$\begin{bmatrix} I_{sd} \\ I_{sq} \end{bmatrix} = \begin{bmatrix} \cos\theta_e & \sin\theta_e \\ -\sin\theta_e & \cos\theta_e \end{bmatrix} \begin{bmatrix} I_{s\alpha} \\ I_{s\beta} \end{bmatrix} \tag{2.18}$$

$$\begin{bmatrix} I_{sd} \\ I_{sq} \end{bmatrix} = \frac{2}{3} \begin{bmatrix} \cos(\theta_e) & \cos\left(\theta_e - {}^{2\pi}/_{3}\right) & \cos\left(\theta_e + {}^{2\pi}/_{3}\right) \\ -\sin(\theta_e) & -\sin\left(\theta_e - {}^{2\pi}/_{3}\right) & -\sin\left(\theta_e + {}^{2\pi}/_{3}\right) \end{bmatrix} \begin{bmatrix} I_{sa} \\ I_{sb} \\ I_{sc} \end{bmatrix} \tag{2.19}$$

θ_e represents the rotor electrical angle, which is dependent on the number of pole pairs and mechanical angle of the rotor, exhibited in Equation (2.20).

$$\theta_e = p_p \theta_m \tag{2.20}$$

Now, the complete model of a PMSM with no saliency can be described in Equation (2.21). Specifically, the electromagnetic torque can be seen in Equation (2.22).

$$\begin{bmatrix} \frac{di_{sd}}{dt} \\ \frac{di_{sq}}{dt} \\ \frac{d\omega_v}{dt} \end{bmatrix} = \begin{bmatrix} -\frac{R_s}{L_s} i_{sd} + p_p \omega_v i_{sq} + \frac{v_{sd}}{L_s} \\ -\frac{R_s}{L_s} i_{sq} + p_p \omega_v i_{sd} + \frac{v_{sq}}{L_s} - p_p \omega_v \frac{\psi_r}{L_s} \\ -\frac{f_v}{J} \omega_v + \frac{p_p \psi_r}{J} i_{sq} - \frac{1}{J} T_l \end{bmatrix} \tag{2.21}$$

$$T_e = \frac{3}{2} p_p \psi_r i_{sq} \tag{2.22}$$

Saliency

The physical attributes of the rotor lead to changes in the saliency of the PMSM. A surface mounted PMSM (SPMSM) includes magnets placed on the surface of the rotor that present a homogeneous gap [24]. This allows the PMSM inductance to be independent of the rotor position; thus, the d-axis and q-axis inductances are equivalent. For an interior PMSM (IPMSM), the magnets are integrated into the rotor's body, creating a salient-pole motor. This leads to a

slightly different inductance on the d-axis and q-axis while the rotor spins. Reluctance torque is created from this, making IPMSM's advantageous in the EV domain. Figure 2.3 displays the structure for each of these rotors. Based on this saliency affect, modeling of the PMSM will be adjusted according to an IPMSM in the next section.

IPMSM Mathematical Modeling

Inductances from Equations (2.5) to (2.7) can now be written with new parameters, L_d and L_q. For an IPMSM, L_d is not equal to L_q and the following equations will introduce a new inductance matrix.

$$L_{sv} = \frac{1}{3}[L_d - L_q] \tag{2.23}$$

$$L_{so} = \frac{1}{3}[L_d + L_q] \tag{2.24}$$

$$[\Lambda_{ss}] = \frac{1}{2}[L_d - L_q]\begin{bmatrix}\cos(2\theta_e) & \sin(2\theta_e)\\ \sin(2\theta_e) & \cos(2\theta_e)\end{bmatrix} + \frac{1}{2}[L_d + L_q]\begin{bmatrix}1 & 0\\ 0 & 1\end{bmatrix} \tag{2.25}$$

The electromagnetic model of an IPMSM in the two-phase rotating frame can now be seen in Equation (2.26). The electromagnetic torque can then be seen in Equation (2.27).

$$\begin{bmatrix}\frac{di_{sd}}{dt}\\ \frac{di_{sq}}{dt}\\ \frac{d\omega_v}{dt}\end{bmatrix} = \begin{bmatrix}-\frac{R_s}{L_d}i_{sd} - p_p\omega_v\frac{L_q}{L_d}i_{sq} + \frac{v_{sd}}{L_d}\\ -\frac{R_s}{L_q}i_{sq} - p_p\omega_v\frac{L_d}{L_q}i_{sd} + \frac{v_{sq}}{L_q} - p_p\omega_v\frac{\psi_r}{L_q}\\ -\frac{f_v}{J}\omega_v + \frac{p_p}{J}(L_d - L_q)i_{sq}i_{sd} + p_p\psi_r i_{sq} - \frac{1}{J}T_l\end{bmatrix} \tag{2.26}$$

$$T_{em} = \frac{3}{2}p_p(L_d - L_q)i_{sq}i_{sd} + \frac{3}{2}p_p\psi_r i_{sq} \tag{2.27}$$

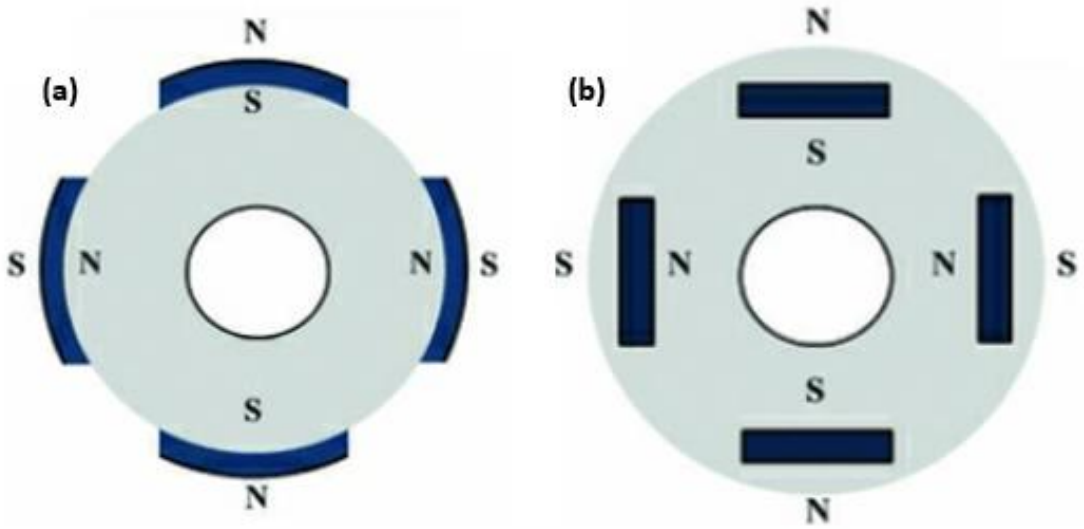

Figure 2.3. (a) Surface Mounted PMSM and (b) Interior PMSM [24]

Motor Control

By understanding the governing equations for an IPMSM, one can develop an FOC program to provide the desired speed and torque. Depending on the application, a speed reference may never be applied. Electric vehicle traction motors are normally provided a torque command based on the accelerator pedal. It is only when cruise control is specified that the motor drive system will regulate the speed of the electric motor. The speed, n, of an IPMSM is dependent on the electrical frequency, f_e, at which the stator currents operate. Equation (2.28) displays the speed calculation in revolutions per minute. p_p is the motor's pole pair number.

$$n = \frac{60 f_e}{p_p} \tag{2.28}$$

The torque can then be set by (1) measuring the three-phase stator currents, (2) comparing them to the direct axis and quadrature axis reference currents to generate an error signal, and then (3) modulating the motor terminal voltages based on the error signal in the measured and commanded currents to improve the control of the motor. A block diagram shown in Figure 2.4 shows the structure of Field Oriented Control for an IPMSM [25]. Within FOC, there is a Proportional-Integral (PI) controller for the speed and current references, Park and Clarke Transformations, Space Vector Modulation, and protection algorithms to ensure the safe operation of the electric drive system. The PI controller for the current references regulate I_{sd} and I_{sq}. This creates an inner loop within FOC and can be

labeled as the torque loop, as shown in the Figure 2.5. The three-phase current is sampled by external current sensors and then converted to the direct and quadrature axis rotating frame to regulate the torque of the motor. The difference in the measured and commanded currents generates an error signal that becomes the input of the current PI controller; there are separate PI controllers for I_{sd} and I_{sq}. In the presence of a speed controller, the output of the speed PI controller will become the input of the I_{sq} PI controller. The speed loop is considered the outer loop and regulates the desired speed of the motor, creating a fundamental frequency at which the stator phase currents operate. I_{sq} is regulated to accelerate or decelerate the motor as the speed command changes. Equation 2.28 describes the speed definition of the motor; therefore, a fundamental frequency must be set. This frequency originates from the sine and cosine position signals that are used for Park Transformations. Finally, PWM signals to the power devices must be developed to regulate the motor.

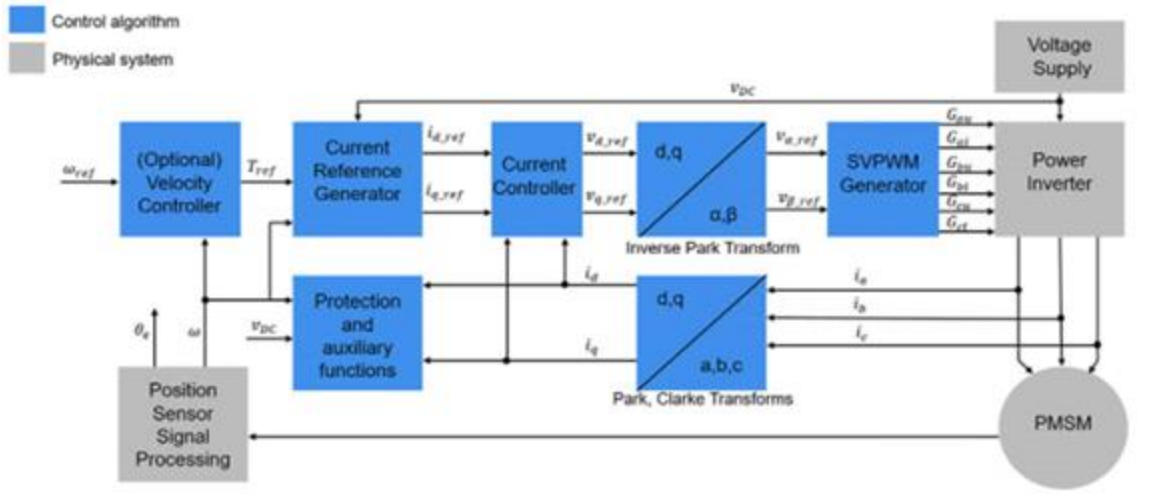

Figure 2.4. Field Oriented Control Block Diagram (Mathworks) [25]

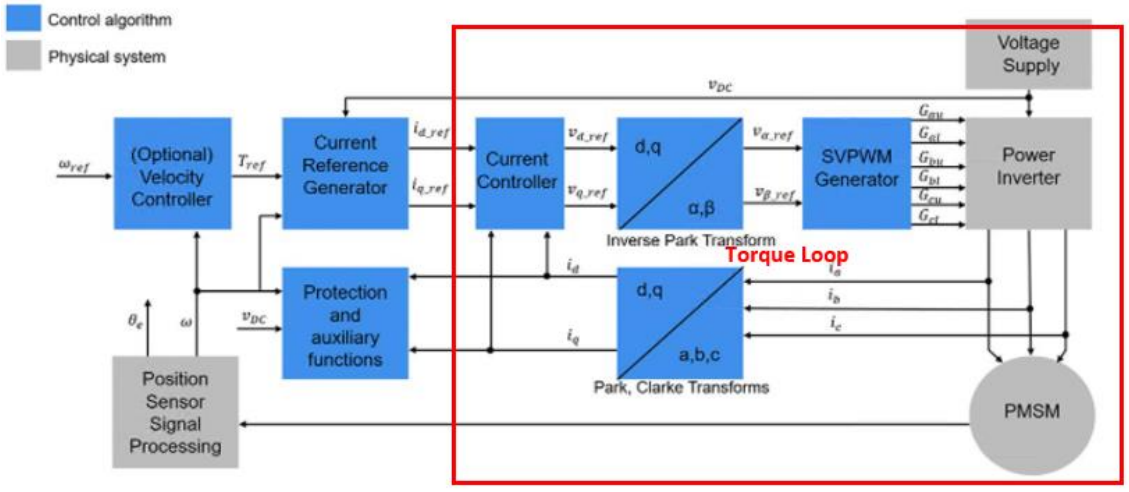

Figure 2.5. Torque Loop (Mathworks) [25]

CHAPTER THREE

LITERATURE REVIEW

Sensorless control algorithms can be categorized based on their position estimation technique. Physical models, dependent on the governing mathematical equations for electric motors and estimated machine parameters, perform well in the high-speed range but become unreliable at low speeds. The Back-Electromotive-Force (Back EMF), Kalman Filter, and Sliding Mode Observer are physical model based methods. At standstill and low speeds, the dominating position estimation technique requires signal injection. High frequency injection may introduce audible noise into the system and can suffer from dynamic bandwidths due to the filtering process. Intelligent control using artificial intelligence, genetic algorithms, or fuzzy logic may also be used to perform sensorless FOC; however, these methods require large sets of data for training the implemented algorithms for precise position estimation. Some researchers have introduced hybrid methods for sensorless control that combine both physical models and high frequency injection. Often there is a transition region between low speed high frequency injection and high-speed model based approaches. Now, a review of different sensorless control techniques will be covered.

Back-Electromotive-Force (EMF) Observer

The Back EMF method provides a position estimation through the integration of the total flux linkage within the stator phase currents [26] [27] [28] [29]. With an IPMSM, the stator circuit definition in the synchronous rotating reference frame is shown in Equation (3.1) [29].

$$\begin{bmatrix} v_d \\ v_q \end{bmatrix} = \begin{bmatrix} r_s + pL_d & -\omega_{re}L_q \\ \omega_{re}L_d & r_s + pL_q \end{bmatrix} \begin{bmatrix} i_d \\ i_q \end{bmatrix} + \begin{bmatrix} 0 \\ \omega_{re}\lambda_{pm} \end{bmatrix} \tag{3.1}$$

v_d, v_q, i_d and i_q are the $d-q$ components of the stator voltage and current vectors. ω_{re} represents the electrical rotor speed; L_d and L_q are the d-axis and q-axis inductances; p is the differential operator; r_s is the stator resistance; λ_{pm} is the rotor permanent-magnet flux. Equation (3.1) can then be transformed into the stationary reference frame, which leads to the derivation of Equation (3.2) and Equation (3.3) [30].

$$v_\alpha = r_s i_\alpha + \frac{di_\alpha}{dt} L_d + \omega_{re}\left(L_d - L_q\right) i_\beta + e_\alpha \tag{3.2}$$

$$v_\beta = r_s i_\beta + \frac{di_\beta}{dt} L_d - \omega_{re}\left(L_d - L_q\right) i_\alpha + e_\beta \tag{3.3}$$

e_α and e_β represent the back-EMF of the IPMSM in stationary reference frame and can be described by Equation (3.4) and Equation (3.5) [31].

$$\begin{bmatrix} e_\alpha \\ e_\beta \end{bmatrix} = e \begin{bmatrix} -\sin\theta_{re} \\ \cos\theta_{re} \end{bmatrix} \tag{3.4}$$

$$e = \omega_{re}\lambda_{pm} + \left(L_d - L_q\right)\left(\omega_{re} i_d - p i_q\right) \tag{3.5}$$

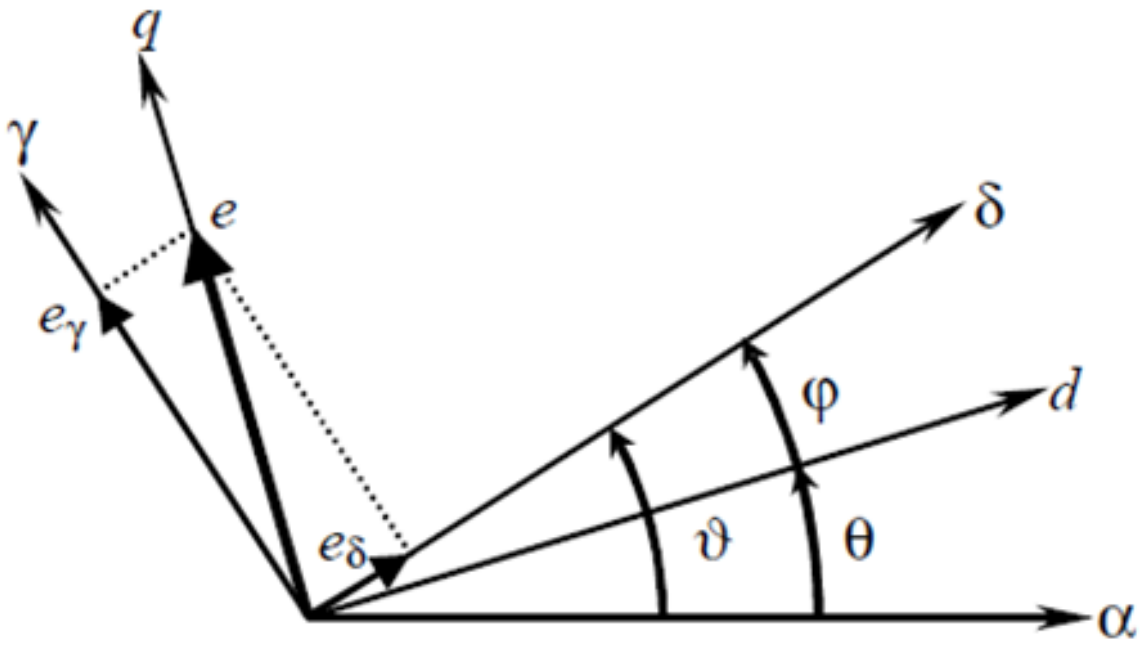

Figure 3.1. $\delta - \gamma$ and $d - q$ reference frames

A state filter based on current observers in the stationary reference frame can be used to estimate e [31]. Ideally, the estimated back-EMF is equal to the actual back-EMF of the IPMSM [29].

$$\lim_{t\to\infty}\begin{bmatrix}\hat{e}_\alpha(t)\\ \hat{e}_\beta(t)\end{bmatrix} = e\begin{bmatrix}-\sin\theta_{re}(t)\\ \cos\theta_{re}(t)\end{bmatrix} \tag{3.6}$$

The rotor position, θ_{re}, can be obtained using the estimated back-EMF shown in Equation (3.6). Figure 3.2 shows the diagram to estimate the rotor flux angle and speed. To simplify the implementation, the sign of the estimated rotor speed is multiplied with the estimated back-EMF. A new back-EMF estimation can be seen in Equation (3.7) [29].

$$\begin{bmatrix}\hat{e}_\alpha^{\#}\\ \hat{e}_\beta^{\#}\end{bmatrix} = sign(\hat{\omega}_{re})\begin{bmatrix}\hat{e}_\alpha\\ \hat{e}_\beta\end{bmatrix} = |\hat{e}|\begin{bmatrix}-\sin\theta_{re}\\ \cos\theta_{re}\end{bmatrix} \tag{3.7}$$

The angle estimation error, ϵ, can be obtained by using Equation (3.8) or Equation (3.9) [31].

$$\epsilon = -\hat{e}_\alpha^{\#}\cos\left(\hat{\theta}_{re}\right) - \hat{e}_\beta^{\#}\sin\left(\hat{\theta}_{re}\right) \tag{3.8}$$

$$\epsilon = |\hat{e}|\sin\left(\theta_{re} - \hat{\theta}_{re}\right) \tag{3.9}$$

Next, a PID controller is used to estimate the electrical speed with the angle estimation error as the input. The final estimated angle is then calculated through the integration of the electrical speed. Based on the rotor angle and speed estimation equations, this approach may suffer from the measurement error or noise in the voltages and currents; moreover, the motor resistance and inductance can vary depending on the external environment [27] [32].

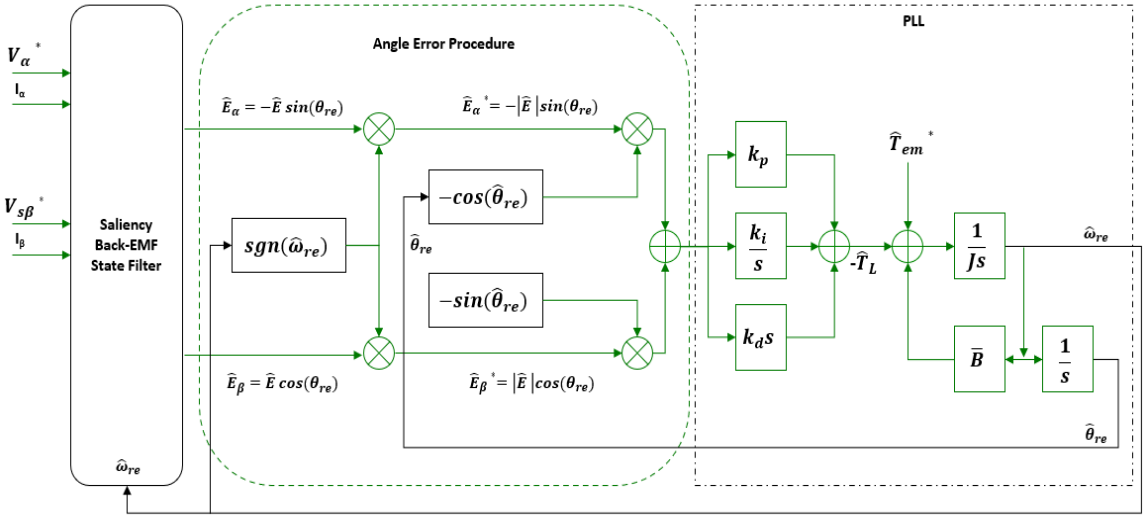

Figure 3.2. Saliency Back-EMF Rotor Flux Angle and Speed Estimator [29]

Table 2.1 shows the influence specific parameters have on the estimated position error. Based on the analysis, the estimated rotor position error increases with the error of the stator resistance, stator inductance, and stator current, and the angle error decreases from an increase in the stator voltage [33]. The PWM signal delay caused from the microcontrollers and the inductance variation significantly impact the estimated position error compared to other parameter variations. To solve the parameter variation issues, an online parameter identification method can be applied for the sensorless control algorithm to improve the estimated position error. An online parameter identification method with the back-EMF observer can be seen in Figure 3.3 [34].

Sliding Mode Observer

The sliding mode observer offers a simple approach to estimate the angular position of the rotor. It provides a more robust method in the presence of parameter variations and has features for a fast dynamic response [35] [36]. However, this method suffers from a chattering problem, which can be solved with the implementation of low-pass filters [36] [37] [38]. The conventional sliding mode observer block diagram is shown in Figure 3.4. The sliding hyperplane, S, can be defined based on the stator current error, displayed in Equation (3.10) [38].

Table 3.1. Parameter Variations and Measurement Error [33]

Parameter	Cause	Position Error Influence
Resistance	Thermal Effect	Negligible
Inductance	Flux Saturation	DC Offset at Steady-State
Current	Sensor Uncertainty	DC, 1st,2nd Order Harmonics Injected
Voltage	Dead-Time Effect	Harmonics Injected
PWM Signal	Delay from DSP	DC Offset

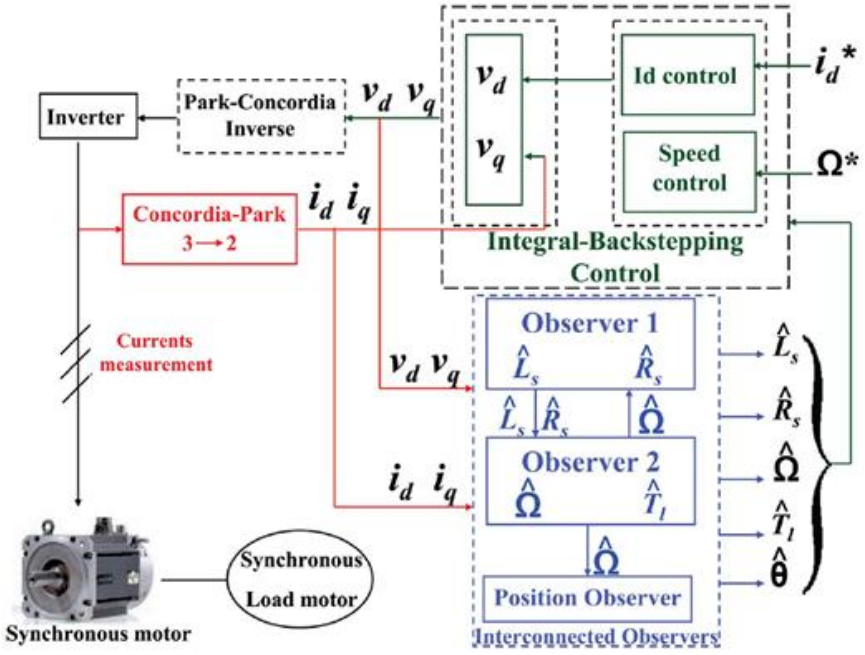

Figure 3.3. Online Parameter Identification with Back-EMF Observer [34]

$$S(x) = \begin{bmatrix} \tilde{\imath}_\alpha \\ \tilde{\imath}_\beta \end{bmatrix} = \begin{bmatrix} \hat{\imath}_\alpha - i_\alpha \\ \hat{\imath}_\beta - i_\beta \end{bmatrix} \tag{3.10}$$

The sliding mode observer can then be constructed with Equation (3.11) [35]. $\hat{e}_\alpha$, $\hat{e}_\beta$ are the estimated back EMF; z_α, z_β are the switching signals related to the stator current errors, which contain the information of the estimated back EMF. Equation (3.12) displays the switching signals definition.

$$\frac{d}{dt}\begin{bmatrix} \hat{\imath}_\alpha \\ \hat{\imath}_\beta \end{bmatrix} = \frac{1}{L_d}\begin{bmatrix} -r_s & -\hat{\omega}_{re}\left(L_d - L_q\right) \\ \hat{\omega}_{re}\left(L_d - L_q\right) & -r_s \end{bmatrix}\begin{bmatrix} \hat{\imath}_\alpha \\ \hat{\imath}_\beta \end{bmatrix} + \frac{1}{L_d}\begin{bmatrix} v_\alpha - \hat{e}_\alpha - z_\alpha \\ v_\beta - \hat{e}_\beta - z_\beta \end{bmatrix} \tag{3.11}$$

$$\begin{bmatrix} z_\alpha \\ z_\beta \end{bmatrix} = k\begin{bmatrix} sgn(\hat{\imath}_\alpha - i_\alpha) \\ sgn\left(\hat{\imath}_\beta - i_\beta\right) \end{bmatrix} \tag{3.12}$$

The gain of the sliding mode observer is a constant value that can be defined by Equation (3.13) in order to maintain the stability of the sliding mode observer control system.

$$k > \frac{1}{2} max\left(|\hat{e}_\alpha|, \left|\hat{e}_\beta\right|\right) \tag{3.13}$$

The back-EMF can be estimated with a low-pass filter for the switching signals, as shown in Equation (3.14); ω_c is the cut-off frequency of the low-pass filter.

$$\begin{bmatrix} \hat{e}_\alpha \\ \hat{e}_\beta \end{bmatrix} = \frac{\omega_c}{s + \omega_c}\begin{bmatrix} z_\alpha \\ z_\beta \end{bmatrix} \tag{3.14}$$

Finally, the estimated rotor position can be obtained from Equation (3.15).

$$\hat{\theta} = -\tan^{-1}\left(\frac{\hat{e}_\alpha}{\hat{e}_\beta}\right) \tag{3.15}$$

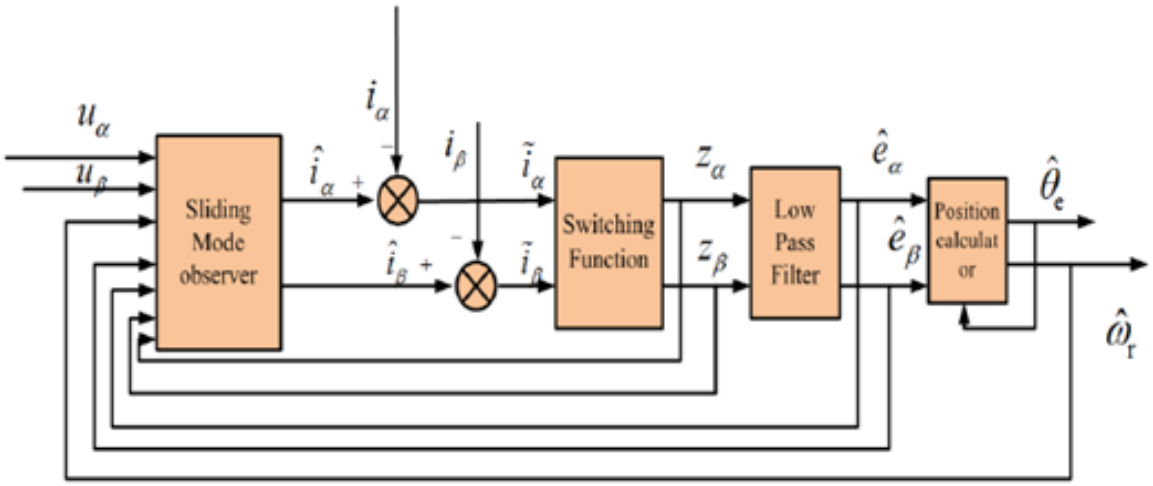

Figure 3.4. Sliding Mode Observer Block Diagram [35]

Extended Kalman Filter

The Extended Kalman Filter (EKF) is a nonlinear version of the Kalman Filter used for the estimation of state parameters in the presence of unknown disturbances in noisy environments [39] [40] [41] [42] [43]. This method is stable, effective, and widely used in many engineering fields [44]. However, this method requires online matrix computations and can be challenging to implement. The EKF process equations include a prediction and measurement calculation. The prediction process can be described by Equation (3.16) where T_s is the sampling time; x_k is the state variables matrix; u_k contains the actuating variables; A is the system matrix and B is the input matrix. Additionally, $\boldsymbol{x}_{k/k-1}$ is the a priori estimate.

$$\boldsymbol{x}_{k/k-1} = \boldsymbol{x}_{k-1} + T_s\boldsymbol{A}\boldsymbol{x}_{k-1} + T_s\boldsymbol{B}\boldsymbol{u}_{k-1} \tag{3.16}$$

A transition function can be created to simplify the prediction process. Equation (3.17) now provides the a priori estimate with the transition function, $\boldsymbol{f}(\boldsymbol{x}_{k-1}, \boldsymbol{u}_{k-1})$.

$$\boldsymbol{x}_{k/k-1} = \boldsymbol{x}_{k-1} + T_s\boldsymbol{f}(\boldsymbol{x}_{k-1}, \boldsymbol{u}_{k-1}) \tag{3.17}$$

The Jacobian matrix can be obtained through the partial derivative of the a priori estimate, shown in Equation (3.18), and the error covariance matrix is obtained in Equation (3.19).

$$\boldsymbol{J}_k = \frac{\partial\left(\boldsymbol{x}_{k-1} + T_s\boldsymbol{f}(\boldsymbol{x}_{k-1}, \boldsymbol{u}_{k-1})\right)}{\partial\boldsymbol{x}_{k-1}} \tag{3.18}$$

$$\boldsymbol{P}_{k/k-1} = \boldsymbol{J}\boldsymbol{P}_{k-1}\boldsymbol{J}^T + \boldsymbol{Q} \tag{3.19}$$

The measurement Jacobian matrix is also needed and displayed in Equation (3.20), where h is the measurement matrix.

$$\boldsymbol{H}_k = \frac{\partial h(\boldsymbol{x})}{\partial \boldsymbol{x}} \tag{3.20}$$

Next, the Kalman gain ($\boldsymbol{K}_k$), covariance update process ($\boldsymbol{P}_k$), and correction process ($\boldsymbol{x}_k$) for the state variables are described in the following equations.

$$\boldsymbol{K}_k = \boldsymbol{P}_{k/k-1}\boldsymbol{H}_k^T\left(\boldsymbol{H}_k\boldsymbol{P}_{k/k-1}\boldsymbol{H}_k^T + \boldsymbol{R}\right)^{-1} \tag{3.21}$$

$$\boldsymbol{P}_k = \boldsymbol{P}_{k/k-1} - \boldsymbol{K}_k\boldsymbol{H}_k\boldsymbol{P}_{k/k-1} \tag{3.22}$$

$$\boldsymbol{x}_k = \boldsymbol{x}_{k/k-1} + \boldsymbol{K}_k\left(\boldsymbol{y}_k - \boldsymbol{H}_k\boldsymbol{x}_{k/k-1}\right) \tag{3.23}$$

For sensorless control in the rotating reference frame of a PMSM model, the state matrix, input matrix, and output matrix can be selected with Equation (3.24).

$$\begin{aligned} \boldsymbol{x}_k &= [i_d \quad i_q \quad \omega \quad \theta]^T \\ \boldsymbol{u}_k &= [u_d \quad u_q]^T \\ \boldsymbol{y}_k &= [i_d \quad i_q]^T \end{aligned} \tag{3.24}$$

Thus, the transition function and Jacobian matrix can now be obtained.

$$\boldsymbol{f}(\boldsymbol{x},\boldsymbol{u}) = \begin{bmatrix} -\frac{r_s}{L_d}i_d + \omega\frac{L_q}{L_d}i_q + \frac{1}{L_d}v_d \\ -\frac{r_s}{L_q}i_q - \omega\frac{L_d}{L_q}i_d + \frac{1}{L_q}v_q - \omega\frac{\lambda_{PM}}{L_q} \\ 0 \\ \omega \end{bmatrix} \tag{3.25}$$

$$\boldsymbol{J} = \begin{bmatrix} 1 - T_s\frac{r_s}{L_d} & T_s\frac{L_q}{L_d}\omega & T_s\frac{L_q}{L_d}i_q & 0 \\ T_s\frac{L_d}{L_q}\omega & 1 - T_s\frac{r_s}{L_q} & -T_s\left(\frac{L_d}{L_q}i_d + \frac{\lambda_{PM}}{L_q}\right) & 0 \\ 0 & 0 & 1 & 0 \\ 0 & 0 & T_s & 1 \end{bmatrix} \tag{3.26}$$

$$\boldsymbol{H} = \begin{bmatrix} 1 & 0 & 0 & 0 \\ 0 & 1 & 0 & 0 \end{bmatrix} \tag{3.27}$$

Once the matrices have been defined, the Kalman gain, covariance process, and correction process can then be used to provide a position estimation. Figure 3.5 displays the block diagram for an EKF based sensorless control [45].

High Frequency Injection

Although physical models are straightforward to implement, they have limitations at low speeds as the back-EMF decreases, since the magnitude of the back-EMF is proportional to the rotor speed. Inaccuracies in the sampled variables and imprecise knowledge of machine parameters will yield large position estimation errors as the sensor noise and parameter inaccuracies begin to dictate calculations. High frequency injection (HFI) methods inject voltage signals, measure the induced current, and then generate a rotor position estimation. The main HFI based methods are composed of a rotating signal injection method, pulsating signal injection method, and a square wave injection method [46].

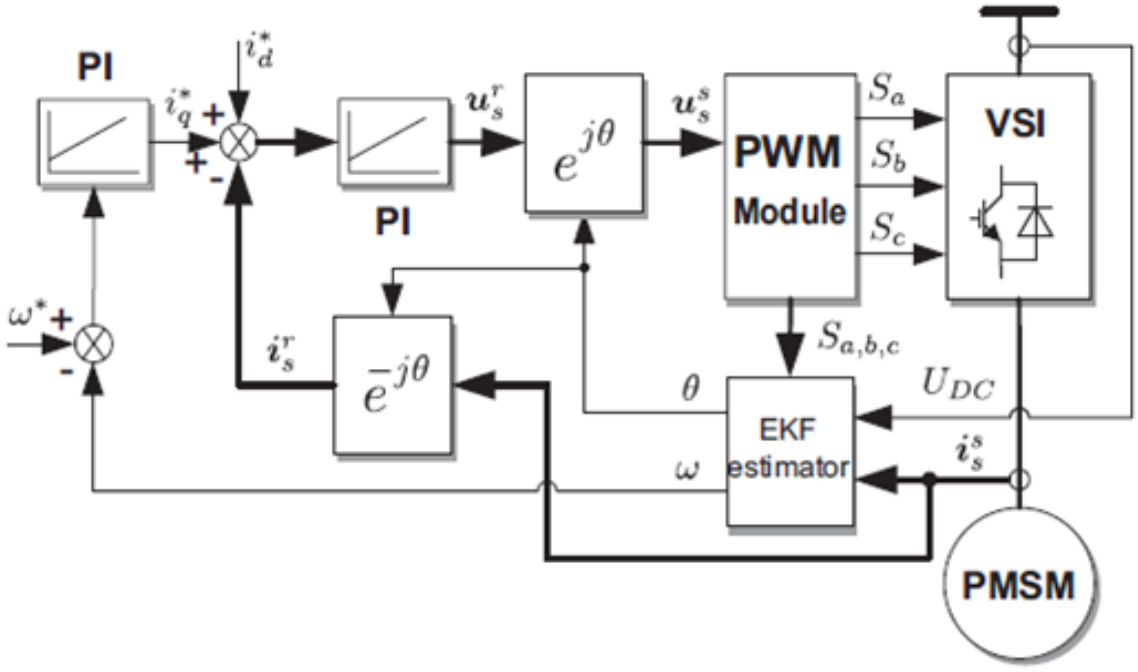

Figure 3.5. EKF Sensorless Control Block Diagram [45]

Rotating Sinusoidal Injection

In this method, a rotating signal is injected onto the $\alpha - \beta$ reference frame. This voltage signal contains an amplitude, V_{inj}, and an angular frequency in radians per second, ω_{inj} [47] [48] [49].

$$\begin{bmatrix} u_{\alpha h} \\ u_{\beta h} \end{bmatrix} = V_{inj} \begin{bmatrix} -\sin \omega_{inj} t \\ \cos \omega_{inj} t \end{bmatrix} \tag{3.28}$$

The current response in the $\alpha - \beta$ reference frame can be expressed in Equation (3.29) by applying a band-pass filter centered at the HFI frequency [50] [51] [52]. θ_{re} represents the actual rotor position embedded in the HFI currents.

$$\begin{bmatrix} i_{\alpha h} \\ i_{\beta h} \end{bmatrix} = I_{inj,0} \begin{bmatrix} \cos \omega_{inj} t \\ \sin \omega_{inj} t \end{bmatrix} + I_{inj,1} \begin{bmatrix} \cos 2\theta_{re} - \omega_{inj} t \\ \sin 2\theta_{re} - \omega_{inj} t \end{bmatrix} \tag{3.29}$$

$I_{inj,0}$ and $I_{inj,1}$ can be formulated by Equation (3.30). The rotor position information can then be extracted from $I_{inj,1}$.

$$\begin{aligned} I_{inj,0} &= \frac{V_{inj}(L_d + L_q)}{2\omega_{inj} L_d L_q} \\ I_{inj,1} &= \frac{V_{inj}(L_q - L_d)}{2\omega_{inj} L_d L_q} \end{aligned} \tag{3.30}$$

Figure 3.6 demonstrates the rotating signal injection sensorless control block diagram, and Figure 3.7 shows the general way to extract the position information from the sampled current. To acquire the angle information contained within the negative sequence current, $I_{inj,1}$, a Park transformation is made with a rotating frequency equal to the injected frequency, resulting in Equation (3.31). A

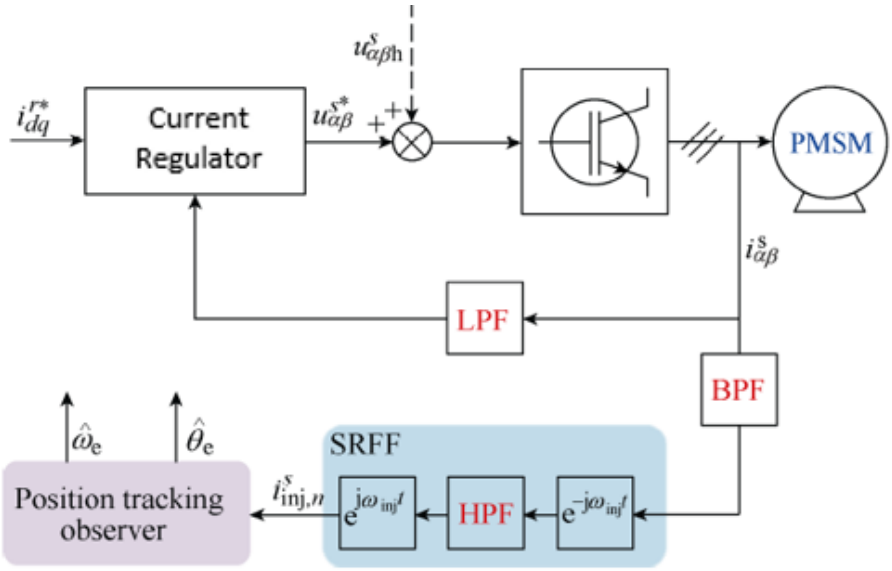

Figure 3.6. Rotating Signal Injection Block Diagram [53]

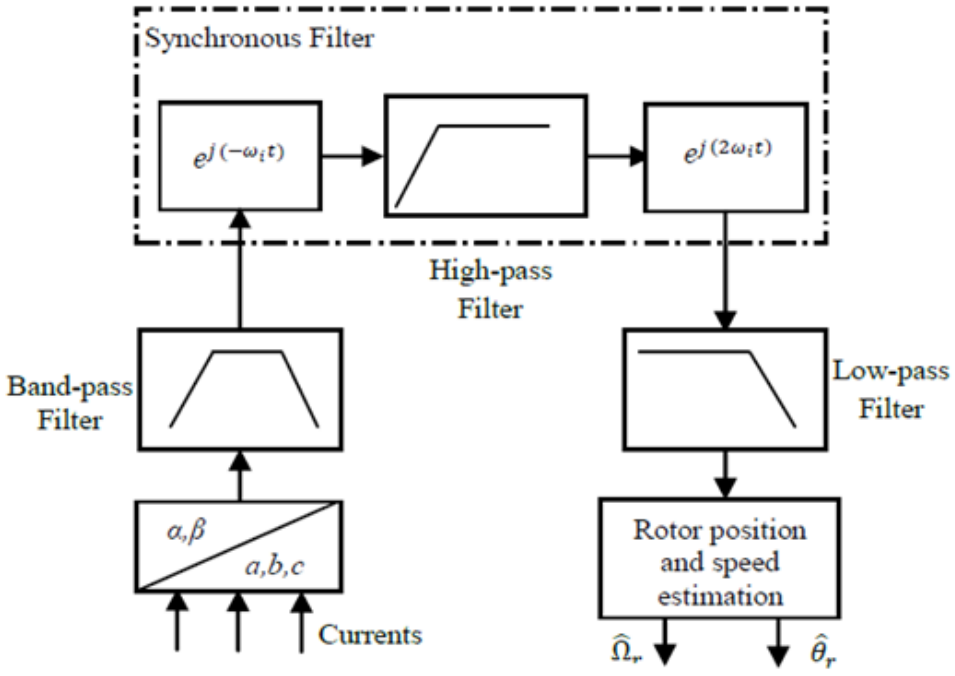

Figure 3.7. Synchronous Filters for Demodulation of HF Currents [54]

high pass filter then removes the $I_{inj,0}$ component. Transitioning back to the fundamental reference frame results in Equation (3.32).

$$\begin{bmatrix} i_{dh} \\ i_{qh} \end{bmatrix} = I_{inj,0} + I_{inj,1} \begin{bmatrix} \cos 2\theta_{re} - 2\omega_{inj}t \\ \sin 2\theta_{re} - 2\omega_{inj}t \end{bmatrix} \tag{3.31}$$

$$\begin{bmatrix} i_{\alpha h} \\ i_{\beta h} \end{bmatrix} = I_{inj,1} \begin{bmatrix} \cos 2\theta_{re} \\ \sin 2\theta_{re} \end{bmatrix} \tag{3.32}$$

The final electrical angle estimation can then be calculated through the arctangent function, shown in Equation (3.33). $\hat{\theta}_{re}$ provides the final position estimation.

$$2\hat{\theta}_{re} = tan^{-1}\left(\frac{I_{inj,1}\cos 2\theta_{re}}{I_{inj,1}\sin 2\theta_{re}}\right) \tag{3.33}$$

Pulsating Sinusoidal Injection

In this method, a pulsating signal is injected to the direct-axis of the $d-q$ reference frame [54] [32] [55] [56].

$$\begin{bmatrix} \hat{u}_{dh} \\ \hat{u}_{qh} \end{bmatrix} = V_{inj} \begin{bmatrix} \cos \omega_{inj}t \\ 0 \end{bmatrix} \tag{3.34}$$

The position error can be defined as the difference between the measured rotor position, θ_{re}, and the estimated rotor position, $\hat{\theta}_{re}$.

$$\theta_{err} = \theta_{re} - \hat{\theta}_{re} \tag{3.35}$$

To acquire this final position estimation and error, the current response from the injected signal is investigated in a similar manner as the rotating sinusoidal injection method.

A band-pass filter centered at the injection frequency is applied to the three-phase current and then converted to the $d-q$ reference frame. The saliency of the IPMSM can be reflected by extracting $\hat{\imath}_{qh}$ and passing this term through a low-pass filter, which generates the input of the speed observer. Equation (3.36) provides the current response in the $d-q$ reference frame and is multiplied by $\sin \omega_{inj} t$ to obtain I_{sal}.

$$\begin{bmatrix} \hat{\imath}_{dh} \\ \hat{\imath}_{qh} \end{bmatrix} = \begin{bmatrix} I_{inj,0} + I_{inj,1} \cos 2\theta_{err} \\ I_{inj,1} \sin 2\theta_{err} \end{bmatrix} \sin \omega_{inj} t \tag{3.36}$$

$$I_{sal} = LPF\{\hat{\imath}_{qh} \sin \omega_{inj} t\} \tag{3.37}$$

Before the LPF is applied, $\hat{\imath}_{dh}$, and $\hat{\imath}_{qh}$ can be described by Equation 3.38 and Equation 3.40 [56].

$$\hat{\imath}_{dh} = \frac{V_{inj}}{2\omega_{inj}} \left[\left(\frac{1}{L_d} + \frac{1}{L_q} \right) + \left(\frac{1}{L_d} - \frac{1}{L_q} \right) \cos 2\theta_{err} \right] \sin \omega_{inj} t + \hat{\imath}_{dh_2} \tag{3.38}$$

$$\hat{\imath}_{dh_2} = \frac{V_{inj}^2}{2\omega_{inj}^2} \frac{d^2 i_d}{d\lambda_{pm}^2} \lambda_{pm} \cos^3 \theta_{err} \sin^2 \omega_{inj} t \tag{3.39}$$

$$\hat{\imath}_{qh} = \frac{V_{inj}}{2\omega_{inj}} \left[\left(\frac{1}{L_d} - \frac{1}{L_q} \right) \sin 2\theta_{err} \right] \sin \omega_{inj} t + \hat{\imath}_{qh_2} \tag{3.40}$$

$$\hat{\imath}_{qh_2} = \frac{V_{inj}^2}{2\omega_{inj}^2} \frac{d^2 i_d}{d\lambda_{pm}^2} \lambda_{pm} \cos^2 \theta_{err} \sin \theta_{err} \sin^2 \omega_{inj} t \tag{3.41}$$

The saliency term can then be defined with Equation 3.42, showing its relationship with V_{inj}, ω_{inj}, and the saliency of the motor.

$$I_{sal} = \frac{V_{inj}(L_q - L_d)}{2\omega_{inj} L_q L_d} \sin 2\theta_{err} \tag{3.42}$$

I_{sal} is used for the final position detection as it is the input of the speed observer; it performs as an error term that passes through a PI controller and is then fed back to form a closed loop. Figure 3.8 displays the block diagram of a pulsating signal injection method. Figure 3.9 displays the closed loop system for the saliency term [56]. The estimated position is compared to the previous calculated position to create an error signal that is sent through the low-pass filter and PI controller.

Square Wave Injection

Square wave injection provides an alternative to the pulsating and rotating sinusoidal injection methods. This approach is used when the sinusoidal method suffers from a limiting bandwidth as the switching frequency of the inverter is constrained [55]. For sinusoidal injection, an injection signal at 1 kHz is problematic if the switching frequency is limited to 5 kHz. However, with square wave injection, either pulsating or rotating, can overcome this issue as the injected signal only changes from positive V_{inj} and negative V_{inj}.

$$\begin{bmatrix} \hat{u}_{dh} \\ \hat{u}_{qh} \end{bmatrix} = \begin{bmatrix} \pm V_{inj} \\ 0 \end{bmatrix} \tag{3.43}$$

The current response containing the position information can be described by Equation 3.44 and Equation 3.45.

$$\frac{d}{dt}\begin{bmatrix} i_{\alpha h} \\ i_{\beta h} \end{bmatrix} = \frac{\hat{u}_{dh}}{\omega_{inj} L_d L_q}\begin{bmatrix} \Sigma L \cos\hat{\theta}_{re} - \Delta L \cos(\theta_{re} + \theta_{err}) \\ \Sigma L \sin\hat{\theta}_{re} - \Delta L \sin(\theta_{re} + \theta_{err}) \end{bmatrix} \tag{3.44}$$

$$\begin{bmatrix} i_{\alpha h} \\ i_{\beta h} \end{bmatrix} = \frac{\hat{u}_{dh}(\Sigma L - \Delta L)}{\omega_{inj} L_d L_q}\begin{bmatrix} \cos\hat{\theta}_{re} \\ \sin\hat{\theta}_{re} \end{bmatrix} \tag{3.45}$$

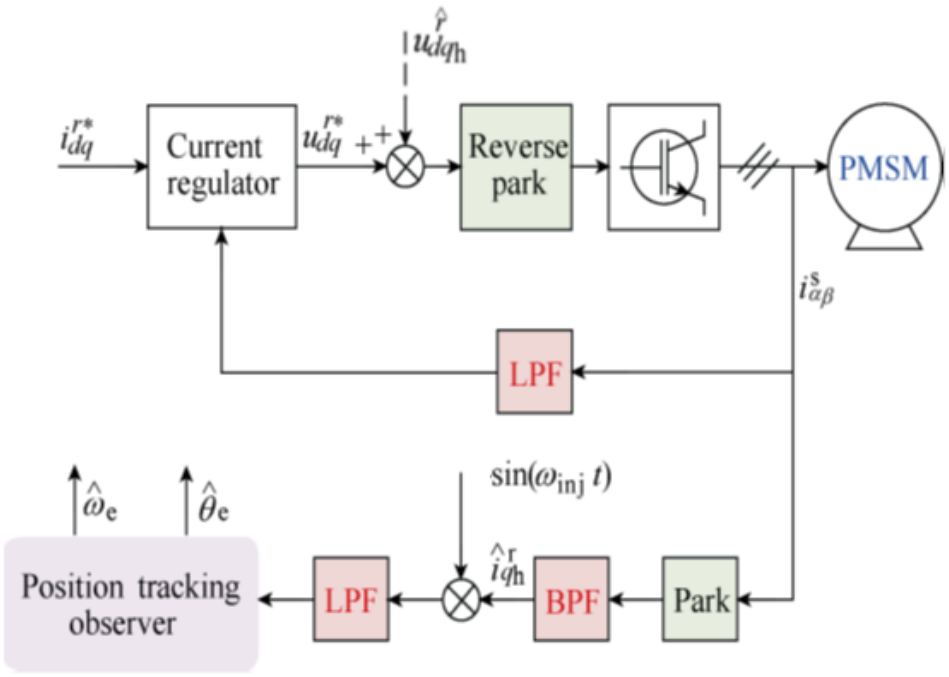

Figure 3.8. Pulsating Signal Injection Block Diagram [53]

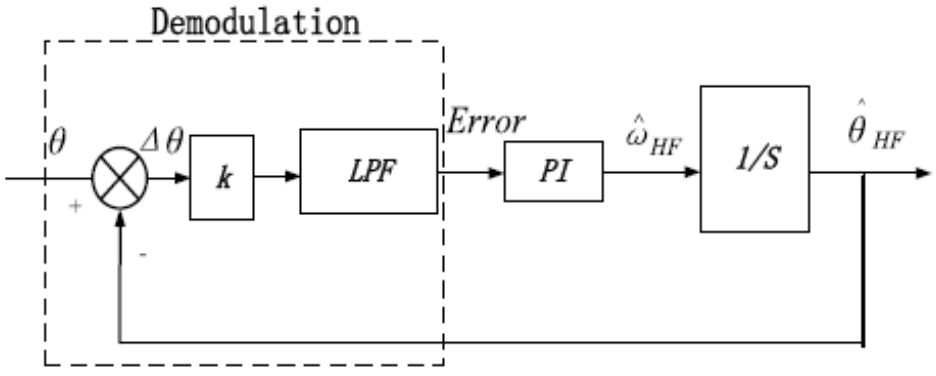

Figure 3.9. Position Tracking Loop [56]

$$\Sigma L = \frac{1}{2}\left(L_d + L_q\right) \tag{3.46}$$

$$\Delta L = \frac{1}{2}\left(L_d - L_q\right) \tag{3.47}$$

In this thesis, simulation and experimental results are derived from the rotating signal injection method for sinusoidal and square wave injection. As stated earlier, square wave injection is an alternative to sinusoidal injection when the bandwidth is too narrow. A block diagram for the square wave injection method is shown in Figure 3.10. Figure 3.11 shows the bandwidth constraints of sinusoidal injection and the improvement made by square-wave injection [55]. The PWM carrier waveform generates the switching frequency and updates the duty cycle for the inverter power devices. When the injected sinusoidal waveform is too close to the switching frequency, only a few points are used to control the duty cycle. Figure 3.11 shows just five different points from the sinusoidal signal that are implemented in one period; this discrete-time waveform is no longer a clean sinusoidal signal. The discrete-time waveform can be seen in the blue, dashed-line waveforms. For five discrete values, this implies the updating frequency of the duty cycle is only five times that of the injected sinusoidal signal – 500 Hz injection with 2.5 kHz switching frequency. Square wave injection shows that the injected voltage signal is still able to be implemented when the bandwidth is limited. Furthermore, this implies that the sinusoidal injection signal is limited by the upper bandwidth of the sensorless speed controller [57]. However, implementing these control methods in an FPGA can prevent bandwidth constraints. Therefore, within this thesis, an FPGA is utilized to develop a

relationship between the rotor fundamental frequency, inverter switching frequency, injection frequency, and the selected frequencies for the low-pass and bandpass filters. Simulation and experimental results are provided in the next chapters.

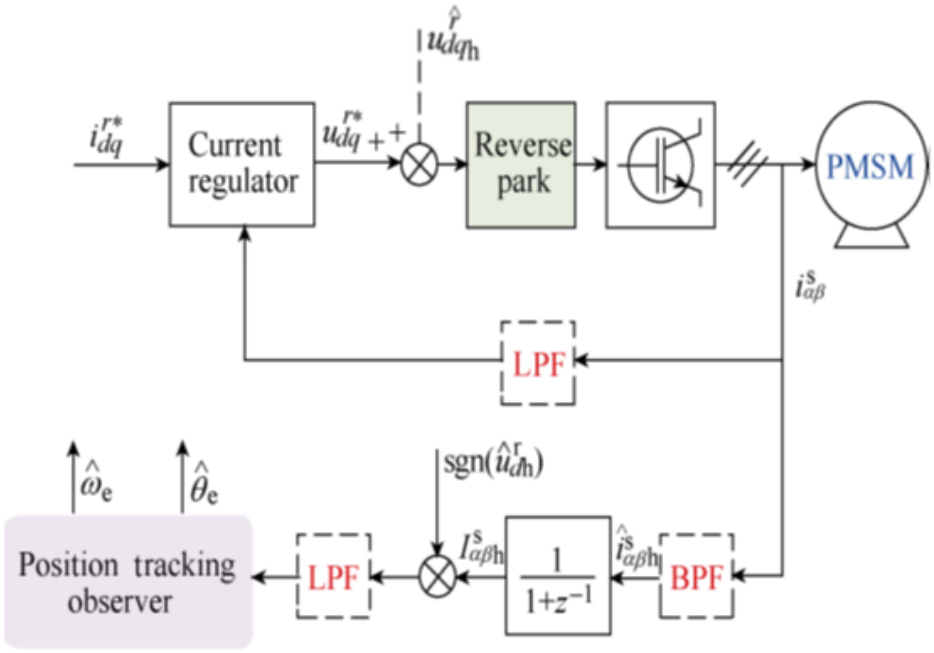

Figure 3.10. Square Wave Injection Block Diagram [53]

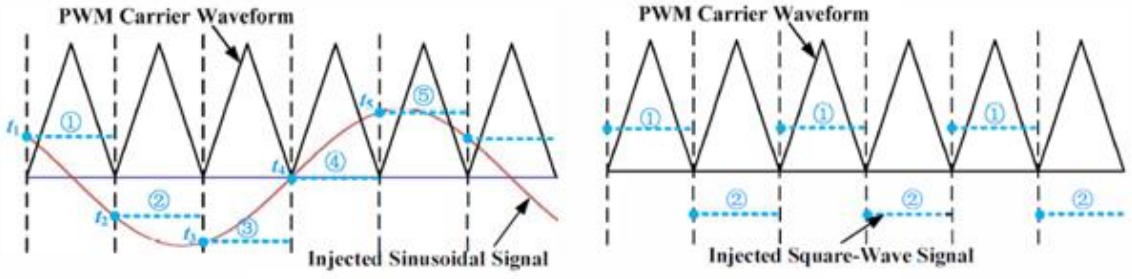

Figure 3.11. Bandwidth Comparison between Sinusoidal and Square Injection [55]

CHAPTER FOUR

SIMULINK DEVELOPMENT

MATLAB and Simulink offer an environment to effectively simulate motor control algorithms. More specifically, the Simulink environment offers a motor control and specialized power systems blockset. A PMSM model with saliency is defined in the Simulink workspace to develop the sensorless control simulation, as seen in Figure 4.1. The output of the PMSM block provides information for the speed, position, three-phase current, and torque. This replicates the physical sensors for experimental testing. Figure 4.2 displays the block parameters for the utilized PMSM. The parameters reflect the actual IPMSM used for experimental testing – this includes the stator resistance and rotating reference frame inductance. The PMSM is driven by a three-phase inverter, which is also set with a Simulink power electronics block. The inverter is driven by six different gate signals, generated from the SVPWM calculations, and has a voltage source connection. The SVPWM duty cycle calculations within the Simulink model can be seen in Figure 4.4. The PI controllers convert current references into voltage references understandable for SVPWM calculations. PI parameters can be defined in terms related to the inductance, stator resistance, and controller bandwidth.

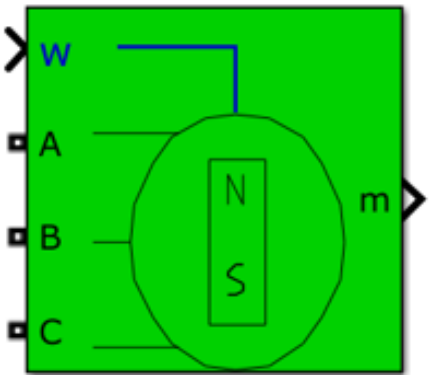

Figure 4.1. PMSM Simulink Block

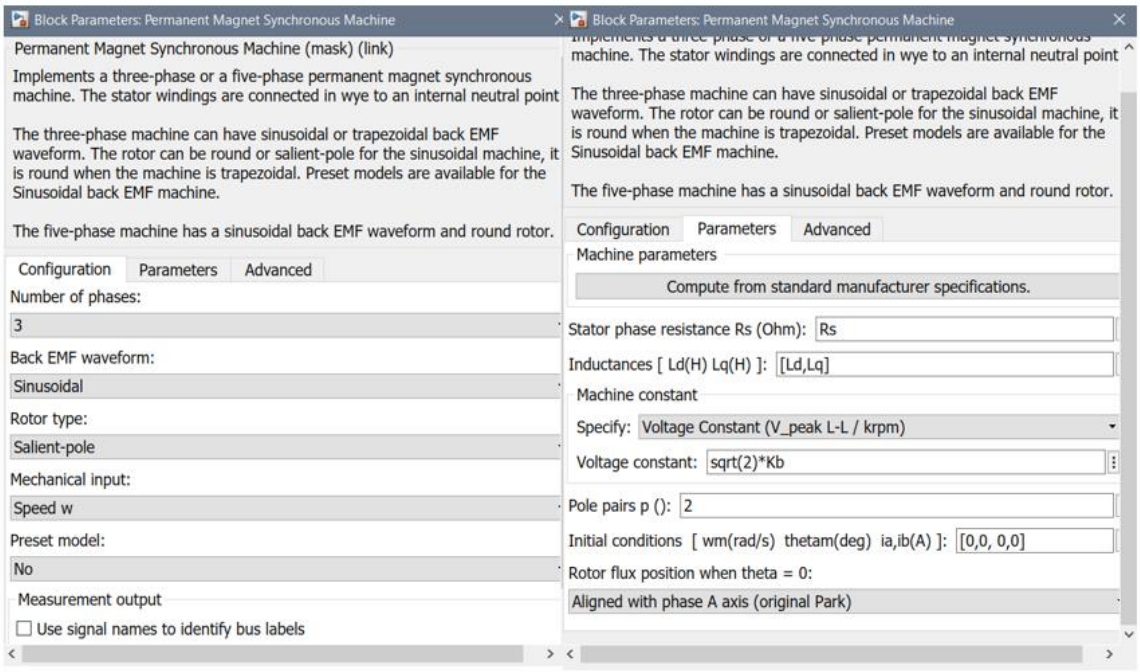

Figure 4.2. PMSM Block Parameters

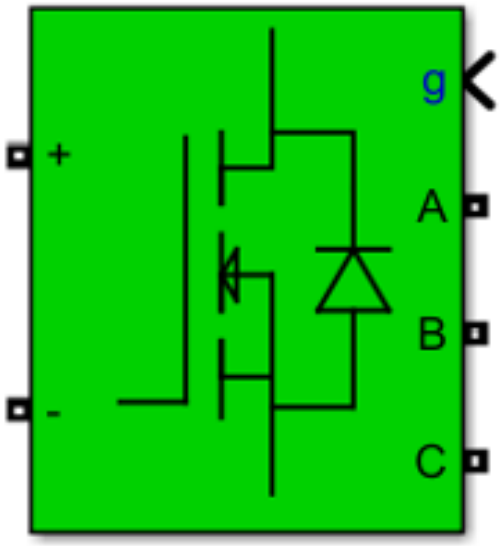

Figure 4.3. Three-Phase Inverter Simulink Block

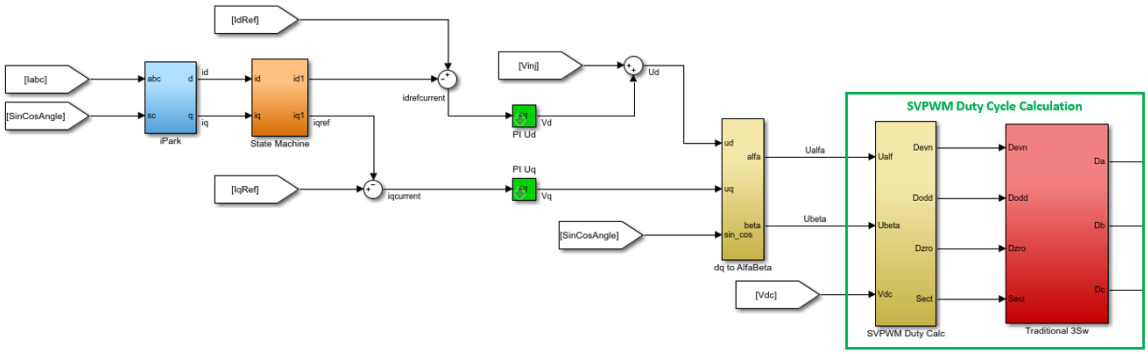

Figure 4.4. Duty Cycle Calculations

Sensorless Control Model

Within the Simulink environment, the pulsating sinusoidal signal injection method is utilized for sensorless control. A sinusoidal voltage, V_{inj}, is superimposed onto the direct axis; the three-phase current is then sampled and sent to the HFI observer as an input. The estimated position is also sent as an input to the HFI observer. Within the HFI observer, the three-phase current is passed through a bandpass filter centered at the injection frequency to extract the position dependent current. The simulation parameter, F_{inj}, defines the injected frequency. The bandpass filter can be represented as a second order transfer function as shown in Equation (4.1) [58]. The damping factor, δ, is set to 0.2 to modify the quality factor of the bandpass filter.

$$G(\mathcal{s}) = \frac{\delta\left(2\pi F_{inj}\right)\mathcal{s}}{\mathcal{s}^2 + \delta\left(2\pi F_{inj}\right)\mathcal{s} + 4\pi^2 F_{inj}^2} \tag{4.1}$$

A bode plot is displayed in Figure 4.5 in which the injected frequency is set to 500 Hz. Figure 4.6 displays a bode plot for a bandpass filter centered at 1 kHz, Figure 4.7 displays a bode plot for a bandpass filter centered at 2 kHz, and Figure 4.8 displays a bode plot for a bandpass filter centered at 4 kHz. Figure 4.9 displays the implemented bandpass filter in Simulink, as the three-phase current is passed into their respective filters. A Park transformation is then made to convert I_{abc} to I_{dq}. The electrical angle used for this calculation is the estimated electrical angle. Simulink calculations are then shown in Figure 4.10 for the Park transformation.

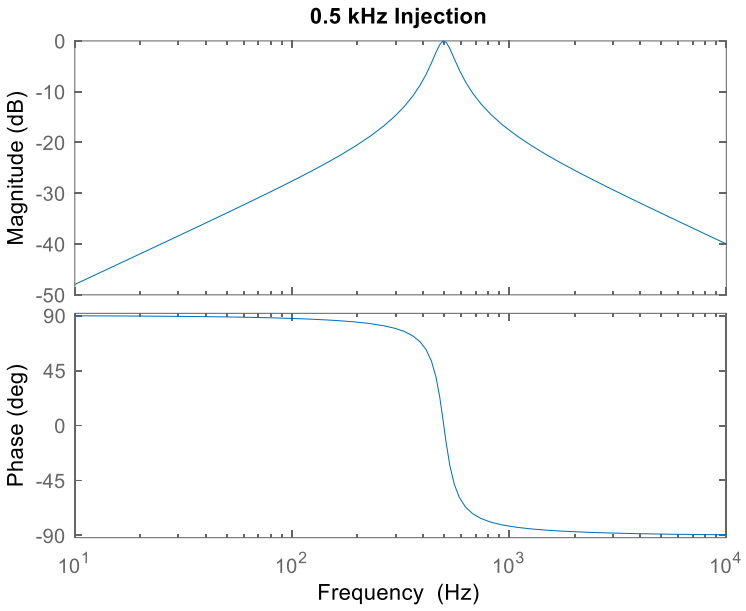

Figure 4.5. 500 Hz Bandpass Filter Bode Plot

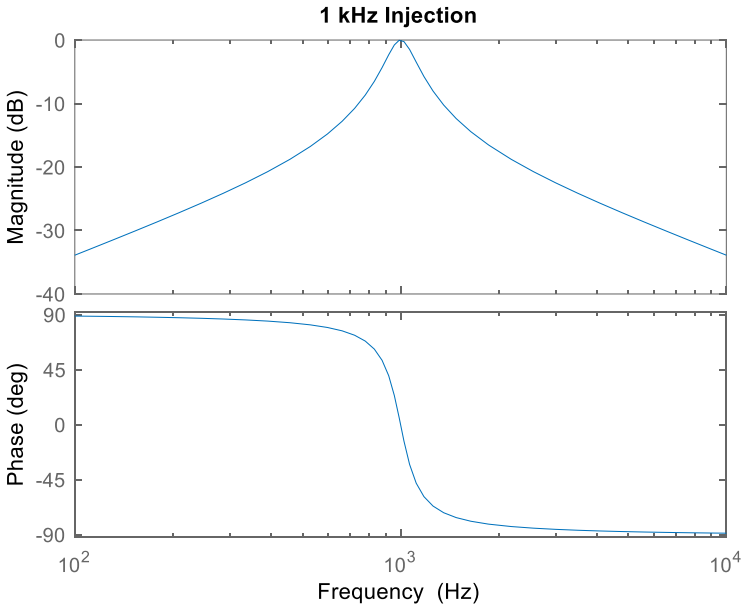

Figure 4.6. 1 kHz Bandpass Filter Bode Plot

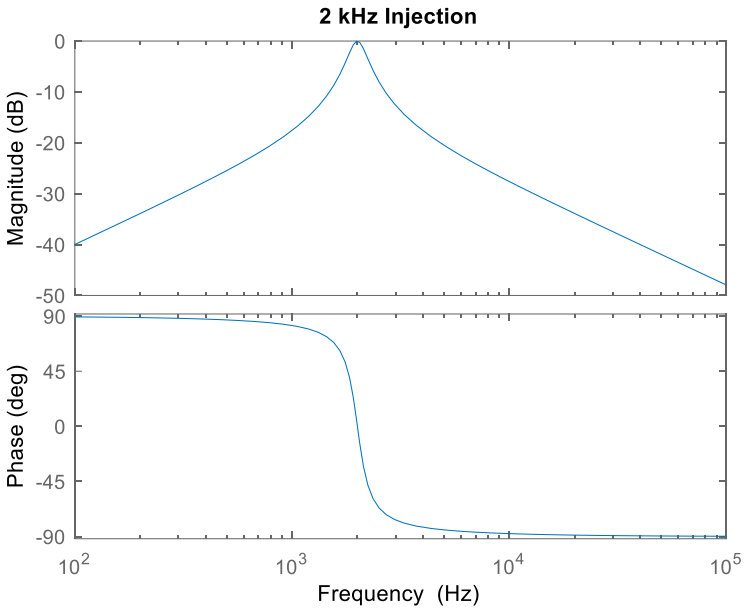

Figure 4.7. 2 kHz Bandpass Filter Bode Plot

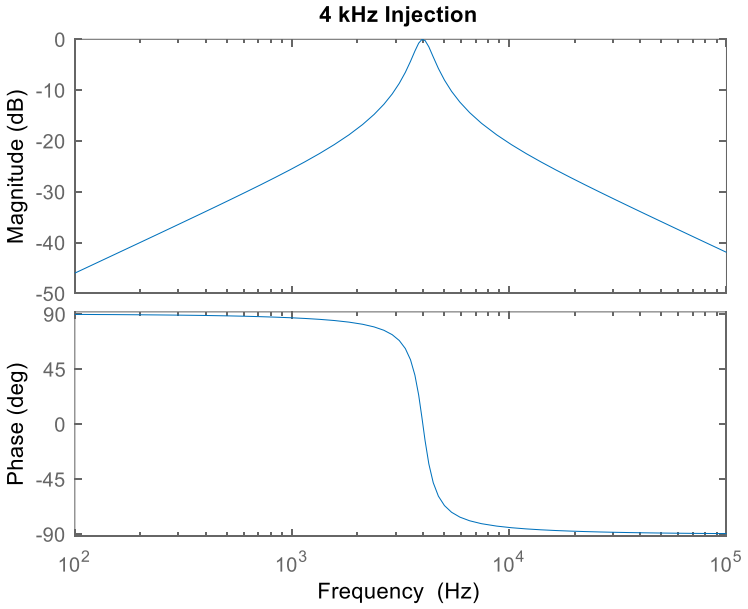

Figure 4.8. 4 kHz Bandpass Filter Bode Plot

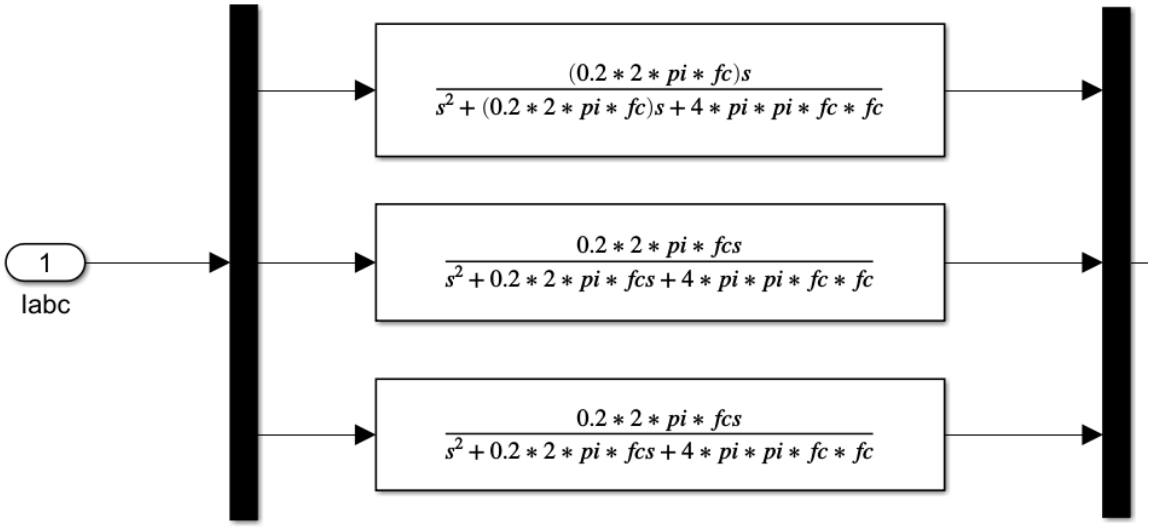

Figure 4.9. Bandpass Filter Transfer Function in Simulink

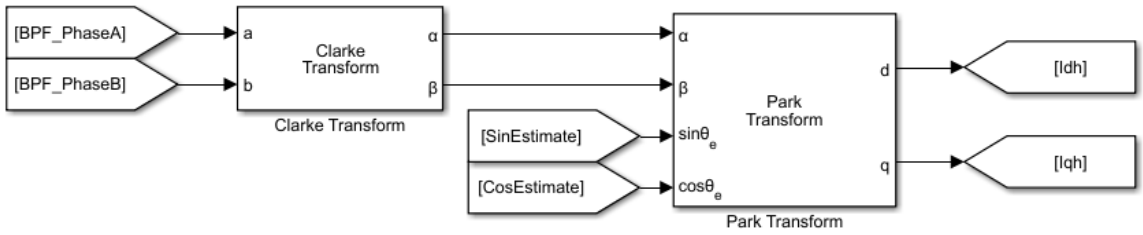

Figure 4.10. Simulink Park Transformation

To retrieve the position information, I_{qh} is multiplied by $\sin 2\pi F_{inj} t$ and then passed through a low-pass filter; the low-pass filter has a cutoff frequency of 150 Hz. While the bandpass filter is mindful of the injected frequency, the low-pass filter must also account for the injection frequency. The low-pass filter is designed as a second order transfer function described by Equation (4.2) [58]. Additionally, the bode plot for the low-pass filter is shown in Figure 4.11. A damping factor is set to 0.707 for the low-pass filter.

$$G(s) = \frac{4\pi^2 F_{cut}^2}{s^2 + \frac{1}{\sqrt{2}}(2\pi F_{cut})2s + 4\pi^2 F_{cut}^2} \tag{4.2}$$

The output of the low-pass filter is then set as the input to a PI controller for speed tracking. The speed estimation is then integrated to provide an electrical rotor position. Figure 4.12 shows the Simulink block for a PI controller and integrator connected to complete the HFI observer. Once the simulation environment is setup, variables can be adjusted and an analysis can be made to evaluate the final position estimation. The next section will document simulations results. Additionally, the current response with the bandpass filter and low-pass filter are displayed.

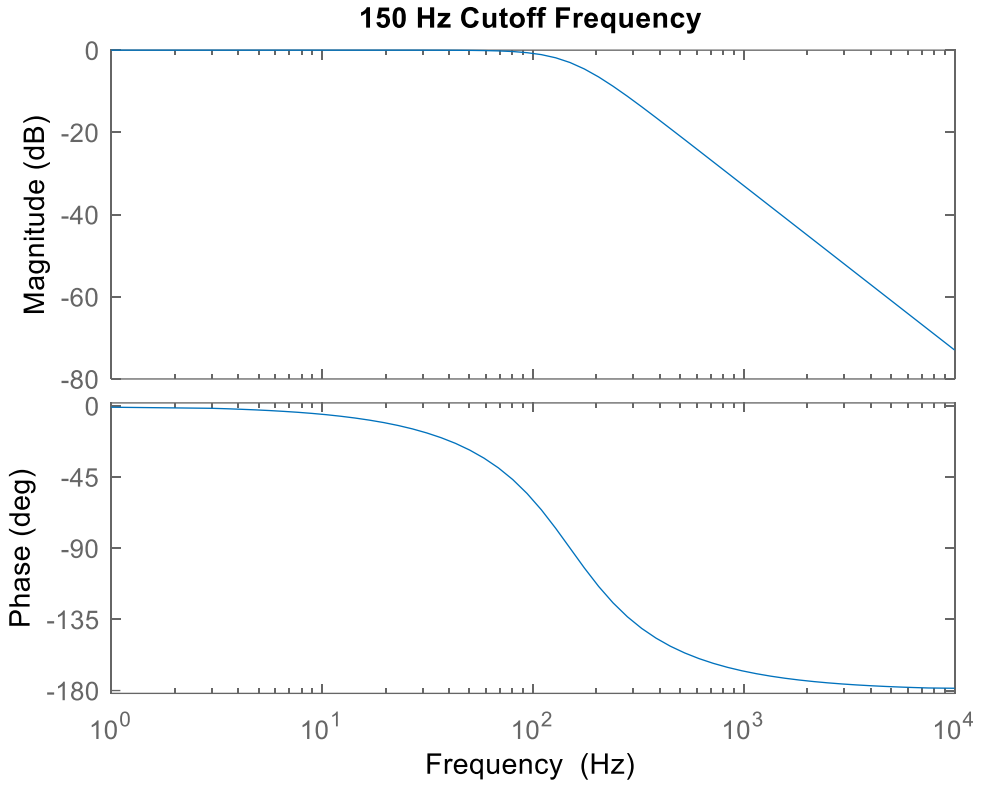

Figure 4.11. Low-Pass Filter Bode Plot

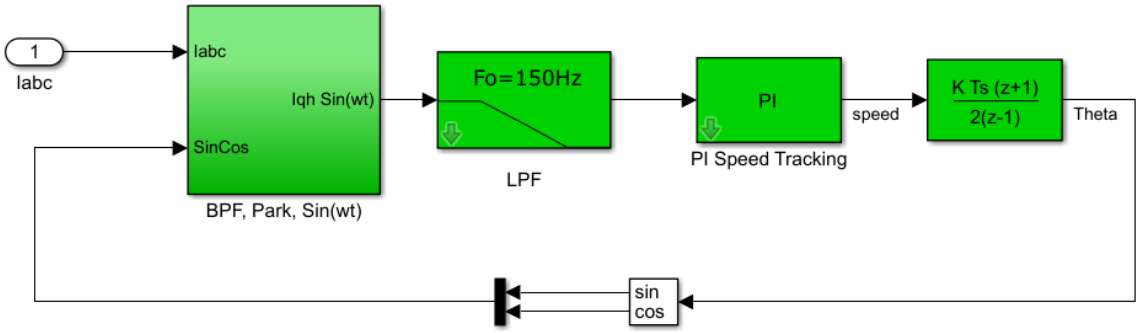

Figure 4.12. Closed Loop Position Estimation

Sensorless Control Simulation Results

Simulations were conducted to verify the HFI sensorless control algorithm. Additionally, variables of interest – summarized in Table 4.1 - were modified to evaluate the resulting angle error. The injection frequency ranges from 500 Hz to 4 kHz. The voltage injection amplitude ranges from 10 Volts to 40 Volts, and the switching frequency ranges from 5 kHz to 60 kHz. High switching frequencies, thus, enable SiC power devices. The first set of simulations operate at 150 RPM and 25 Volts injected. The switching frequency is modified between simulations. Figure 4.13 displays the measured and estimated electrical angle of the rotor for a 500 Hz sinusoidal injection, ranging from 0 to 2π radians. A significant overlap in the signals imply an acceptable position estimation. The resulting speed estimation, measured speed, and calculated angle error between the real position and the estimated position are shown in Figure 4.14 at a 5 kHz switching frequency. A 5 kHz switching frequency in these simulations also indicates that all signals are sampled and calculations are made at the same rate. Figure 4.15 and Figure 4.16 demonstrate the angle error results as the switching frequency is changed to 20 kHz. Figure 4.17 and Figure 4.18 communicate the angle error results for a 1 kHz sinusoidal injection signal with the switching frequency at 10 kHz while Figure 4.19 and Figure 4.20 change the switching frequency to 20 kHz. The injection frequency is then increased to 2 kHz, with data shown for a 5 kHz switching frequency in Figure 4.21 and Figure 4.22 and a 20 kHz switching frequency in Figure 4.23 and Figure 4.24.

Table 4.1. Simulation Parameter Variations

Parameter	Values	Unit
F_{inj}	500, 1000, 2000, 4000	Hz
V_{inj}	10, 25, 40	V
F_{sw}	5, 10, 20, 40, 60	kHz
Speed Reference	150, 300	RPM
L_d Inductance	12	mH
L_q Inductance	34	mH
Stator Resistance	6.98	Ω
DC Bus Voltage	150	V

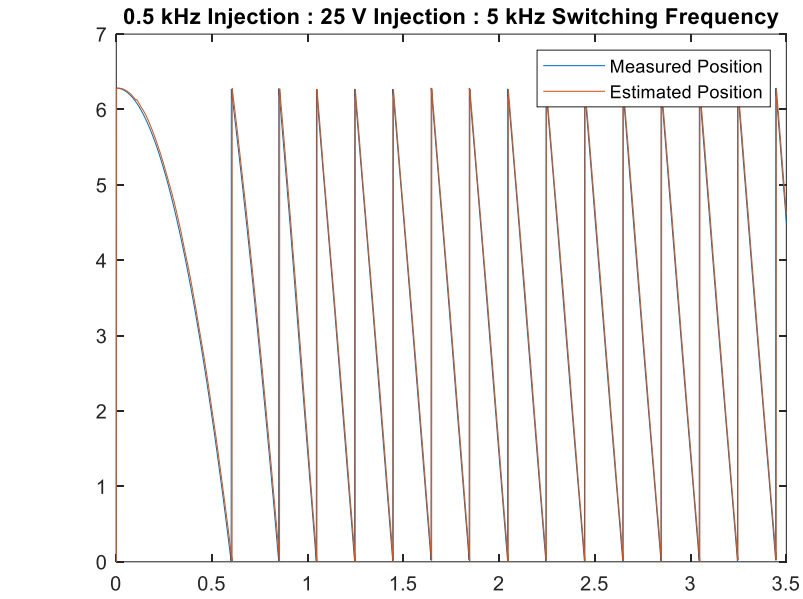

Figure 4.13. 500 Hz, 25 V Sine Injection at 5 kHz Switching: Position Data

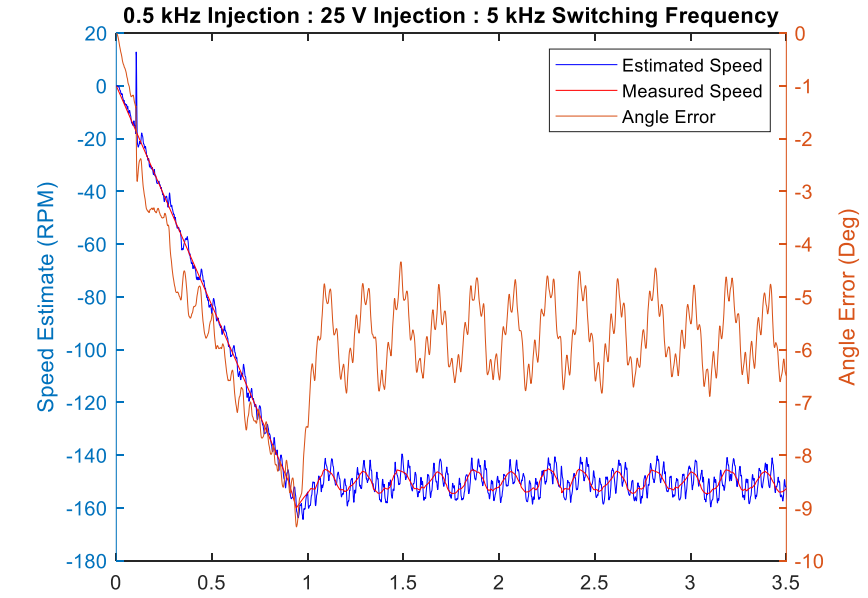

Figure 4.14. 500 Hz, 25 V Sine Injection at 5 kHz Switching: Speed and Angle Error

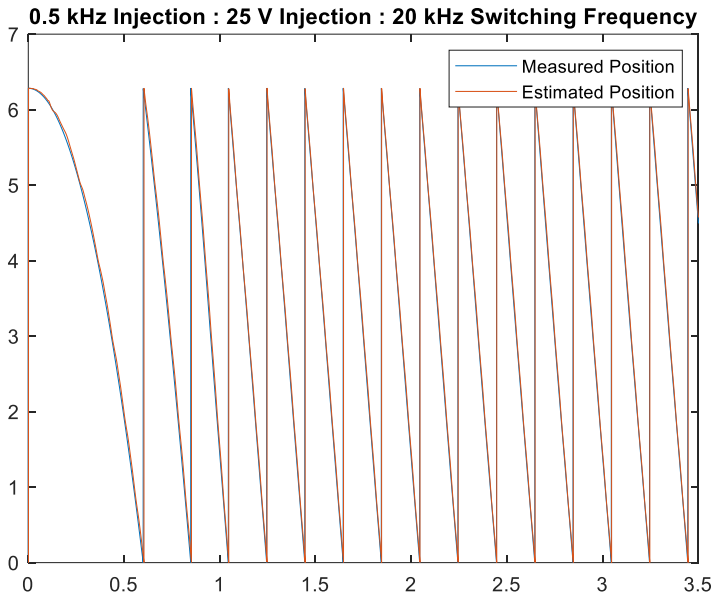

Figure 4.15. 500 Hz, 25 V Sine Injection at 20 kHz Switching: Position Data

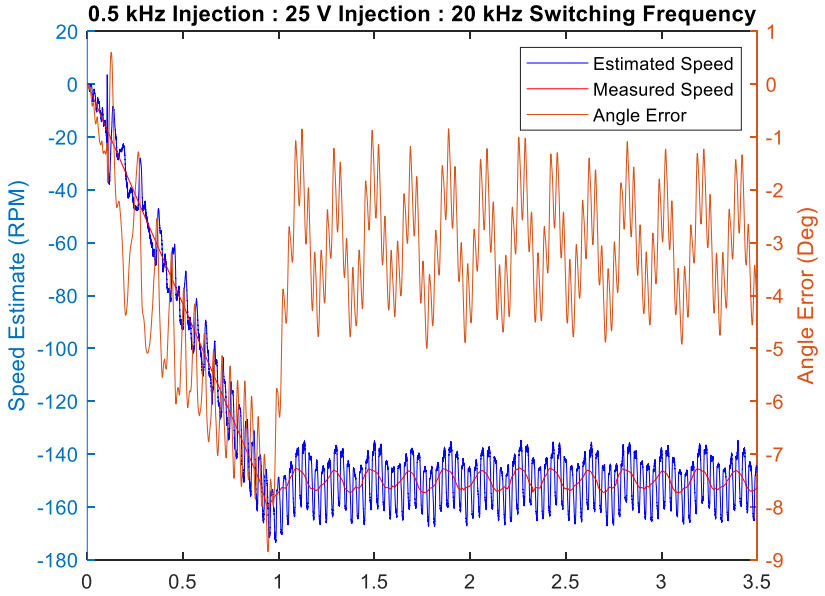

Figure 4.16. 500 Hz, 25 V Sine Injection at 20 kHz Switching: Speed and Angle Error

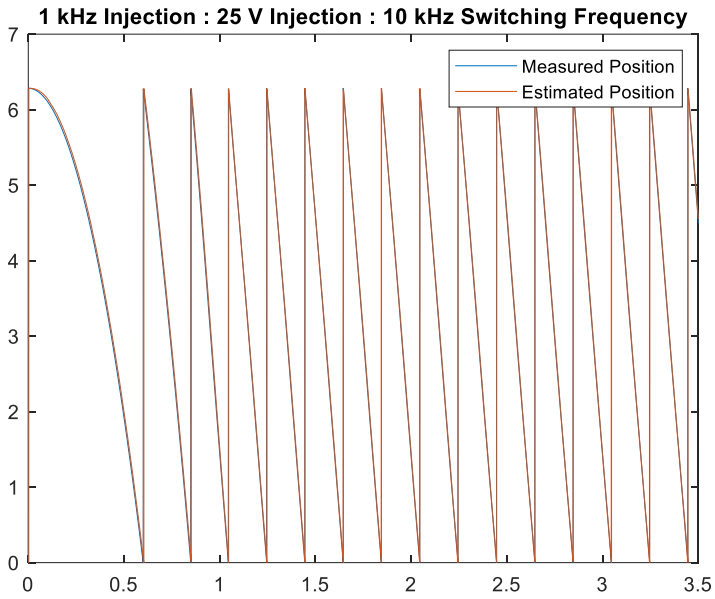

Figure 4.17. 1 kHz, 25 V Sine Injection at 10 kHz Switching: Position Data

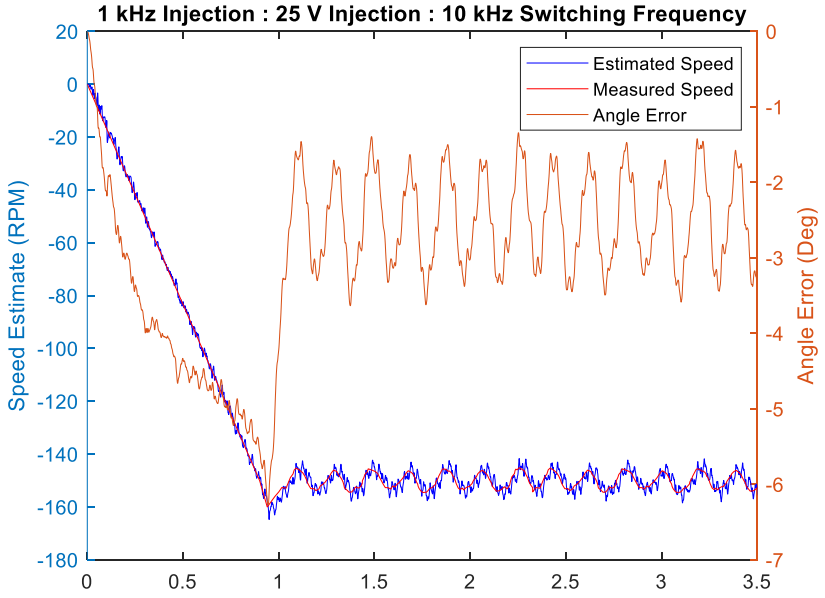

Figure 4.18. 1 kHz, 25 V Sine Injection at 10 kHz Switching: Speed and Angle Error

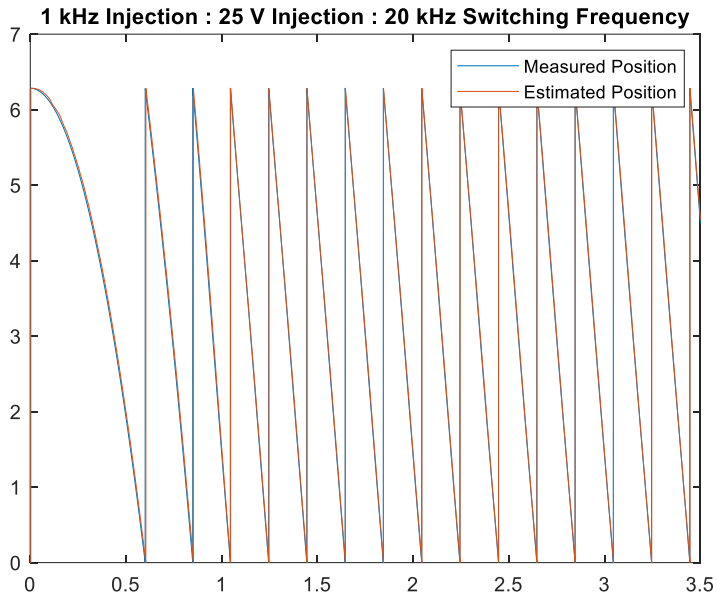

Figure 4.19. 1 kHz, 25 V Sine Injection at 20 kHz Switching: Position Data

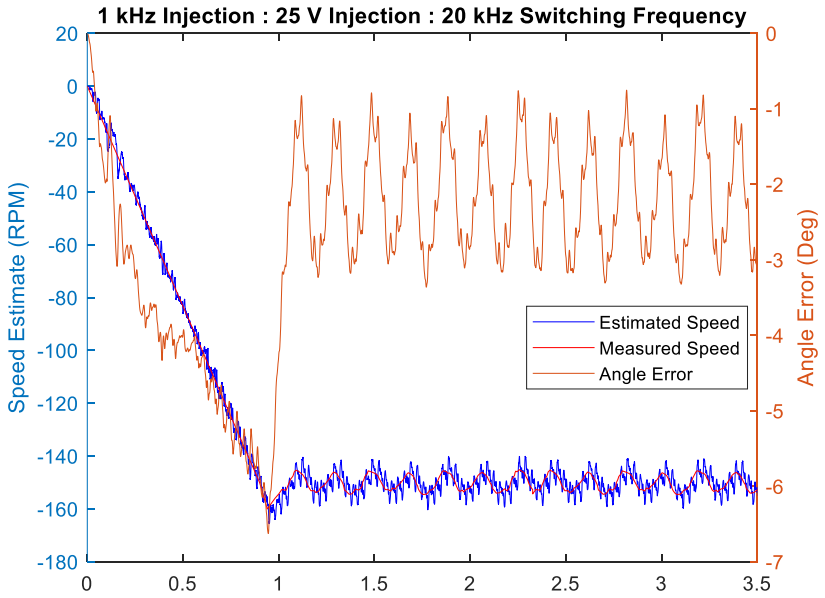

Figure 4.20. 1 kHz, 25 V Sine Injection at 20 kHz Switching: Speed and Angle Error

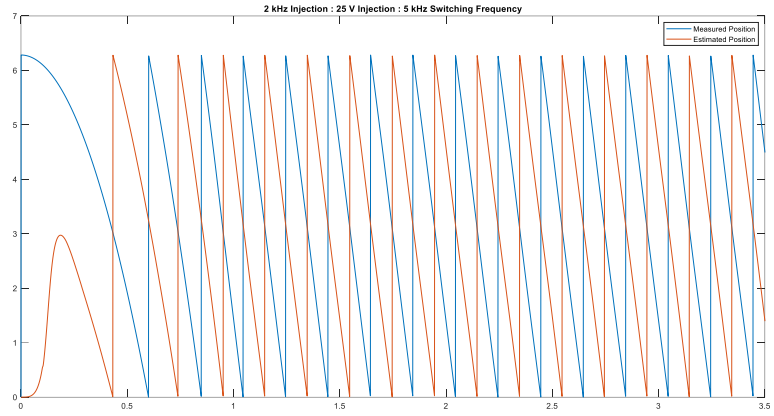

Figure 4.21. 2 kHz, 25 V Sine Injection at 5 kHz Switching: Position Data

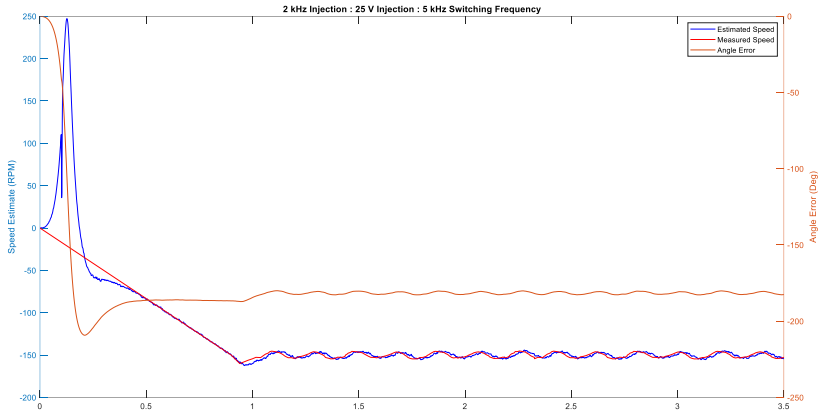

Figure 4.22. 2 kHz, 25 V Sine Injection at 5 kHz Switching: Speed and Angle Error

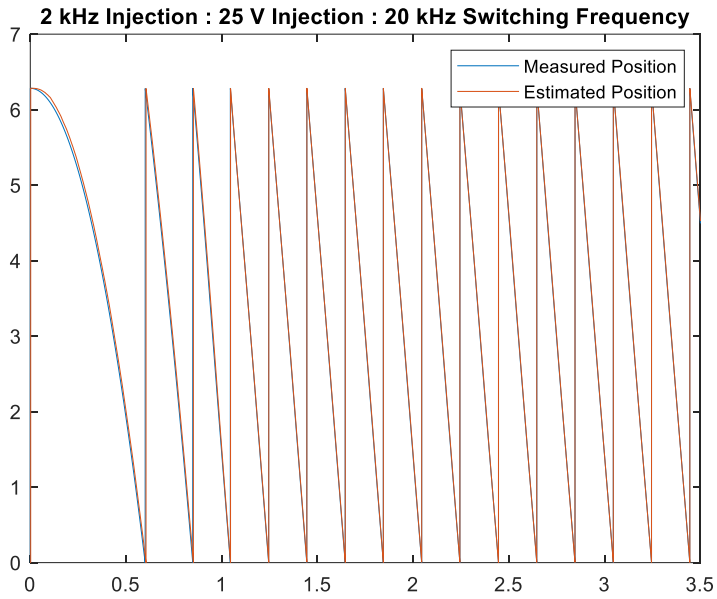

Figure 4.23. 2 kHz, 25 V Sine Injection at 20 kHz Switching: Position Data

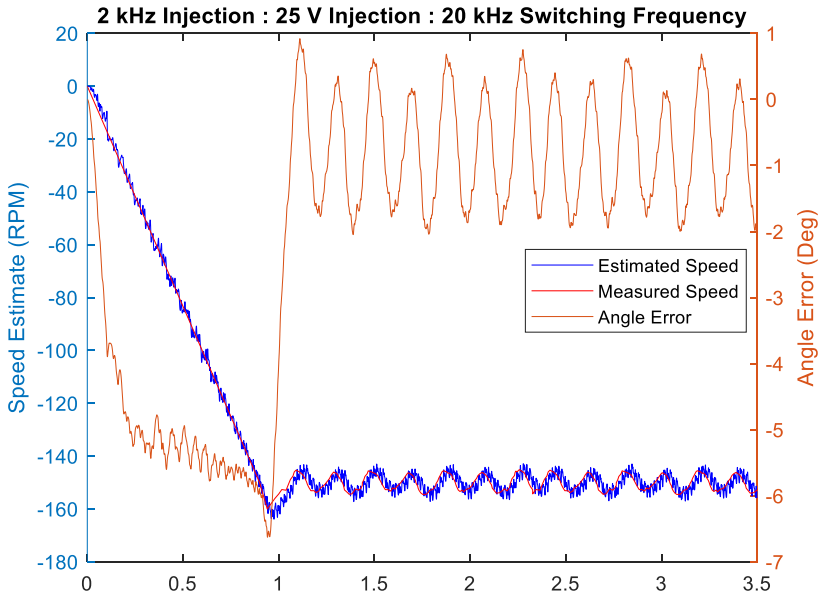

Figure 4.24. 2 kHz, 25 V Sine Injection at 20 kHz Switching: Speed and Angle Error

Evident in Figure 4.22, the injection frequency and switching frequency are too close and the resulting angle error does not converge to an appropriate angle error. Figure 4.25 and Figure 4.26 demonstrate a 500 Hz injection and 5 kHz switching frequency with the speed reference increased from 150 RPM to 300 RPM. Figure 4.27 and Figure 4.28 demonstrate the angle error for a 500 Hz sinusoidal injection with a 20 kHz switching frequency while the rotor operates at 300 RPM. The injection frequency is increased to 2 kHz, and Figure 4.29 and Figure 4.30 show the resulting angle error for a 20 kHz switching frequency. The switching frequency is then increased to 40 kHz for a 2 kHz injection signal with Figure 4.31 and Figure 4.32 documenting the angle error. At the steady-state reference speed for both 150 RPM and 300 RPM data, the peak to peak angle error oscillation is similar for each injection frequency and switching frequency. However, the angle error presents a DC offset at steady-state that increases with an increase in speed. Figure 4.33 shows the resulting bias for 150 RPM and 300 RPM simulations for a 500 Hz, 1 kHz, and 2 kHz injection at a 20 kHz switching frequency. At 150 RPM, each injection frequency shows a small DC offset; however, that offset becomes considerably more negative for the 500 Hz injection signal at 300 RPM while a 1 kHz and 2 kHz injection signal only becomes more negative by a couple of degrees. Figure 4.34 depicts the peak angle error as the rotor accelerates from standstill to 300 RPM, introducing a relationship that the injection voltage now has with the estimated electrical angle.

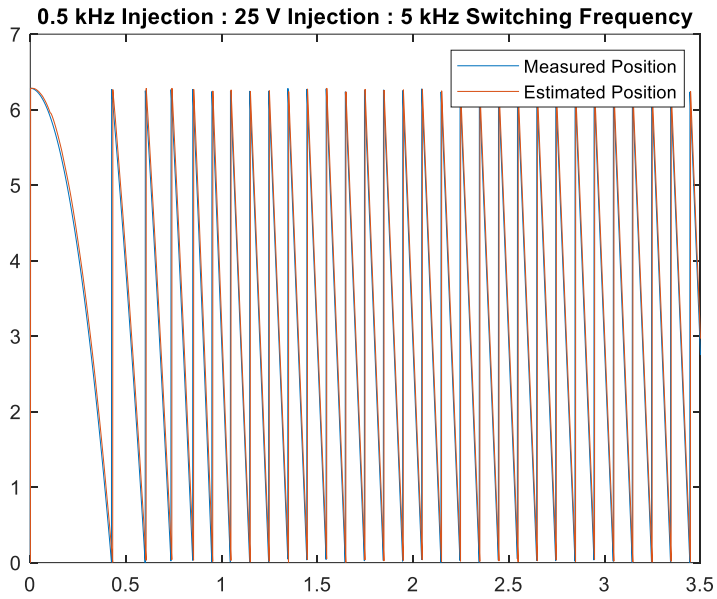

Figure 4.25. 500 Hz, 25 V Sine Injection at 5 kHz Switching: Position Data

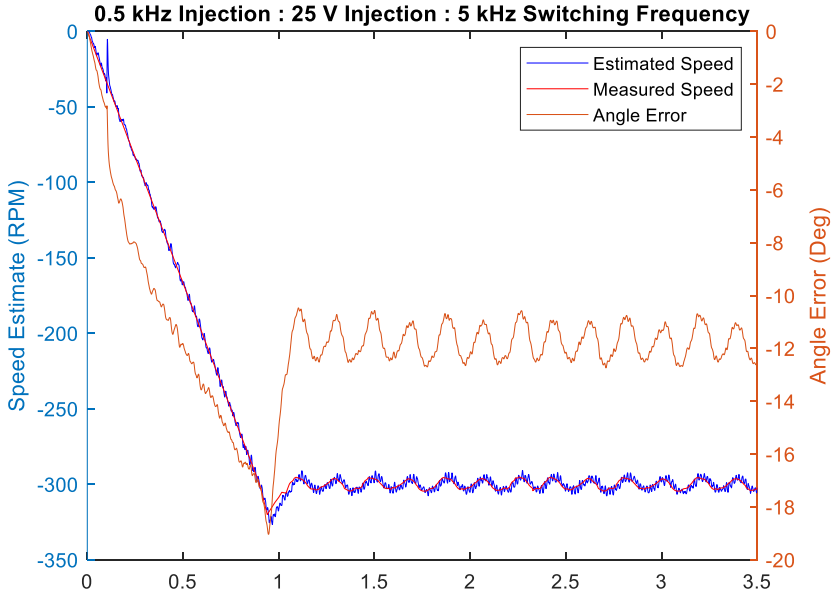

Figure 4.26. 500 Hz, 300 RPM at 5 kHz Switching: Speed and Angle Error

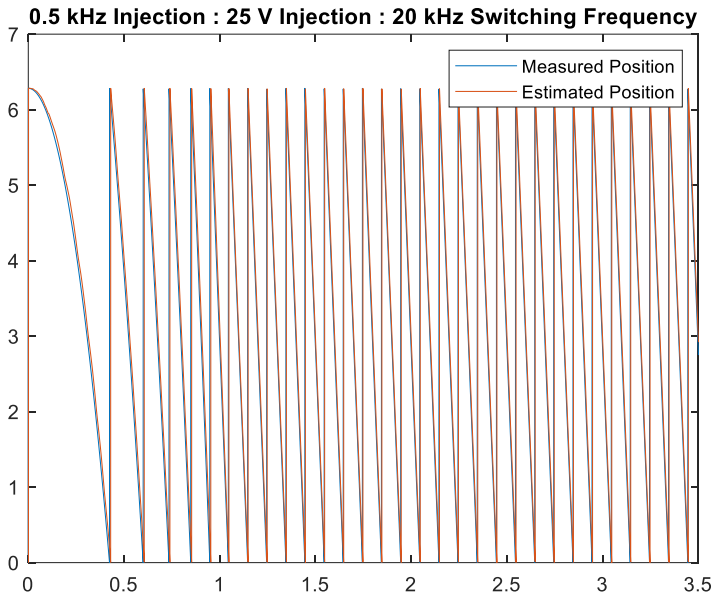

Figure 4.27. 500 Hz Injection, 300 RPM at 20 kHz Switching: Position Data

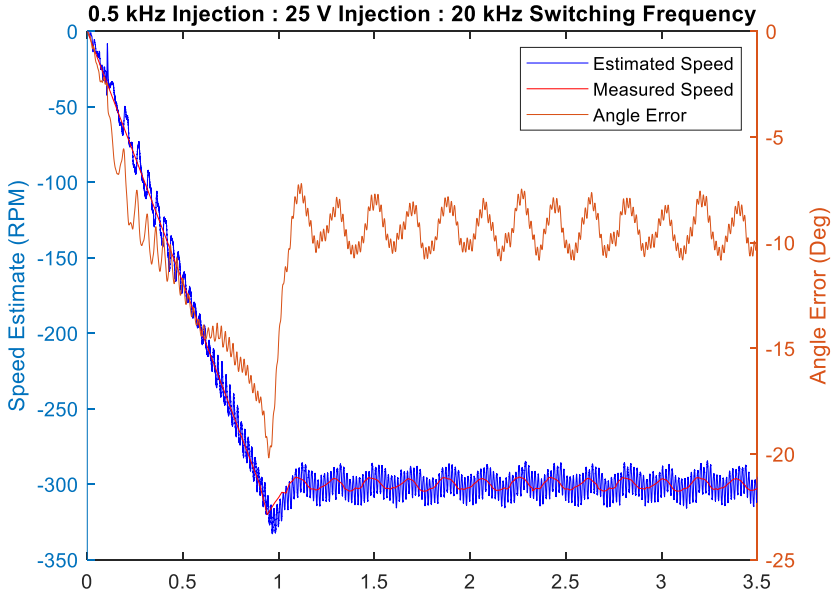

Figure 4.28. 500 Hz Injection, 300 RPM at 20 kHz Switching: Speed and Angle Error

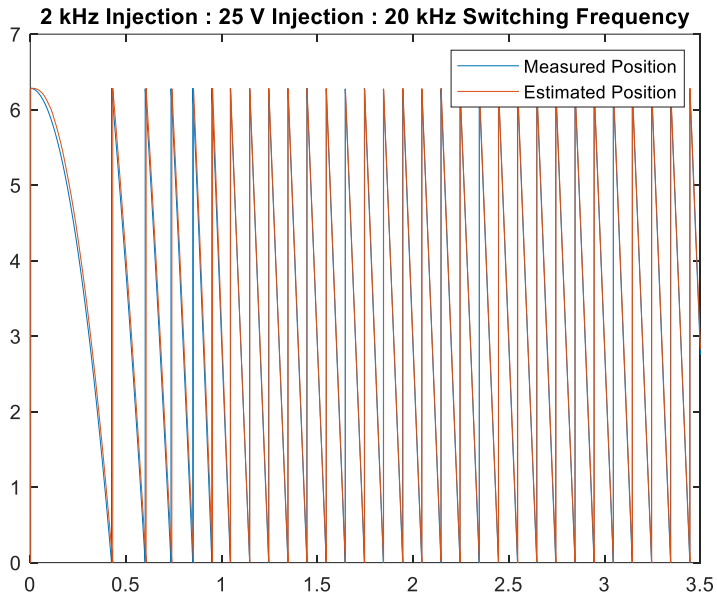

Figure 4.29. 2 kHz Injection, 300 RPM at 20 kHz Switching: Position Data

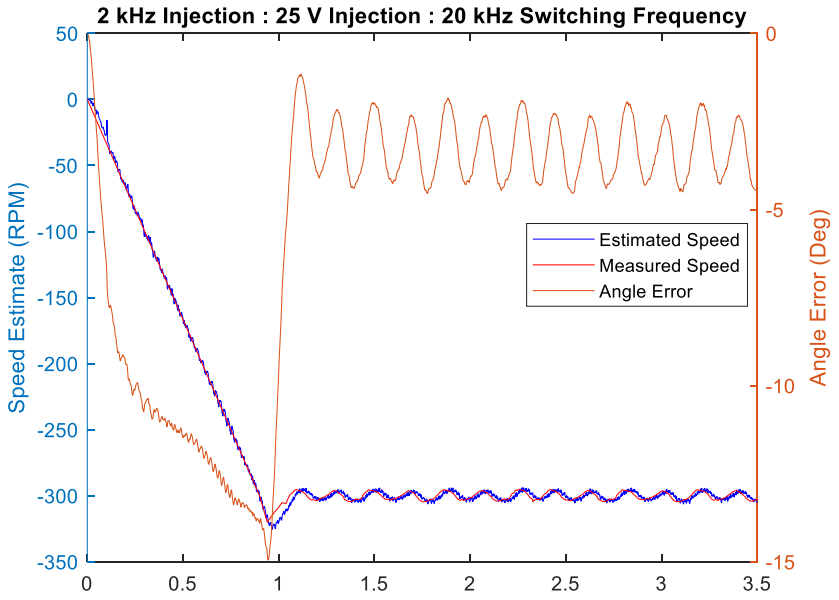

Figure 4.30. 2 kHz Injection, 300 RPM at 20 kHz Switching: Speed and Angle Error

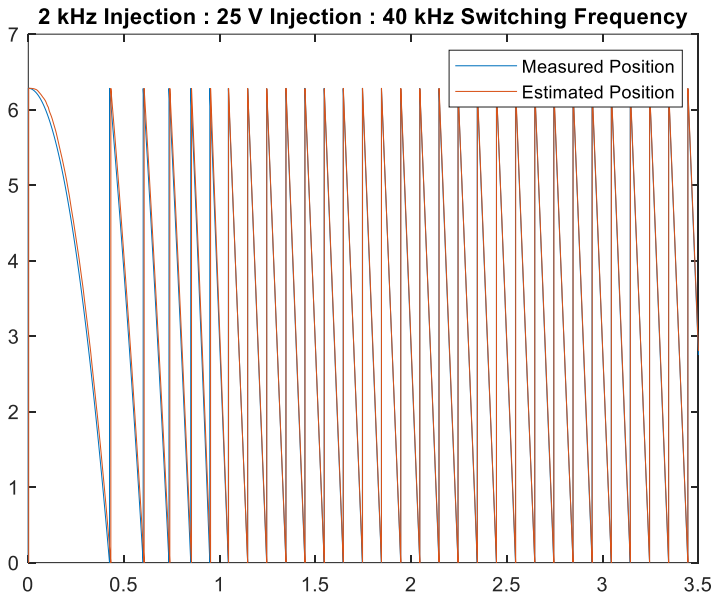

Figure 4.31. 2 kHz Injection, 300 RPM at 40 kHz Switching: Position Data

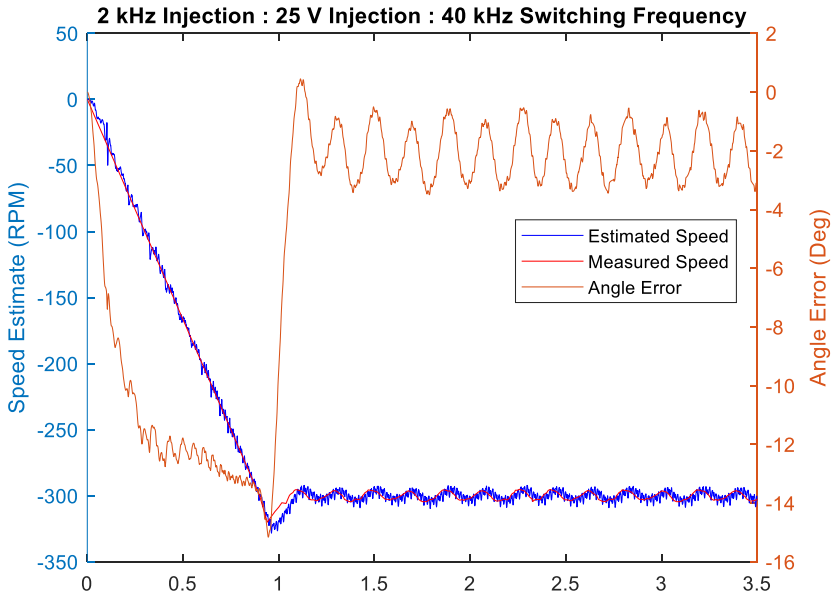

Figure 4.32. 2 kHz Injection, 300 RPM at 40 kHz Switching: Speed and Angle Error

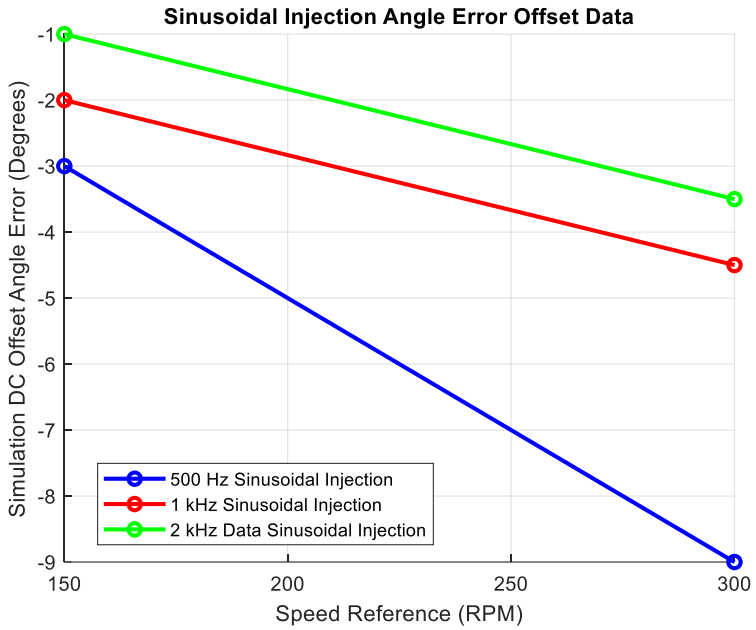

Figure 4.33. DC Angle Error Offset at 150 RPM and 300 RPM

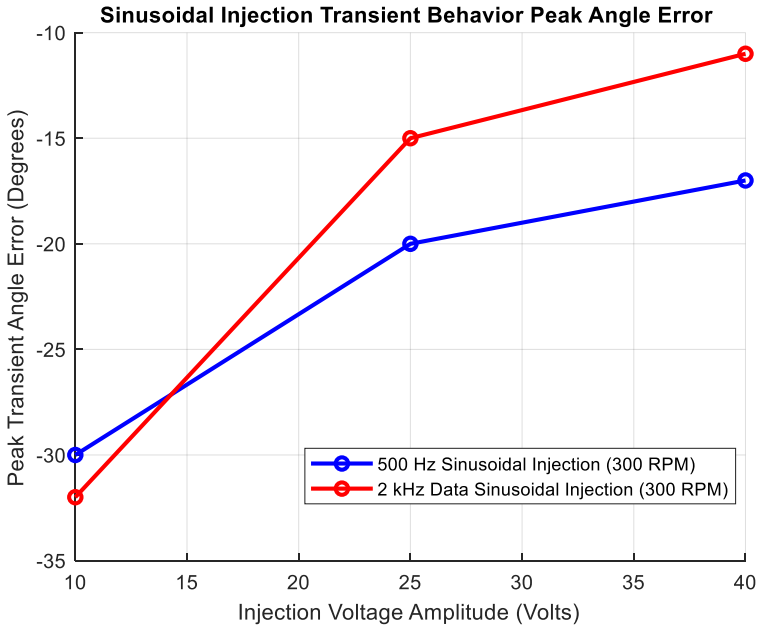

Figure 4.34. Acceleration from 0 to 300 RPM: Peak Angle Error

Recall Equation (3.42) where the saliency current is introduced as the input to the PI speed tracking controller. This equation can be rearranged and shown in Equation (4.3). ω_{inj}, I_{sal}, and V_{inj} are coupled together in HFI sensorless control. ω_{inj} will show up in the impedance, while I_{sal} will be induced from V_{inj} and its amplitude will depend on the impedance associated with ω_{inj}.

$$\frac{2\omega_{inj}I_{sal}}{V_{inj}}\frac{L_qL_d}{L_q-L_d}=\sin 2\theta_{err} \tag{4.3}$$

In the transient response of the PI speed tracking controller, there is a time delay related to the control system independent of the HFI parameters. To compensate for the control system response delay, increasing the injection voltage can improve the dynamic response angle error, which was shown in Figure 4.34. Increasing the injection voltage amplitude improves the electrical angle estimation as the signal to noise ratio (SNR) is improved in the transient process. As the phase current sampling is critical in achieving the estimated electrical angle, figures are presented to illustrate these waveforms. Figure 4.35 shows a single-phase current in blue and the output of that same single-phase current from the bandpass filter in red. The bandpass filter current is created from the induced injection current while also demonstrating a frequency corresponding to the fundamental frequency of the rotor. The filtered current waveform demonstrates the saliency of the IPMSM. Figure 4.36 and Figure 4.37 demonstrate the converted bandpass filter current to the $d-q$ reference frame oscillating at 500 Hz, which corresponds to the injection frequency. The saliency

current is shown in Figure 4.38 and Figure 4.39 to display the signal used by the speed estimation controller.

Summary

Simulations provide excellent insight into the performance of the constructed HFI sensorless control algorithm. Relationships between the fundamental frequency, injection frequency, and switching frequency with the electrical angle error are investigated. Additionally, the influence of the injection voltage and speed reference on the electrical angle error are studied. 1) It can be seen that the switching frequency must be larger than the injection frequency. The bandpass filter design must account for the switching frequency and maximum rotor fundamental frequency, ensuring the quality factor is narrow enough to secure only the injection frequency response in the filtered phase currents. Additionally, with the duty cycle updated at the same rate of the switching frequency, the resolution of the sinusoidal voltage injected depends on the switching frequency. As the switching frequency is reduced closer to the injection frequency, additional harmonic content is introduced into the motor that is not used for the angle error estimation. 2) Increasing the injection frequency can improve the steady-state angle error as the steady-state speed reference is increased. This is beneficial in reducing the angle error as the sensorless control method nears the transition to a model-based method instead of signal injection. 3) Increasing the injection voltage during periods of acceleration can improve the speed tracking, resulting in an improved angle error.

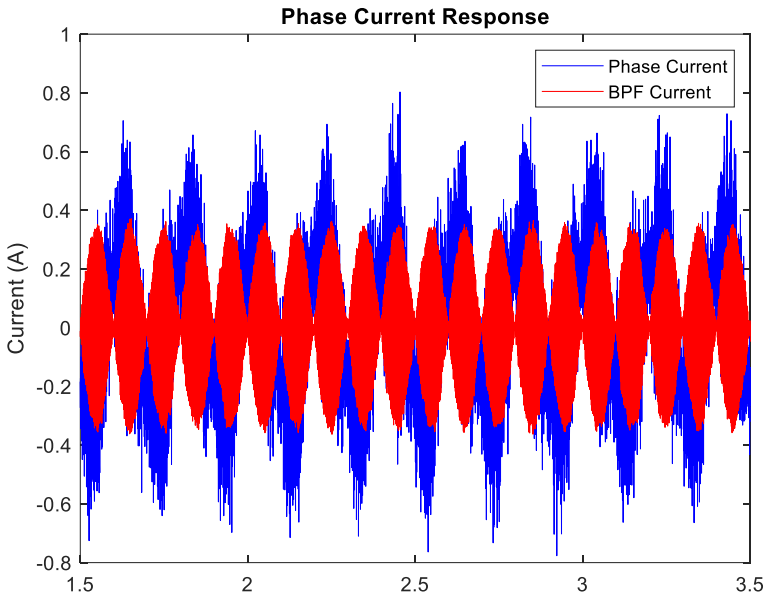

Figure 4.35. 500 Hz Injection Motor Phase Current and BPF Output Current

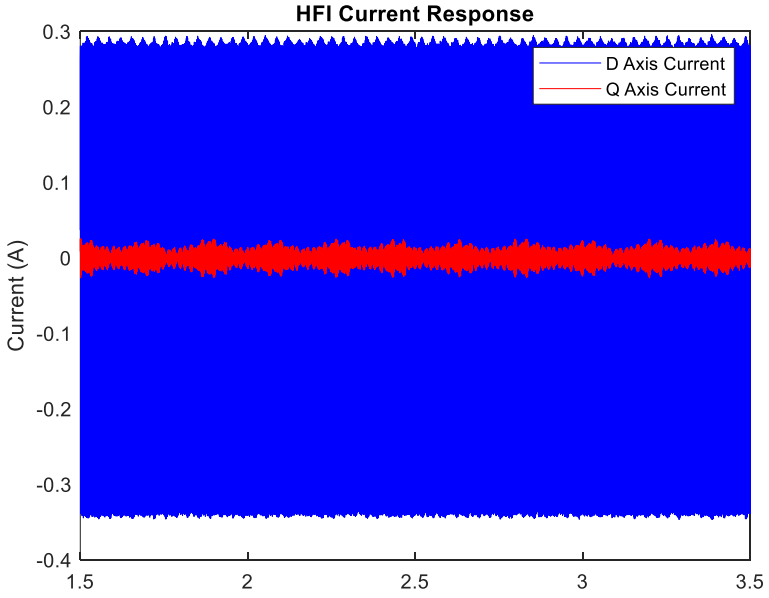

Figure 4.36. 500 Hz Injection DQ HFI Current Response

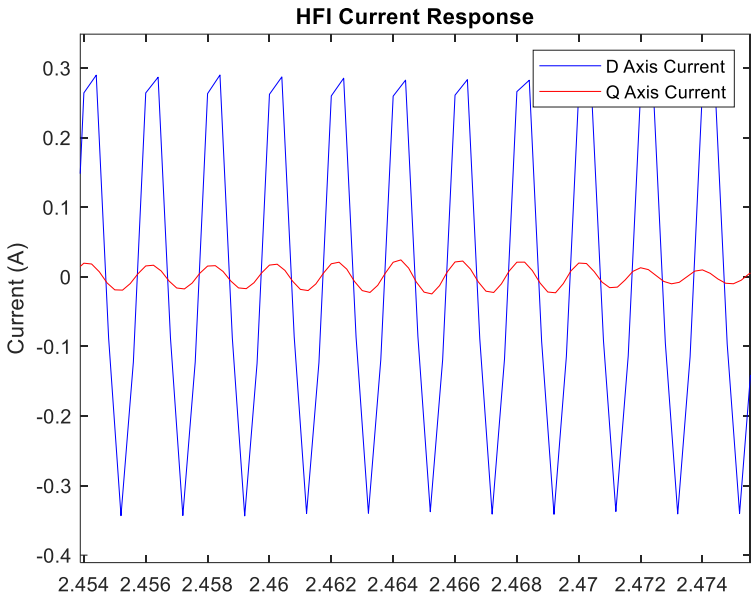

Figure 4.37. 500 Hz Injection DQ HFI Current Response Zoomed In

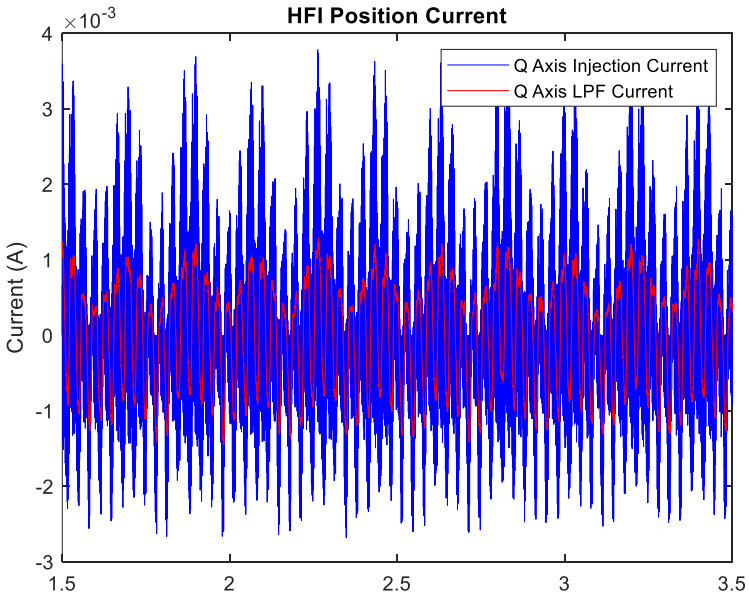

Figure 4.38. Q Axis Current for Position Estimation from LPF

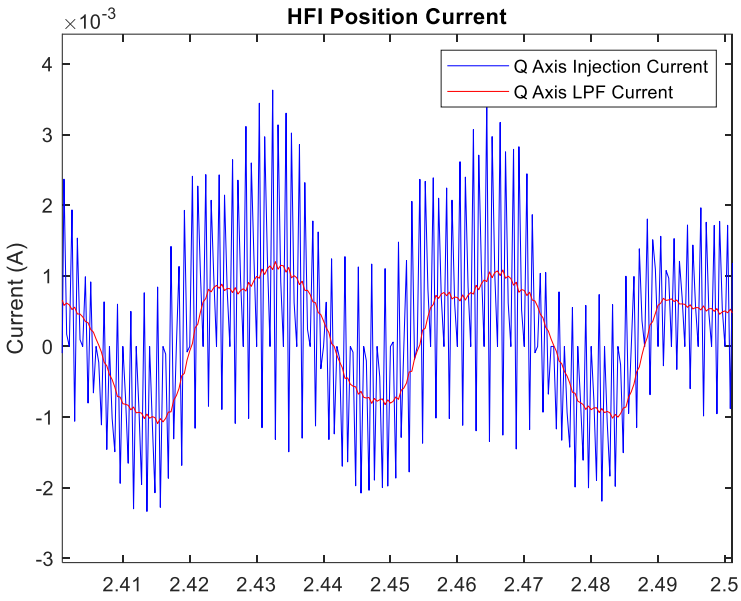

Figure 4.39. Q Axis Current for Position Estimation from LPF Zoomed In

CHAPTER FIVE

FPGA DEVELOPMENT AND EXPERIMENTAL RESULTS

FPGA Development

Upon completing simulations for the developed sensorless control algorithm, FPGA development is needed to interface with the motor drive system. MATLAB and Simulink provide an opportunity for model based programming that can be generated for the FPGA. Within the MathWorks environment, System Generator for DSP enables a model-based Simulink design environment for FPGA Design [59]. By utilizing the HDL Coder Support Package for Xilinx Zynq Platform and Embedded Coder Support Package for Xilinx Zynq Platform in Simulink, VHDL code can be created for the FPGA platform. The Zynq platform is a System-On-Chip (SoC) framework that integrates both FPGA and ARM processing capabilities, which is utilized in the ZedBoard provided in Figure 5.1 [60]. While a DSP provides adequate sensorless control, the series instruction set calculations make it difficult to update the duty cycle once per switching period. Additionally, a computation delay is included within each instruction. The FPGA can minimize this total computational time delay accrued for the sensorless control algorithm.

System Generator for DSP

The System Generator for DSP Simulink programming environment allows the user to specify the intended Xilinx board, hardware description language, and clock settings. The FPGA clock period is set to 10 ns. The Simulink system

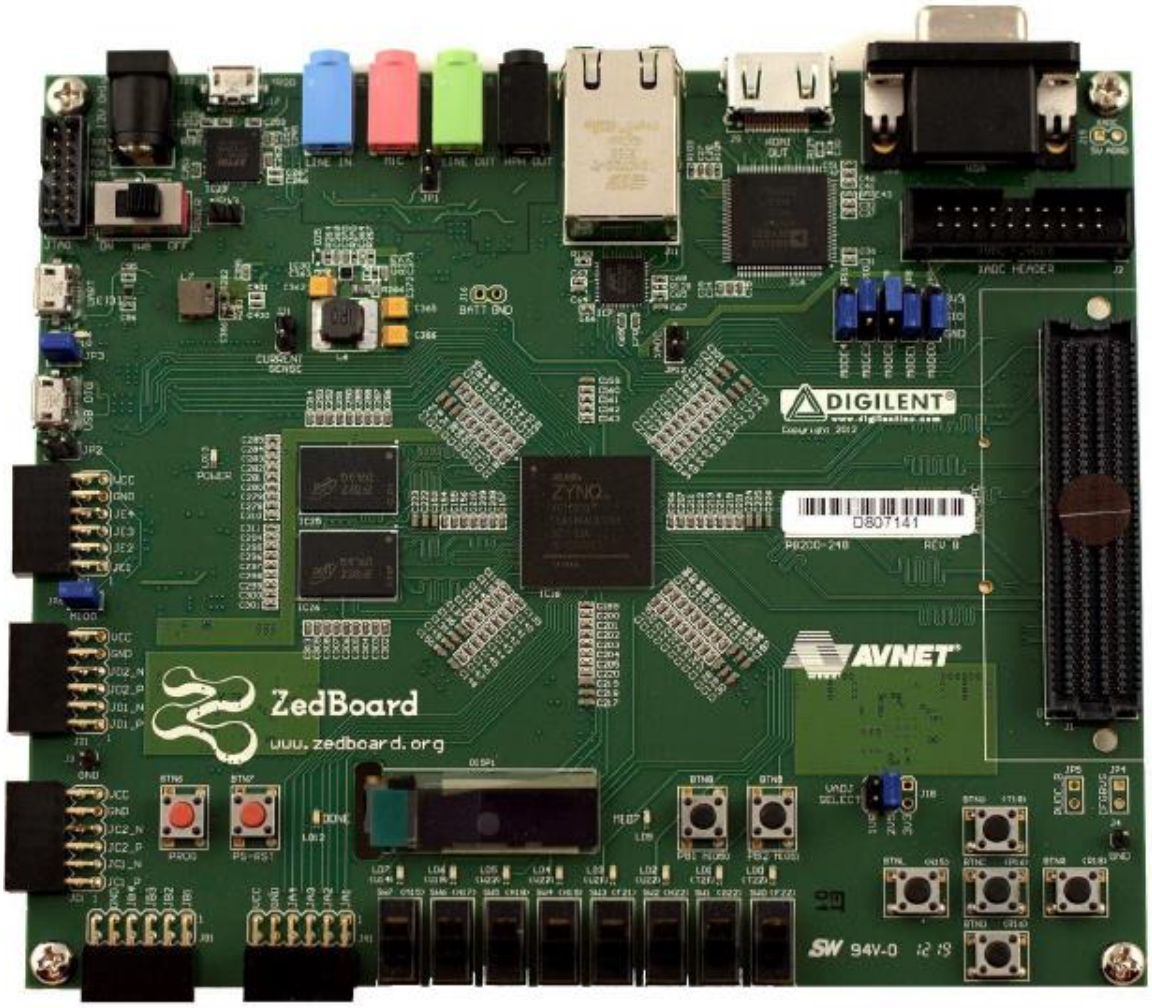

Figure 5.1. ZedBoard Hardware [60]

period is also defined for 10 ns. Figure 5.2 displays the System Generator block and its defined parameters. Once programming is complete, the System Generator block allows one to generate code for the FPGA. Once the current is sampled, the phase currents can be converted into the rotating reference frame. Figure 5.3 and Figure 5.4 show the System Generator code for current sampling and the hardware interface to the ZedBoard's PMOD connections. The Xilinx Gateway In blocks are an interface to FPGA signals and System Generator code. Clarke and Park transformations are performed with the sampled phase currents and the estimated electrical angle of the IPMSM. Figure 5.5 and Figure 5.6 show the transformations within the System Generator environment. I_d and I_q are then passed into a PI controller to obtain a voltage reference used for SVPWM FOC. Inputs into the PI controller include a reset function, the current error term, PI gains, a system trigger that defines the rate at which data between blocks are updated, and a time value used for integration. The variable $SysTrigger$ enables registers to pass new data at a specified rate. Data is still processed at the 100 MHz FPGA clock rate, but now registers can be enabled at a different rate compared to the FPGA clock rate. This is needed for the proper implementation of the integration term in the PI controller. Figure 5.7 shows the PI controller subsystem, and Figure 5.8 displays the System Generator code to generate a sinusoidal signal injected onto the $d-$ axis.

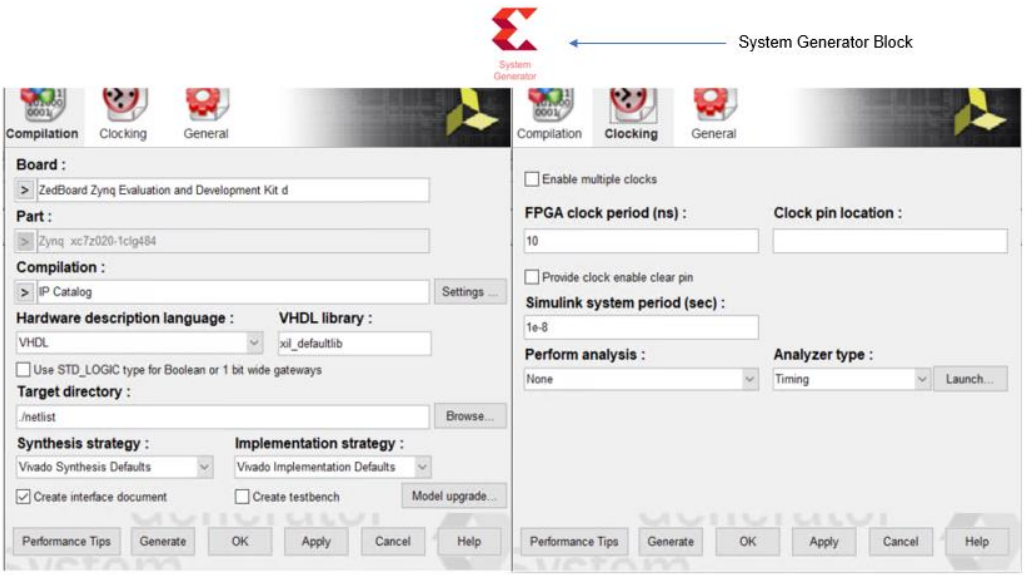

Figure 5.2. System Generator Block Definition

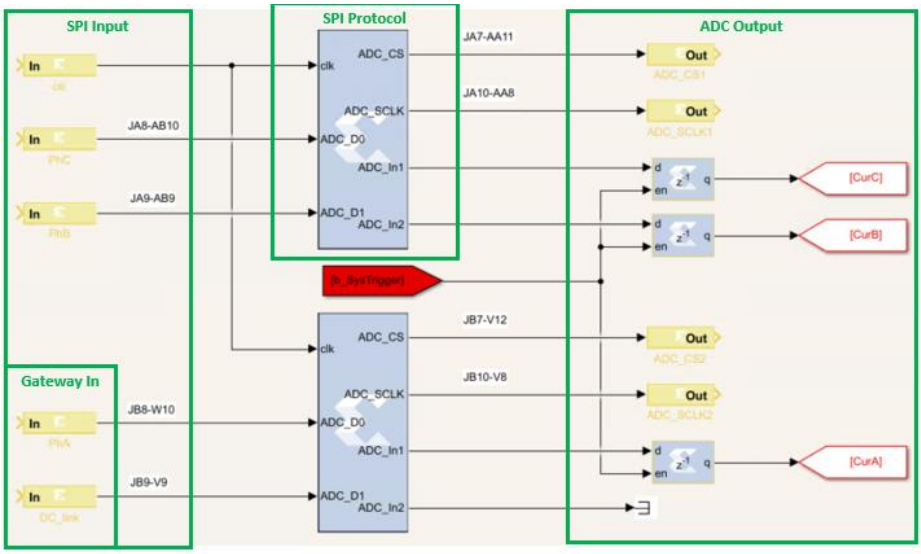

Figure 5.3. System Generator Current Sampling

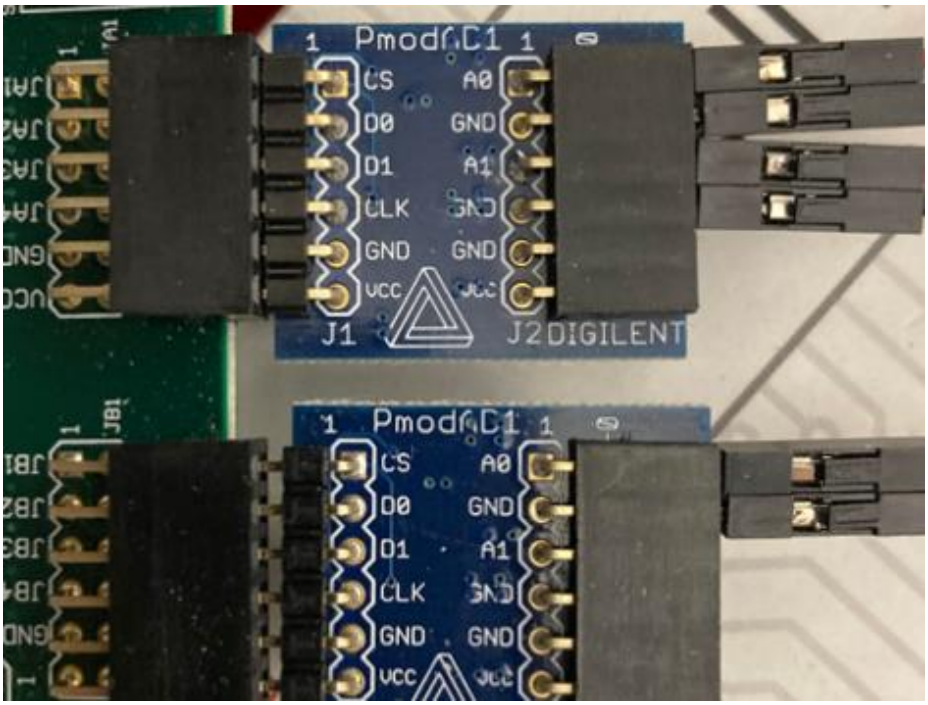

Figure 5.4. Current Sampling PMOD ADC Connection

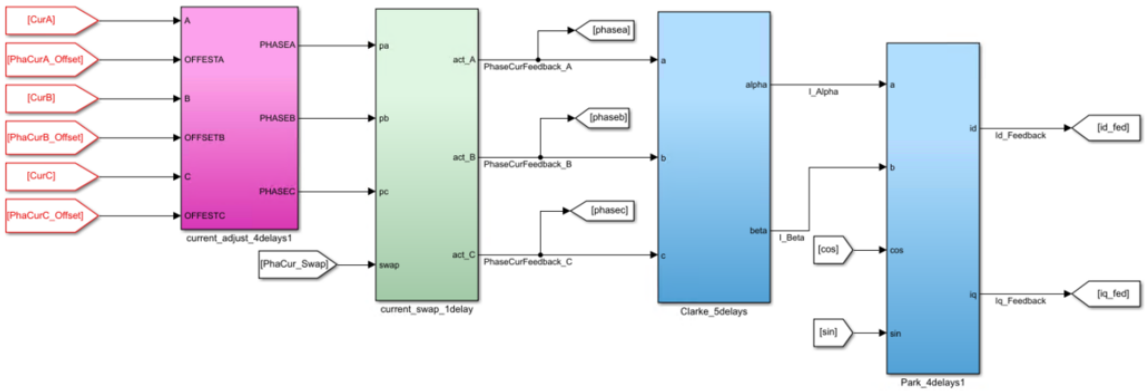

Figure 5.5. Current Clarke and Park Transformations

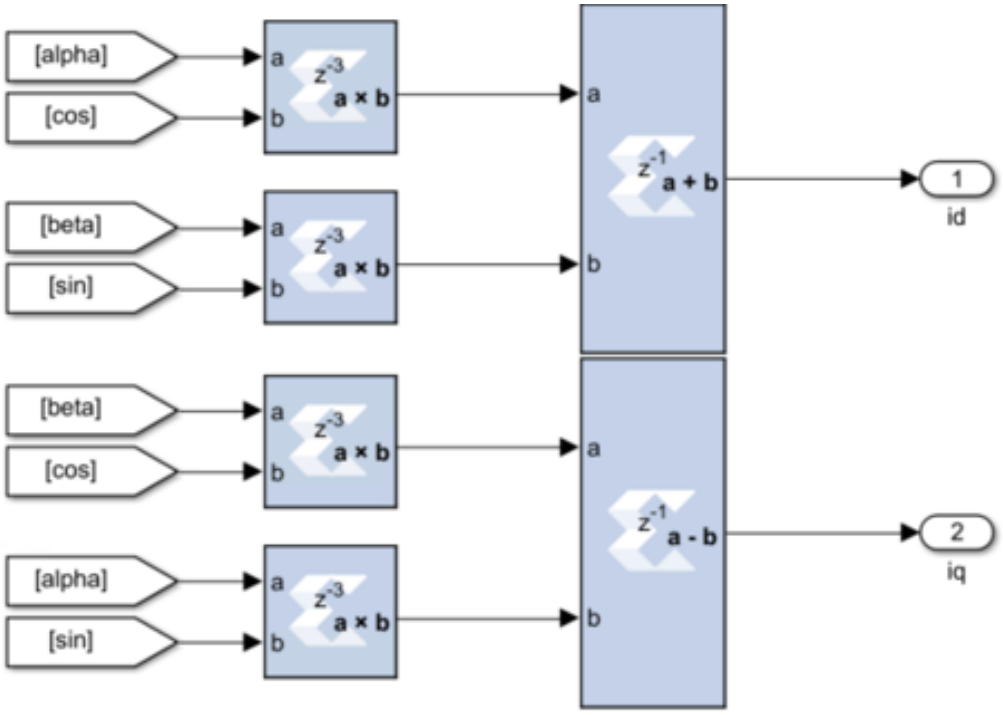

Figure 5.6. System Generator Park Transformation

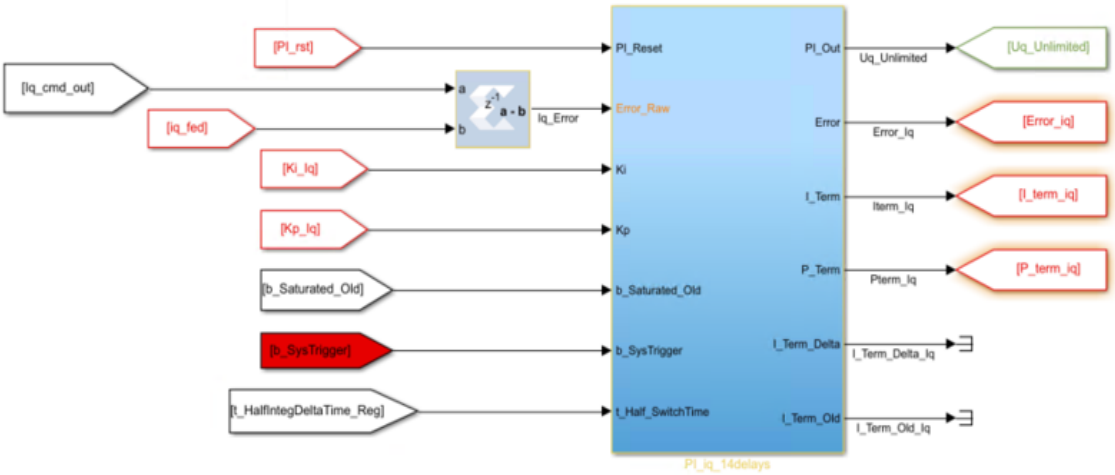

Figure 5.7. Current PI Controller

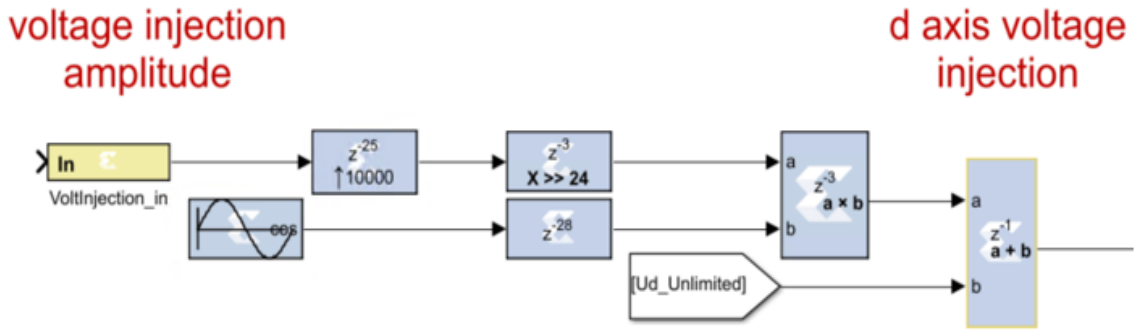

Figure 5.8. High Frequency Sinusoidal Voltage Injection

As the rotating reference frame currents are converted into voltage values, HFI can now be implemented with a sinusoidal voltage superimposed onto the $d-$ axis. Figure 5.8 demonstrates this voltage injection. For square-wave injection, the cosine Xilinx block is removed, and the injection voltage only changes between the positive and negative voltage injection amplitude.

HFI Observer

Parallel processing resources for an FPGA allow the sensorless position estimation to be made possible once the current is sampled, independent of other calculations that must be completed. Figure 5.9 displays the first stage of the HFI observer, showing the bandpass filter, Clarke and Park transformations, and the sinusoidal signal ($\sin 2\pi F_{inj}t$) that is multiplied by I_{qh}. The Park transformation utilizes the estimated position. Figure 5.10 displays the low-pass filter and the saliency term, I_{qh}. The bandpass filter can be converted from a second-order transfer function to a difference equation that is dependent on the sampling rate and center frequency. Equation (5.1) demonstrates the difference equation used to create a bandpass filter in the mCode Xilinx System Generator block. Coefficients are determined based on the injection frequency and sampling rate of the filter.

$$Y[n] = a_1 Y[n-1] - a_2 Y[n-2] + b_1 X[n-1] - b_2 X[n-2] \qquad (5.1)$$

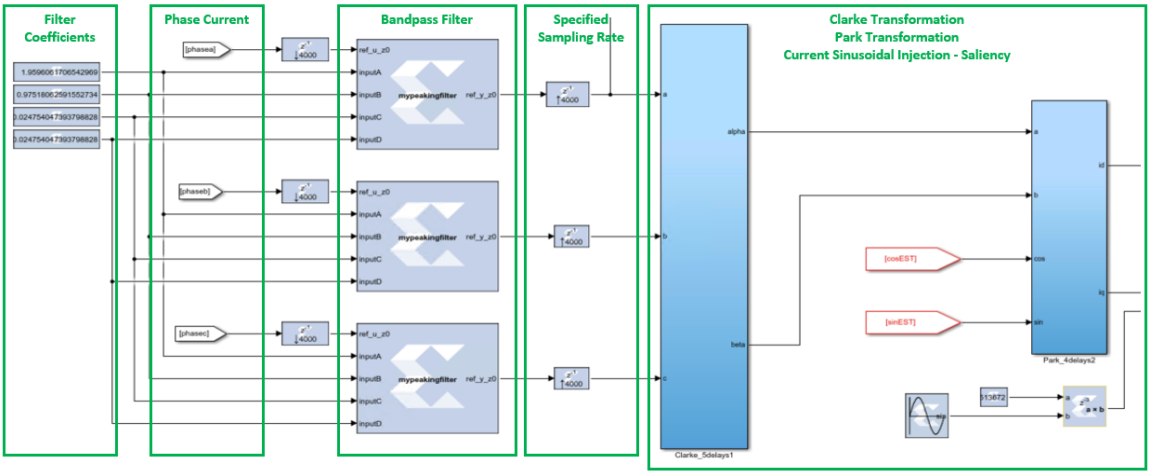

Figure 5.9. HFI Observer Bandpass Filter and Transformations

With an injection frequency of 500 Hz and a sampling rate set to 20 kHz, the coefficients can be calculated; however, with different injection frequencies and sampling rates, the filter coefficients will vary. The low-pass filter difference equation can be represented by Equation (5.2) and implemented in the mCode Xilinx System Generator block. The low-pass filter coefficients are dependent on the cutoff frequency and the sampling rate. With a cutoff frequency of 150 Hz, a set damping factor of 0.707, and a sampling rate of 20 kHz, the coefficients can then be calculated.

$$Y[n] = a_1 Y[n-1] - a_2 Y[n-2] + b_1 X[n-1] + b_2 X[n-2] \qquad (5.2)$$

The estimated speed and electrical position are sent to Xilinx Gateway Out blocks to allow for real-time monitoring and data visualization during experimental testing, which will be discussed in the Vivado Build section. Once speed and position estimations are made, comparisons can be made with measured speed and position information, both calculated from the mechanical resolver attached to the IPMSM. Figure 5.11 demonstrates the speed tracking PI controller and an integration term to obtain the rotor position from the speed estimation. The speed estimation is in units of radians per second, but then converted to revolutions per minute as the speed reference is in units of revolutions per minute.

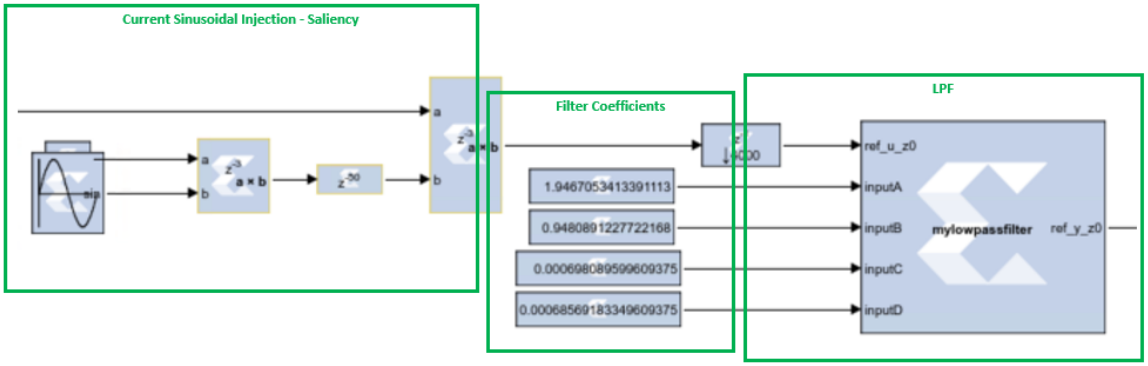

Figure 5.10. Low-Pass Filter with Saliency Current

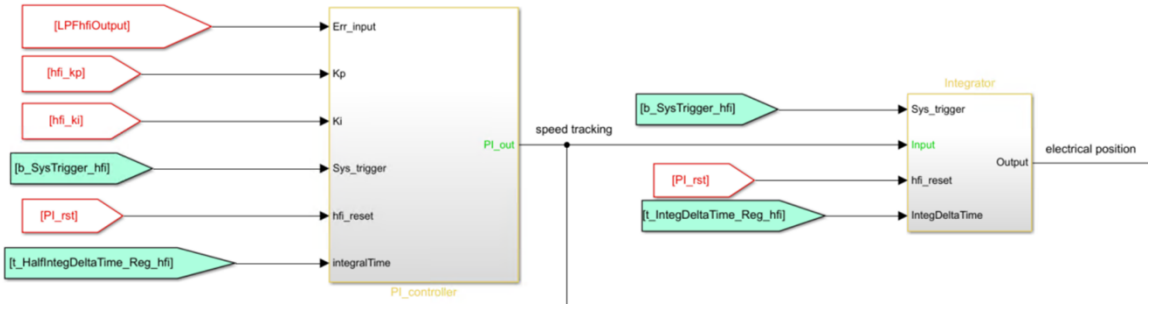

Figure 5.11. Speed Tracking PI Controller and Position Integrator

Angle Error Calculation

To validate the sensorless control algorithm, a resolver is also utilized to generate a position and speed measurement. Figure 5.12 shows the resolver and phase current connections to the IPMSM. The phase current connections go directly to the three-phase SiC inverter. The main connections from the resolver include the Sine, Sine Low, Cosine, Cosine Low, Excitation, and Excitation Low signals to obtain the rotor position information. These signals are operating at 10 kHz, with a constant amplitude for the Excitation and Excitation Low signals while the Sine and Cosine signals vary in amplitude as the rotor spins. The resolver connections from the motor are then sent to the EVAL-AD2S1210SDZ RDC board, shown in Figure 5.13, to convert the resolver signals into a digital value for the ZedBoard. The RDC board then sends a 12-bit digital signal to the ZedBoard PMOD connectors. Within System Generator, this digital position signal is mapped to an electrical angle for the IPMSM. Figure 5.14 demonstrates the System Generator calculation to measure the electrical position of the IPMSM rotor. The measured electrical position is then compared to the estimated electrical position produced from the HFI observer, depicted in Figure 5.15.

Vivado Build

System Generator for DSP offers a model-based programming environment for Xilinx Zynq platforms. Upon model-based coding completion, VHDL code can be generated from the System Generator block, which was previously shown in Figure 5.2. A Vivado project is created from the IP Integrator.

Figure 5.12. IPMSM Resolver Connection

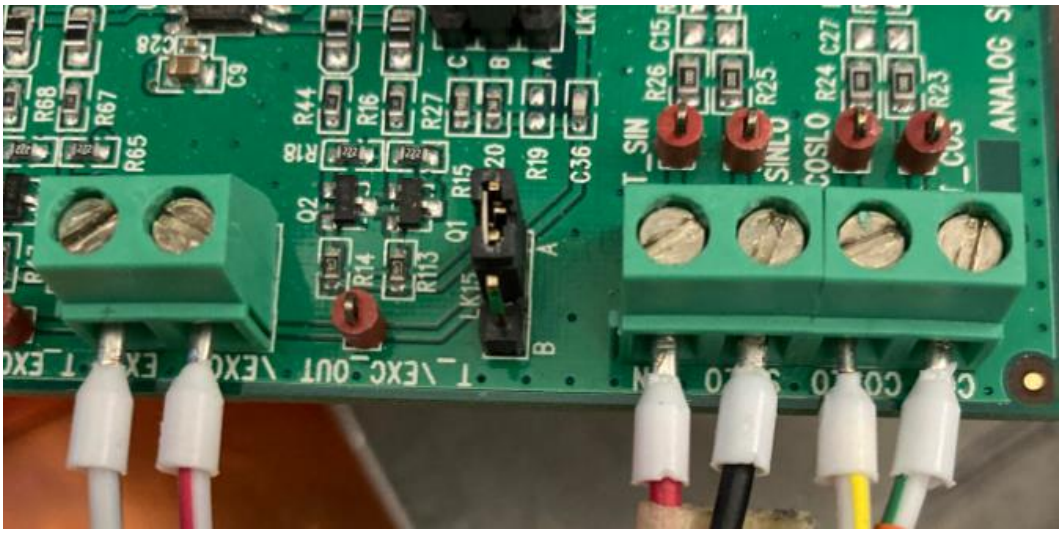

Figure 5.13. Resolver Connections to RDC Board

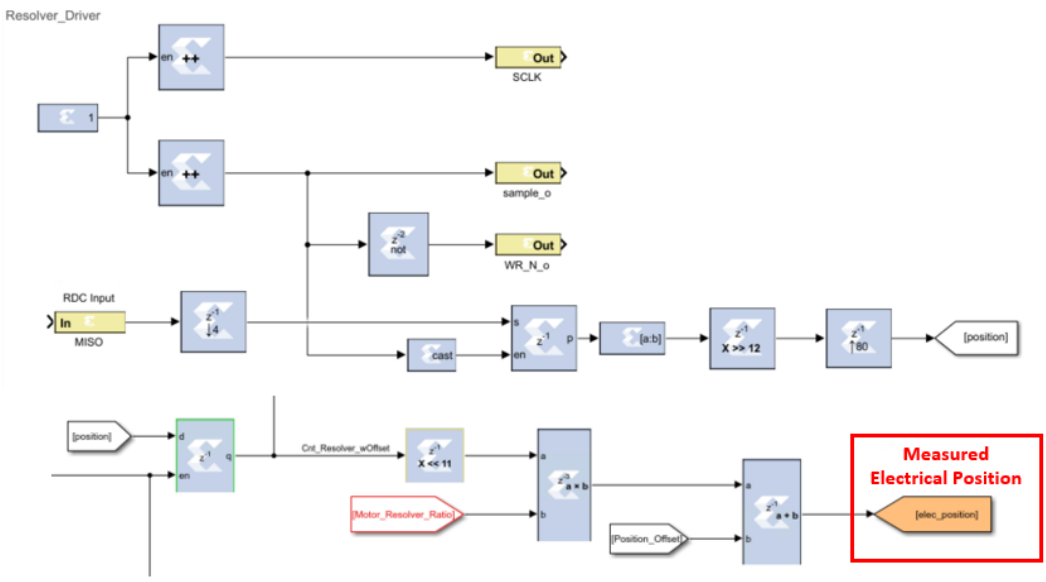

Figure 5.14. System Generator Electrical Position Measurement

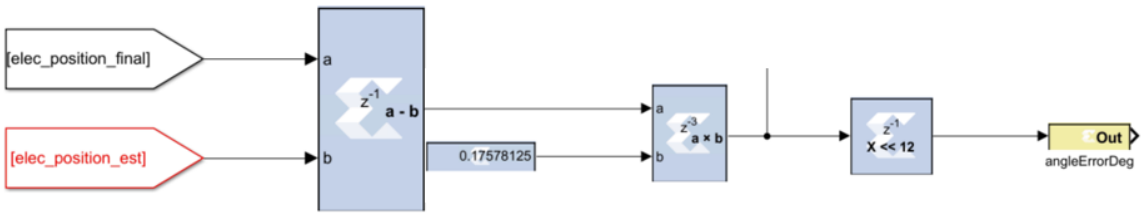

Figure 5.15. Angle Error Calculation

The first step in creating code for the ZedBoard involves opening the IP Block Design, as shown in Figure 5.16, which is generated from the System Generator for DSP model. This IP block design has several components, with the IP ZYNQ7 Processing System used to provide logic connections between the processing system and programmable logic units. Additionally, the ZYNQ7 Processing System integrates custom IP developed in the System Generator for DSP environment. A bitstream is then generated from the IP Block Design to program the FPGA. The resulting bitstream provides information on the FPGA resource utilization. An example build for the rotating sinusoidal injection sensorless control method can be seen in Figure 5.17. Included in the Zynq 7000 SoC Zedboard are DSP slices as well as Look-Up Tables (LUT), Flip Flops (FF), and Input/Output (IO) ports. For the Zedboard, 220 DSP slices are available and 207 DSP slices are utilized in the project. Additionally, 24,054 LUT blocks are utilized out of the available 53,200 while 17 IO blocks out of the available 200 are utilized. 106,400 FF blocks are available, and 26,759 are used. After programming the ZedBoard, experimental testing can be conducted. Within the System Generator model, there are Xilinx Gateway Out blocks that can utilize the AXI4-Lite interface. Xilinx Gateway Out blocks are mapped to registers within the AXI4-Lite interface that allow data to be visualized in Simulink; this is made possible through the ethernet connection between the ZedBoard and host PC.

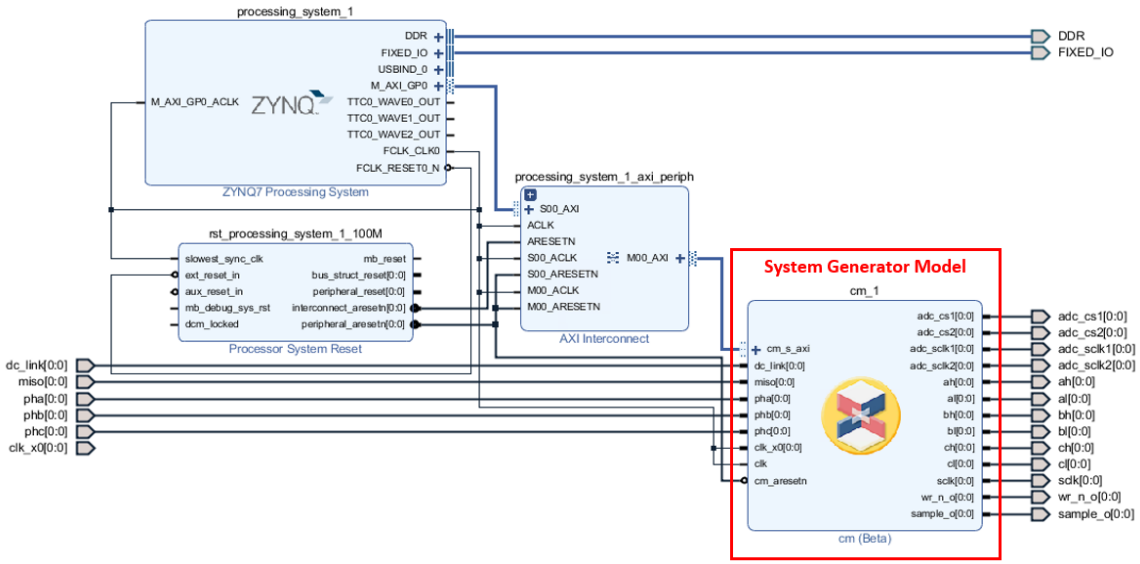

Figure 5.16. IP Block Design from System Generator

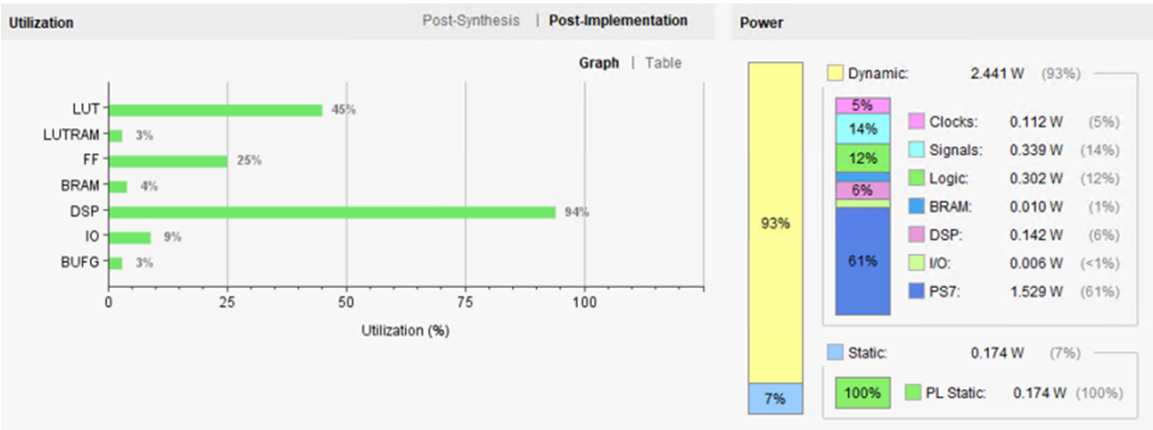

Figure 5.17. FPGA Resource Utilization on ZedBoard

Gateway Out blocks are shown in Figure 5.18 from the System Generator model, showing the phase current, speed estimation, and SVPWM reference waveform sent to registers for the AXI4-Lite interface. An interface model in Simulink can be seen in Figure 5.19, with the corresponding signals from Figure 5.18 to visualize during experimental testing. These signals are connected to a Simulink scope for real-time monitoring. Additionally, Xilinx Gateway In blocks can be used with the AXI4-Lite Interface to control inputs into the System Generator model. Gateway In blocks connected to the AXI4-Lite interface can be seen in Figure 5.20, commanding the speed and current references for the IPMSM. For example, speed and current commands can be inputs the user defines while testing. In Figure 5.21, a Simulink model utilizing the AXI4-Lite interface shows the speed; current; and switching frequency commands that are sent to the FPGA. During experimental testing, these values can be modified, and the FPGA will respond accordingly. To summarize the FPGA development process, model-based coding begins in the Simulink System Generator for DSP environment. An IP Block Design is generated from System Generator and opened in Vivado. A bitstream is then generated from the IP Block Design to program the ZedBoard. Once the ZedBoard is programmed in Vivado, a Simulink interface model is opened to begin experimental testing. Data is transferred between the ZedBoard's ethernet port to the host PC – with the Simulink interface model commanding FPGA outputs and visualizing FPGA inputs.

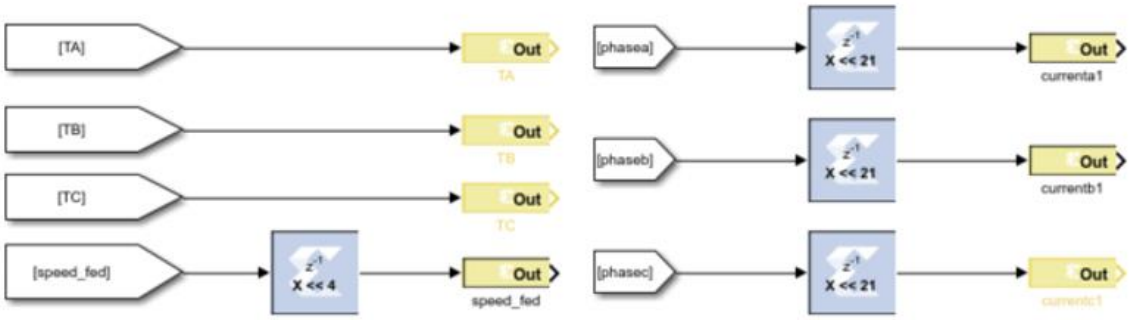

Figure 5.18. Gateway Out Signals

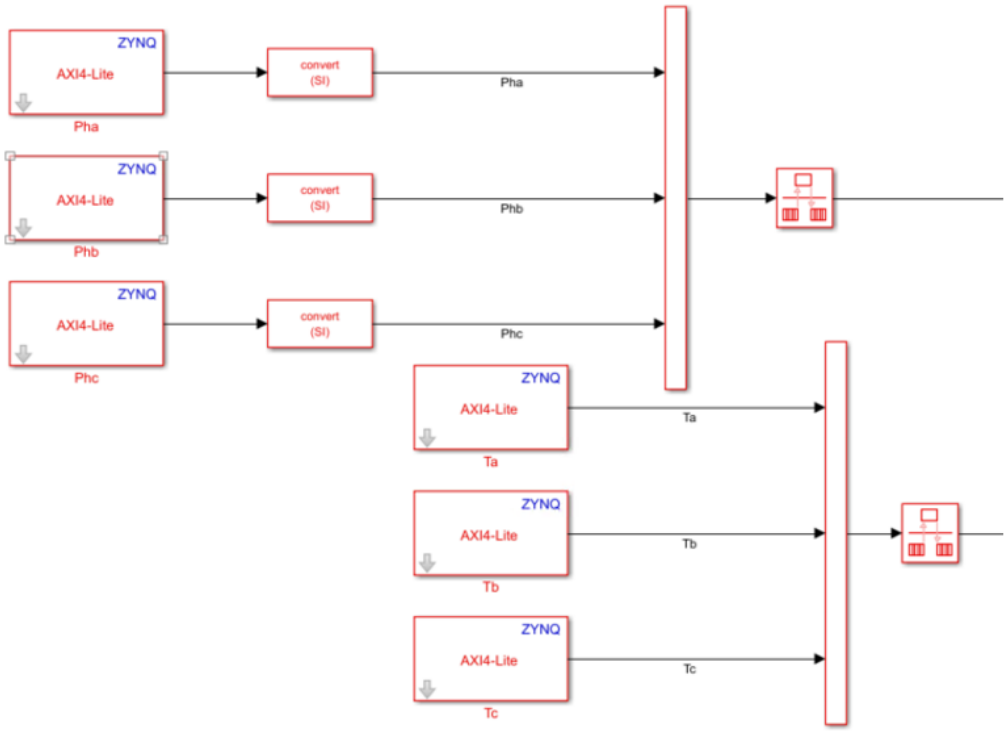

Figure 5.19. AXI4-Lite Interface from Gateway Out Blocks

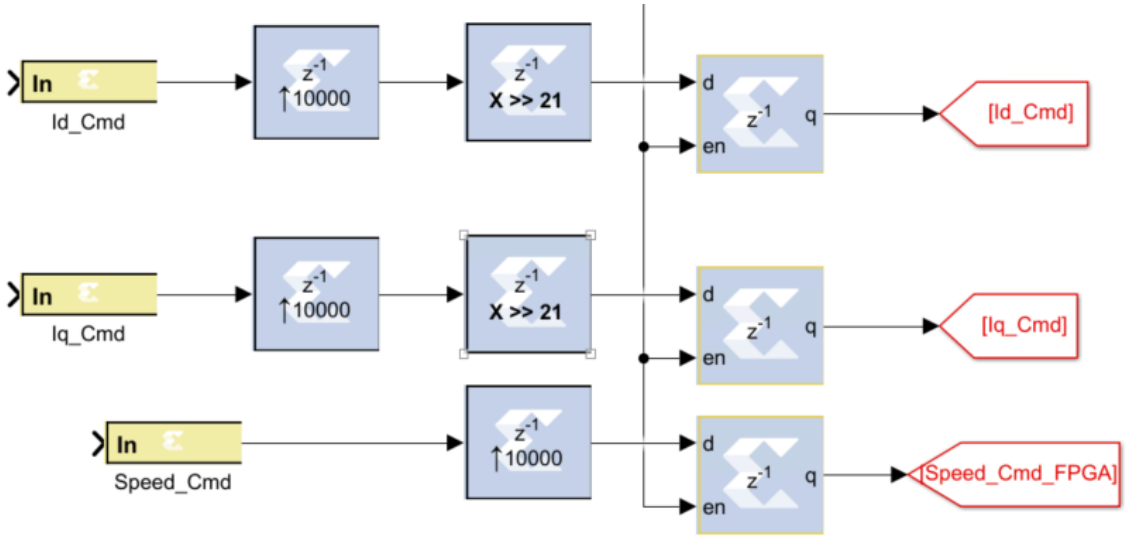

Figure 5.20. AXI4-Lite Interface with Gateway In Blocks

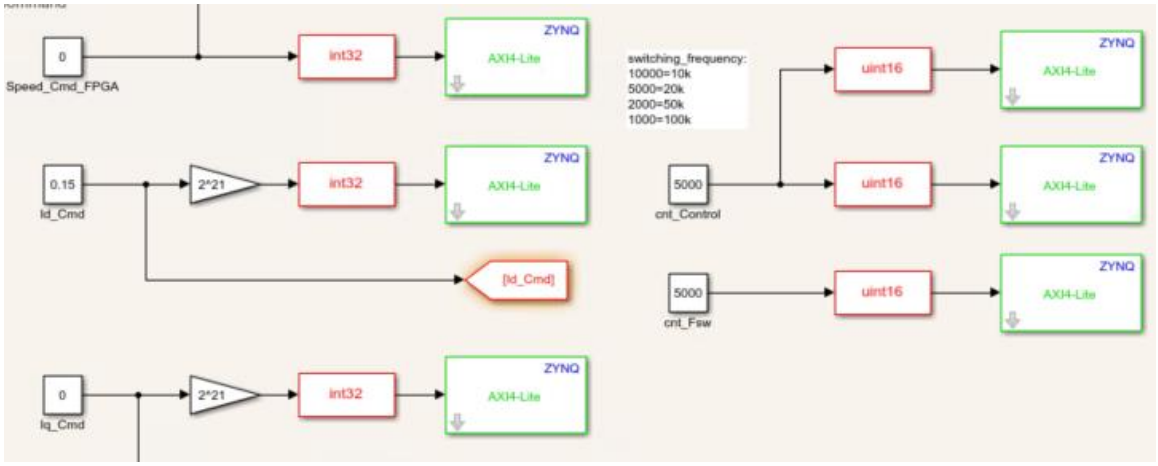

Figure 5.21. AXI4-Lite Interface in Simulink as Inputs

Experimental Results

A SiC three-phase inverter has been designed to facilitate the HFI sensorless control method. Figure 5.22 demonstrates the PCB design for the inverter – containing connectors for the DC voltage supply and three-phase current, DC link capacitors, current sensors, gate driver circuits, and connectors to interface with the ZedBoard. Figure 5.23 displays the bottom side of the PCB where the SiC MOSFETs are placed, having a direct placement to the inverter heatsink to improve thermal dissipation. Figure 5.24 displays the full experimental setup. Present in the experimental setup is the host PC for visualizing FPGA calculations and measurements and providing motor commands. An oscilloscope is used to measure the SiC MOSFETs gate drive signals and the motor winding current. The SiC inverter, ZedBoard, and RDC board are displayed with their connections to one another. Last, the IPMSM under testing is shown. The parameters for the IPMSM are defined in Table 5.1, showing the rated voltage, current, and speed. Additionally, the saliency is shown with the rotating reference frame inductances.

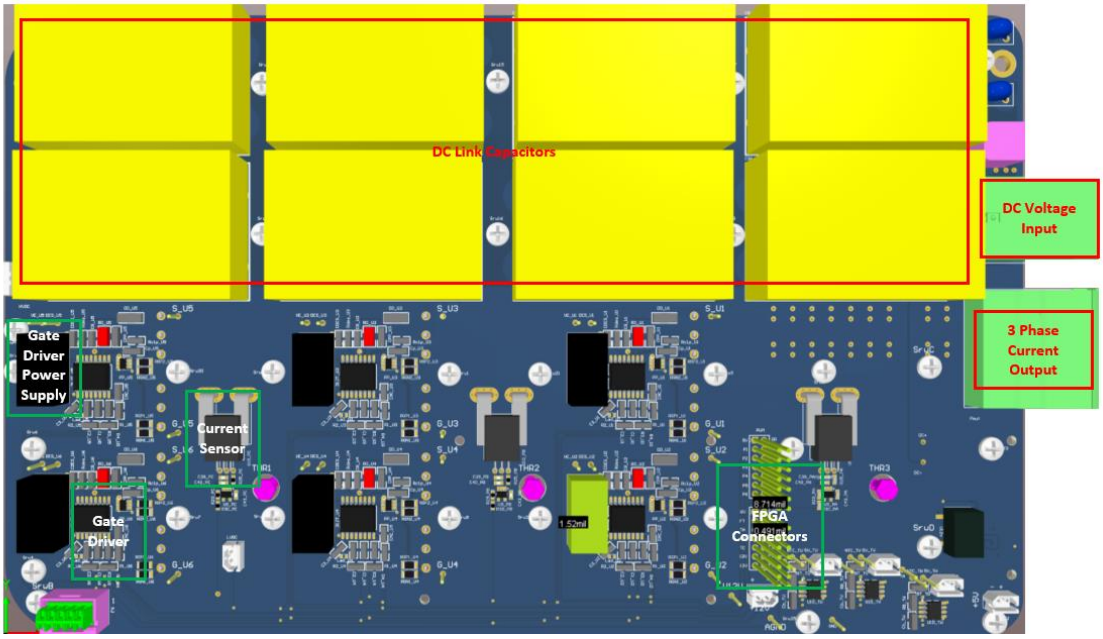

Figure 5.22. Altium Designer SiC Inverter

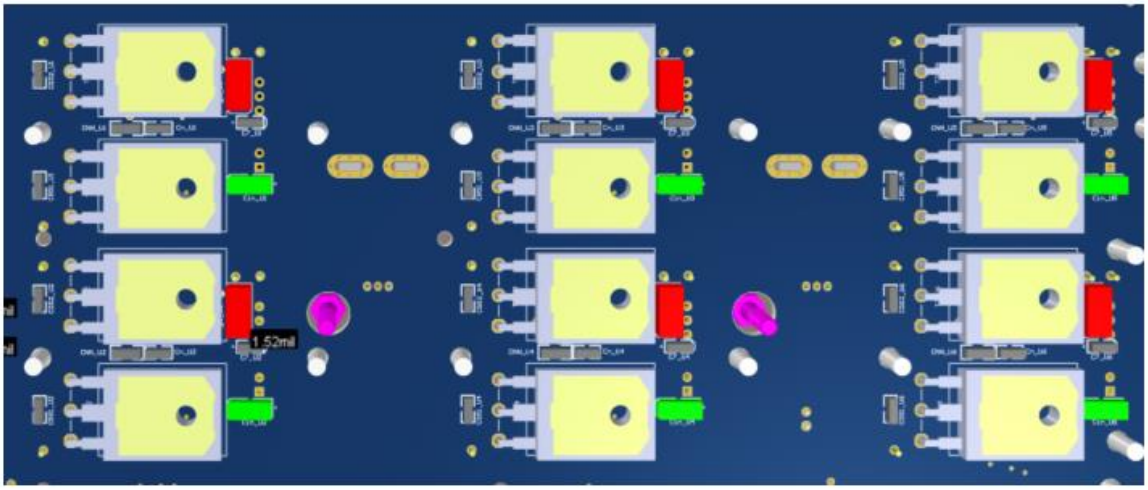

Figure 5.23. SiC MOSFETs

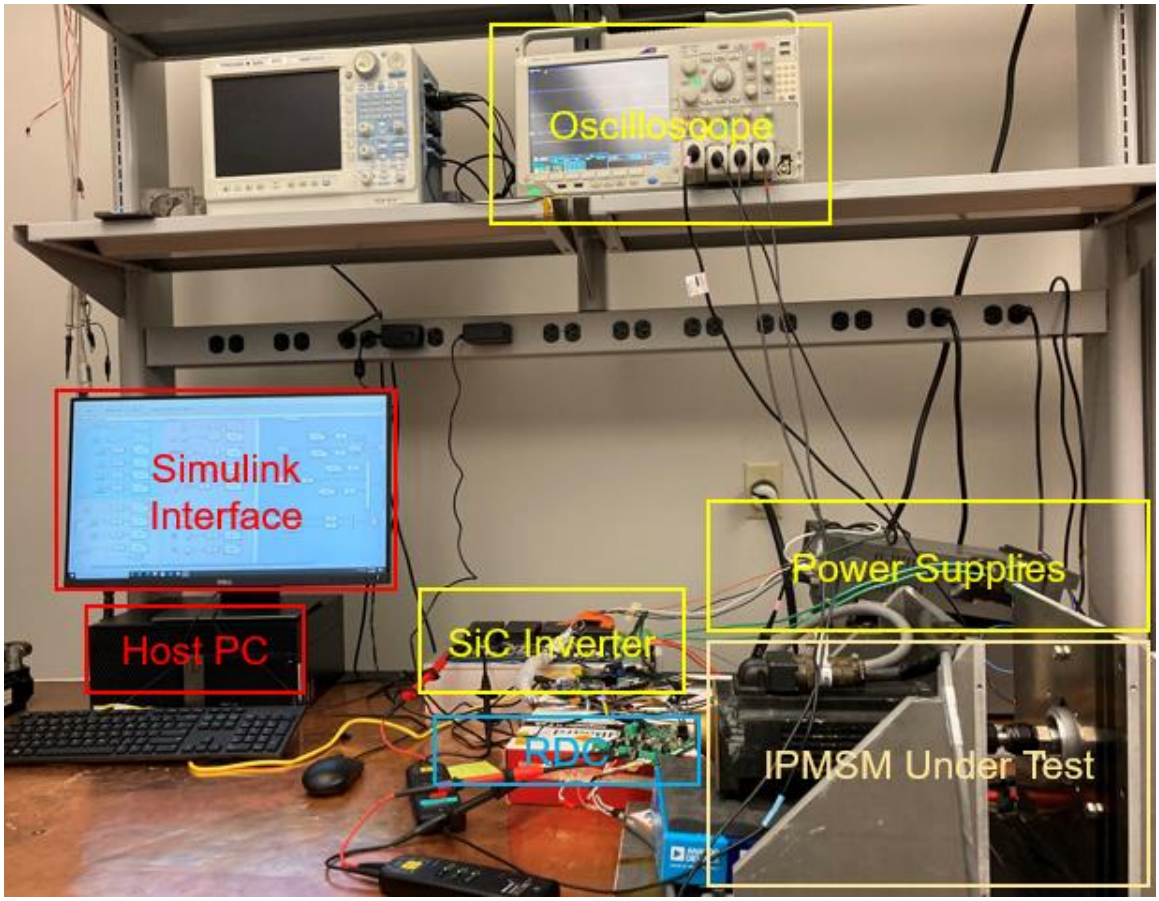

Figure 5.24. Experimental Setup

Table 5.1. IPMSM Parameters

Parameter	Value	Unit
Rated Voltage	230	V
Continuous Current	3.0	A
Peak Current	9.6	A
Rated Power	6.9	kW
Max Speed	3800	RPM
Rated Torque	2.44	Nm
Peak Torque	7.38	Nm
L_d Inductance	12	mH
L_q Inductance	34	mH
Stator Resistance	6.98	Ω

Audible Noise Analysis

The following test results demonstrate the audible noise presence from the sensorless control algorithm as the injection frequency and switching frequency are manipulated. The rotational speed of the motor is 150 RPM, and the DC bus voltage is set to 150 Volts. Figure 5.25 and Figure 5.26 display the audible noise present in the motor drive system for the sinusoidal injection sensorless control method at 500 Hz; Figure 5.27 and Figure 5.28 demonstrate the audible noise from square-wave injection. The injection frequency is then increased, with results shown in the following figures for both sinusoidal and square-wave injection. Figure 5.29 and Figure 5.30 show the audible noise results for a 1 kHz sinusoidal injection signal while Figure 5.31 and Figure 5.32 demonstrate a 1 kHz square-wave injection signal. Audible noise results for a 2 kHz sinusoidal injection method can be viewed in Figure 5.33 and Figure 5.34, and square-wave injection results are shown in Figure 5.35 and Figure 5.36. A 4 kHz sinusoidal injection signal was also tested, with audible noise results in Figure 5.37 and Figure 5.38. The audible noise for the sinusoidal injection can be summarized in Figure 5.39, plotting the peak noise for each injection frequency. To better understand the resulting noise from the square-wave injection, the Fourier series can be shown in Equation (5.3).

$$f(t) = \frac{4}{\pi} \sum_{n=1,3,5,\ldots}^{\infty} \frac{1}{n} \cos(n\omega_{inj} t) \tag{5.3}$$

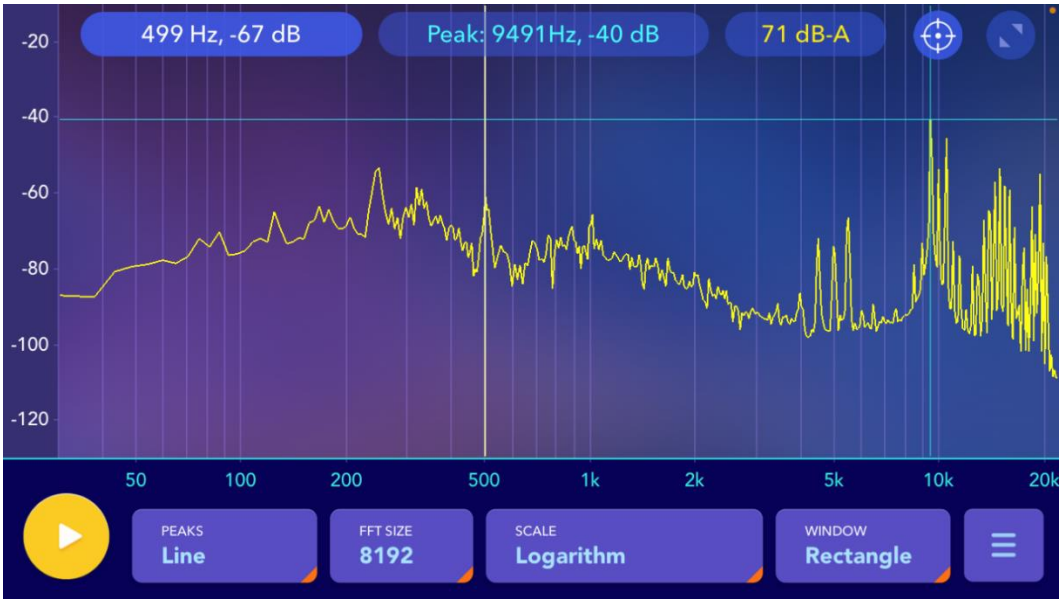

Figure 5.25. 500 Hz Sine Injection and 5 kHz Switching Frequency

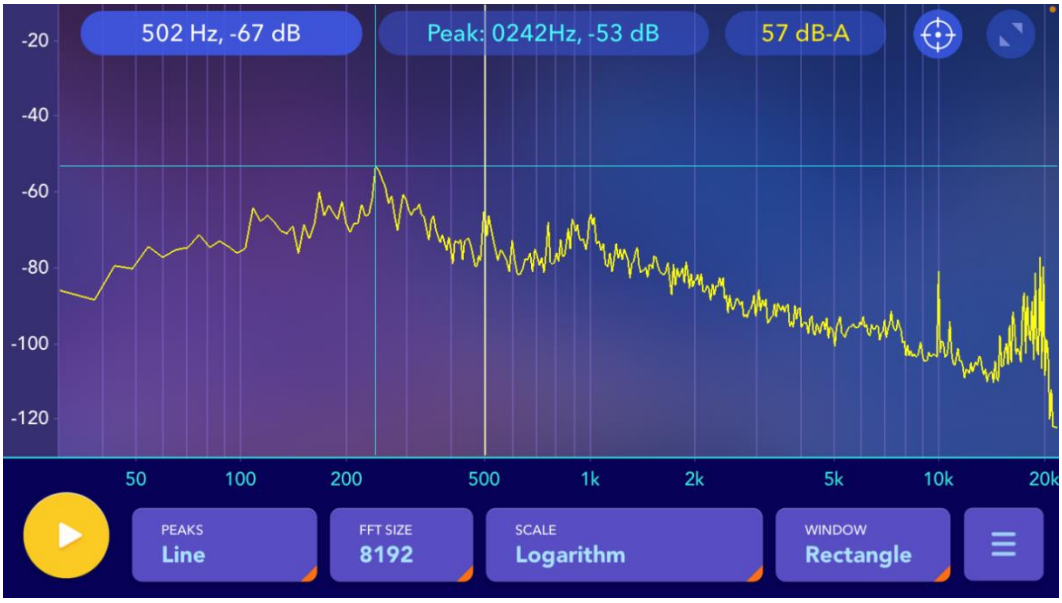

Figure 5.26. 500 Hz Sine Injection and 20 kHz Switching Frequency

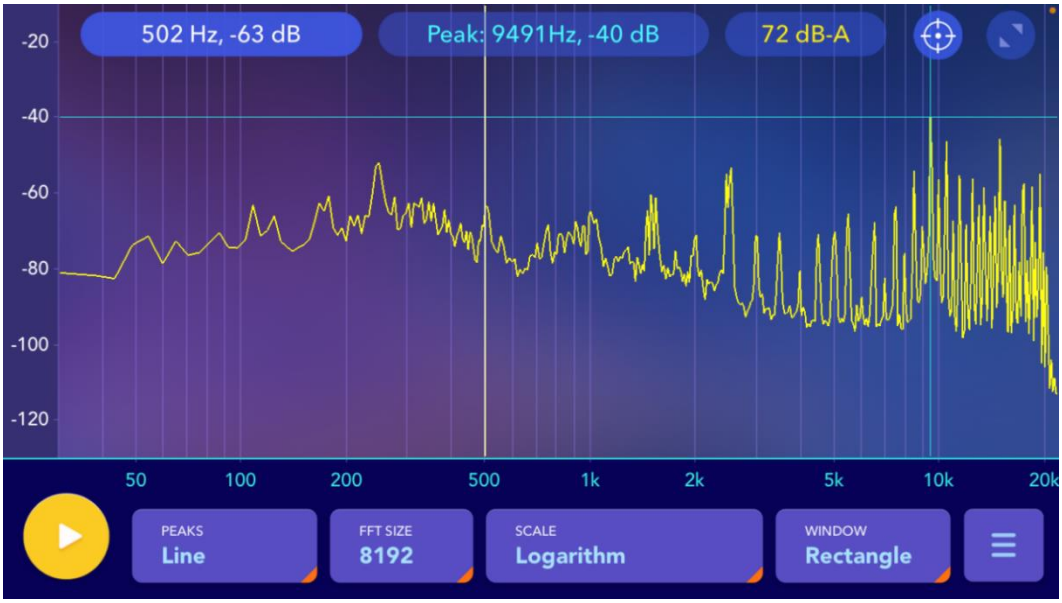

Figure 5.27. 500 Hz Square Injection and 5 kHz Switching Frequency

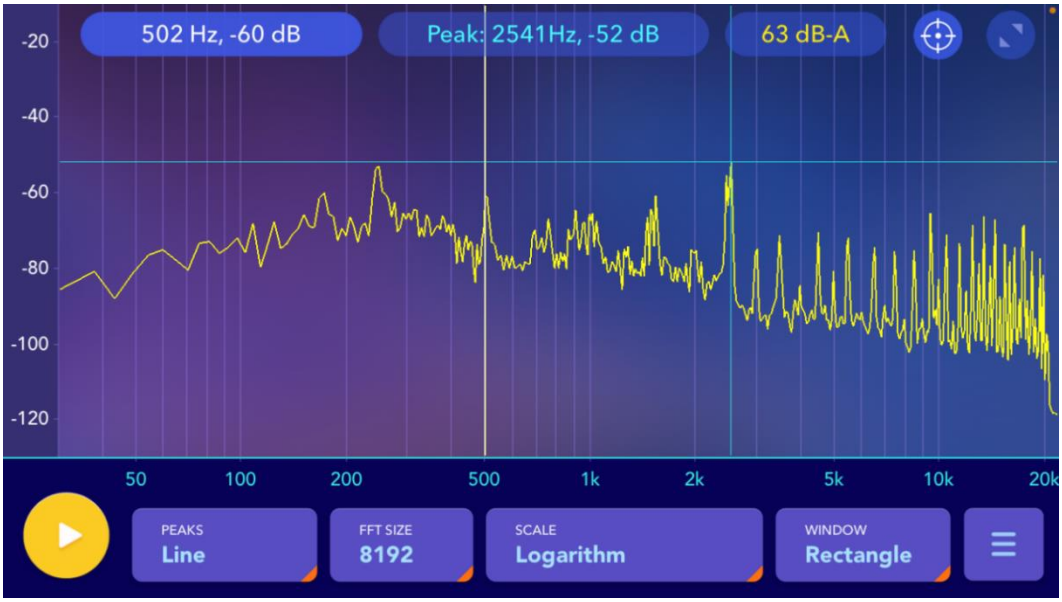

Figure 5.28. 500 Hz Square Injection and 20 kHz Switching Frequency

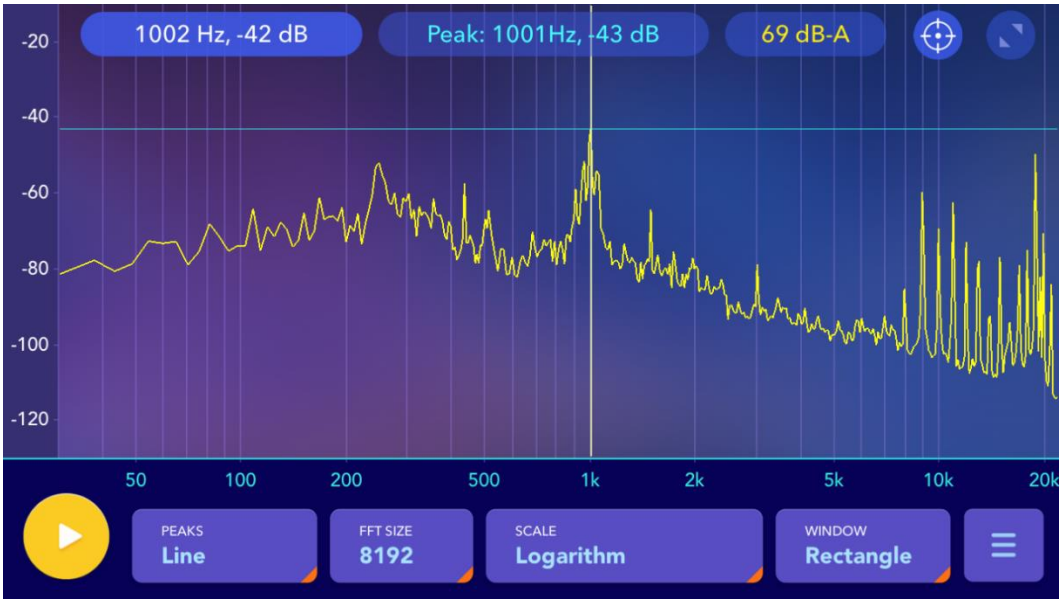

Figure 5.29. 1 kHz Sine Injection and 10 kHz Switching Frequency

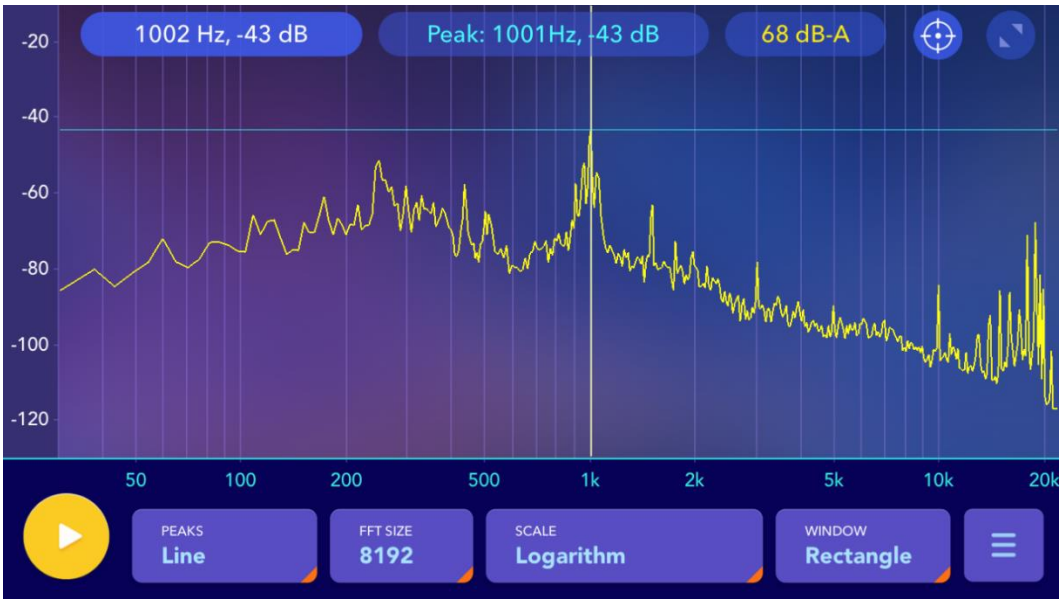

Figure 5.30. 1 kHz Sine Injection and 20 kHz Switching Frequency

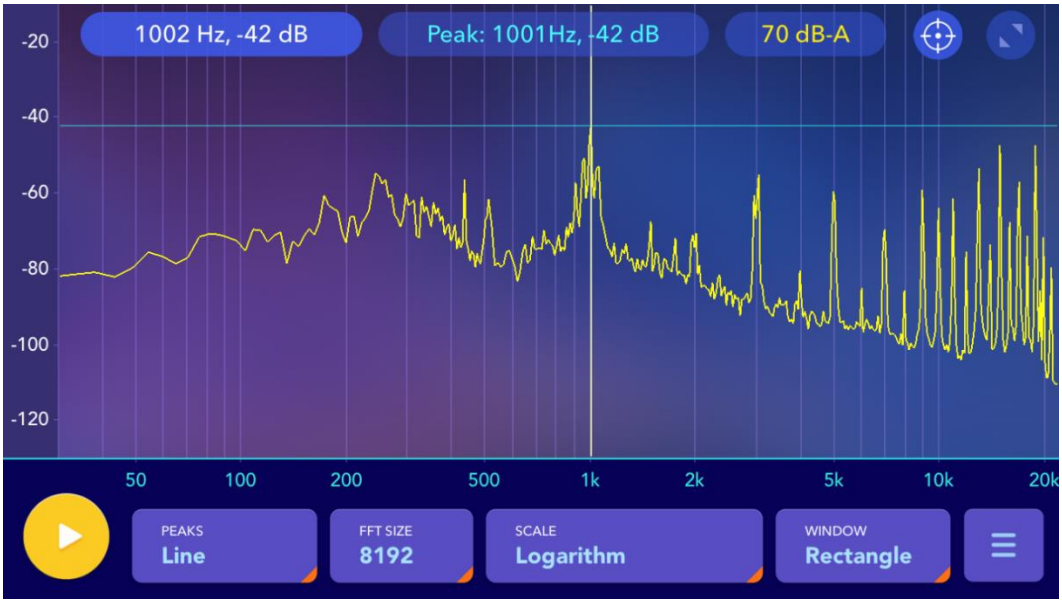

Figure 5.31. 1 kHz Square Injection and 10 kHz Switching Frequency

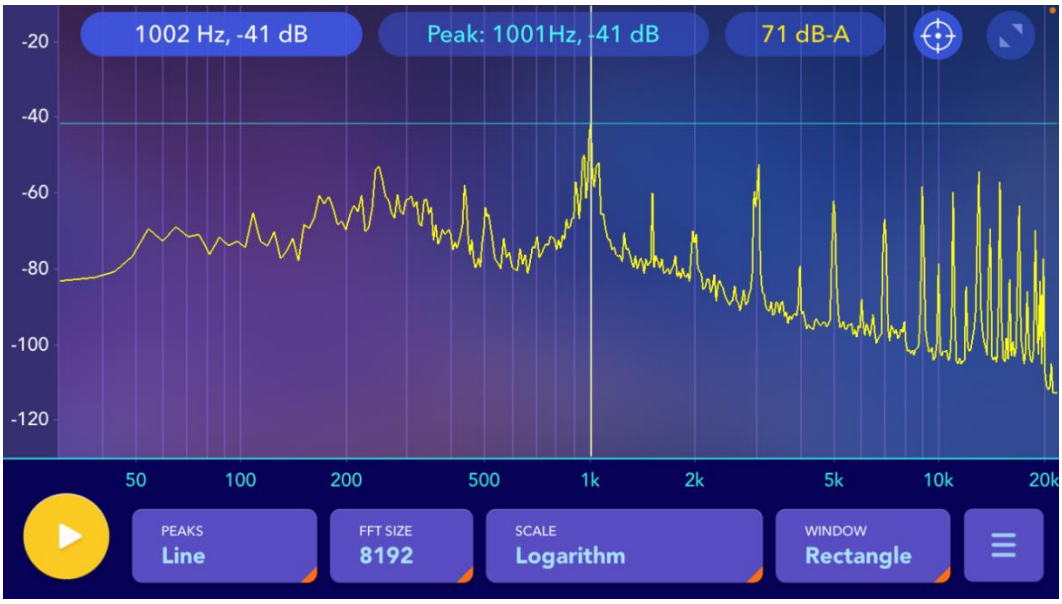

Figure 5.32. 1 kHz Square Injection and 20 kHz Switching Frequency

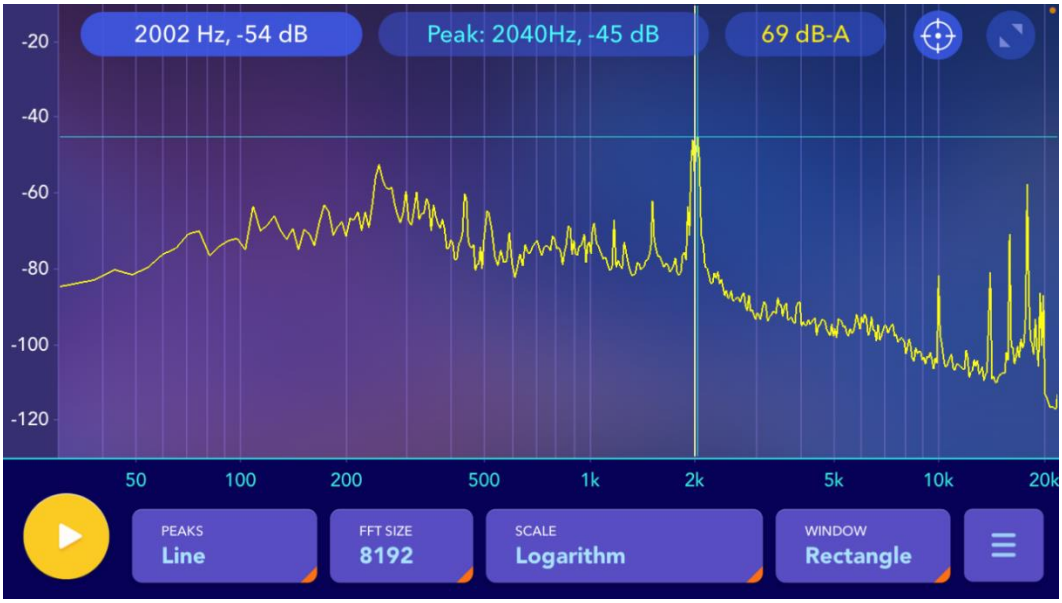

Figure 5.33. 2 kHz Sine Injection and 20 kHz Switching Frequency

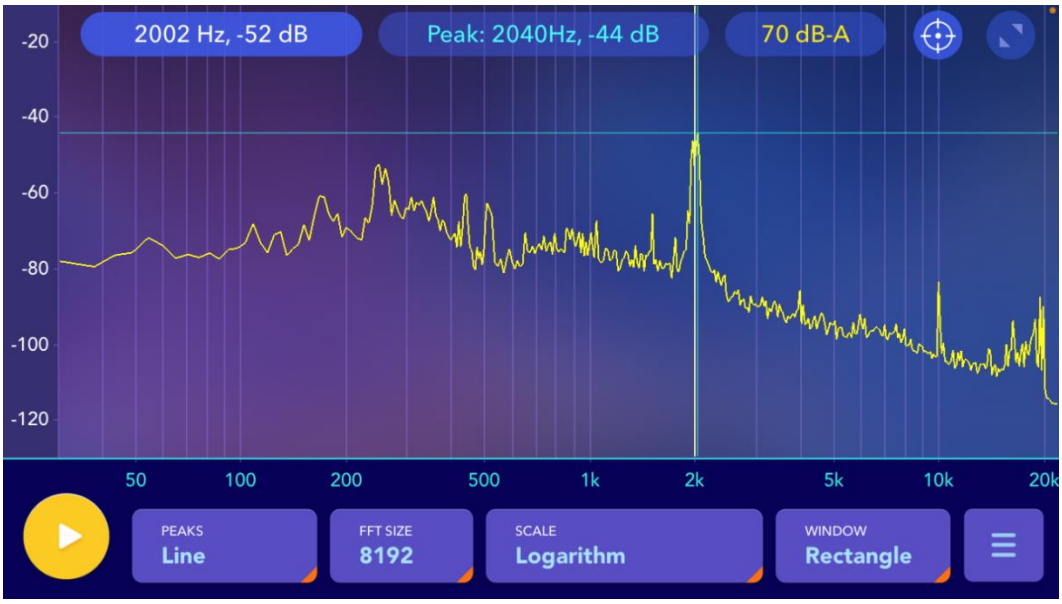

Figure 5.34. 2 kHz Sine Injection and 40 kHz Switching Frequency

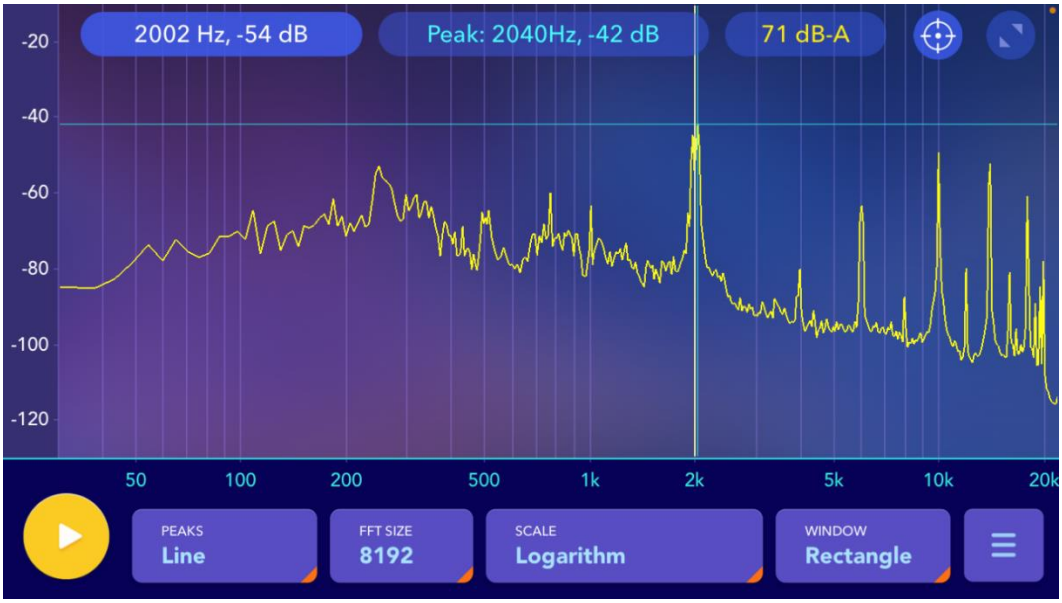

Figure 5.35. 2 kHz Square Injection and 20 kHz Switching Frequency

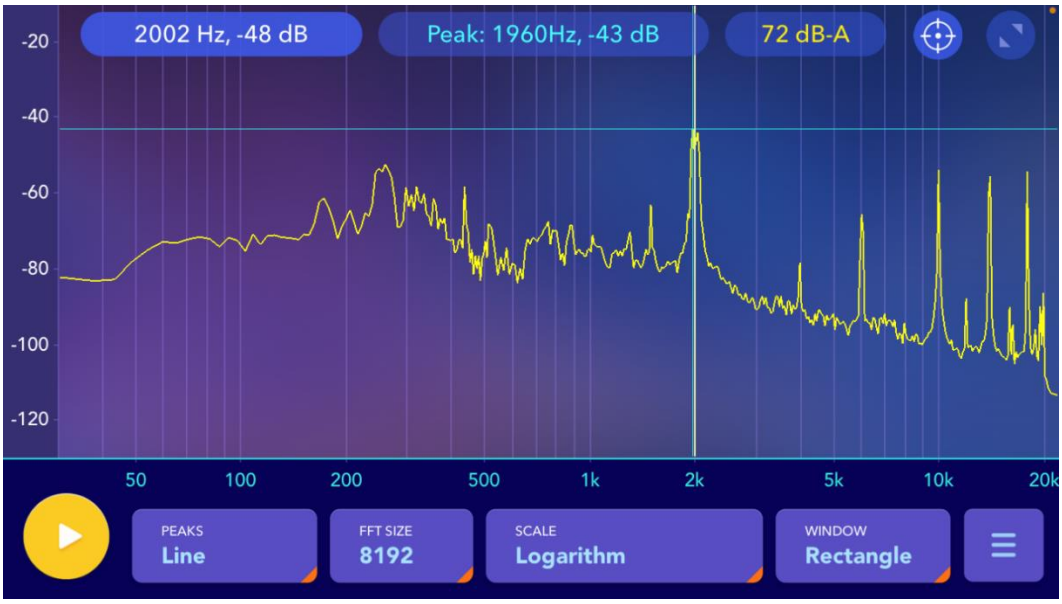

Figure 5.36. 2 kHz Square Injection and 40 kHz Switching Frequency

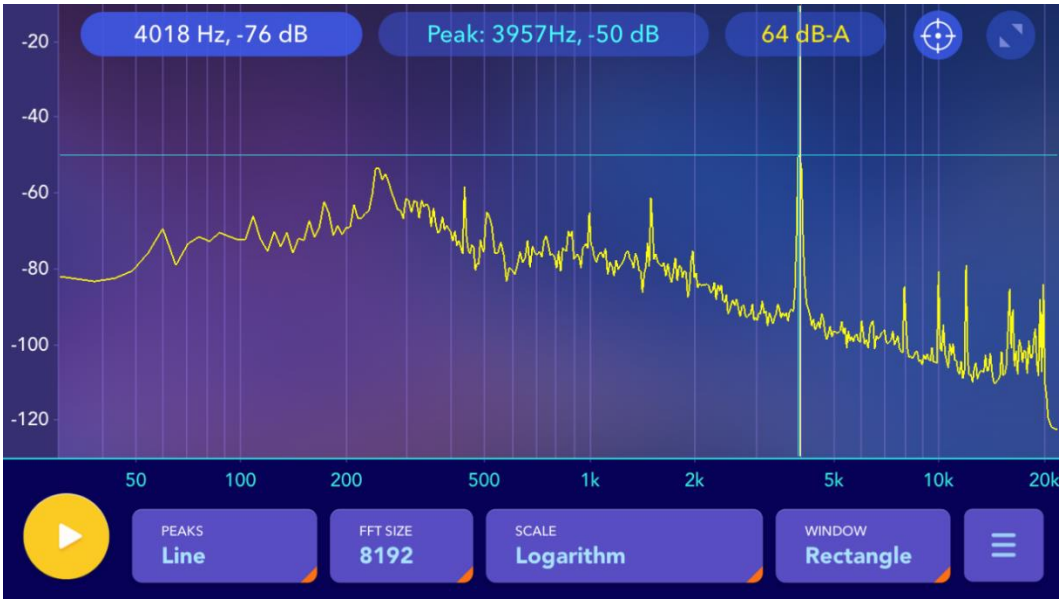

Figure 5.37. 4 kHz Sine Injection and 40 kHz Switching Frequency

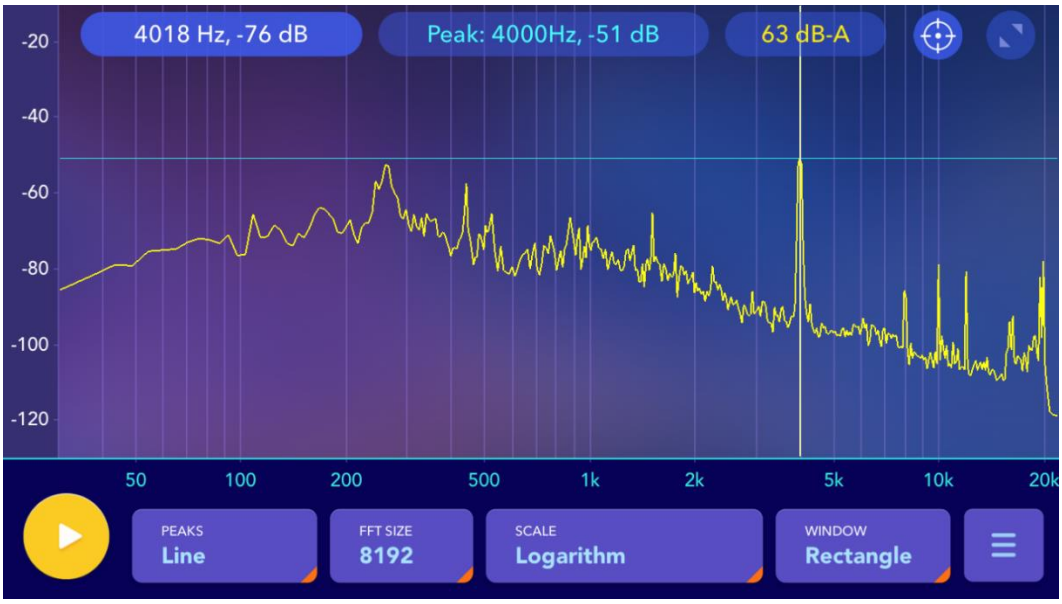

Figure 5.38. 4 kHz Sine Injection and 60 kHz Switching Frequency

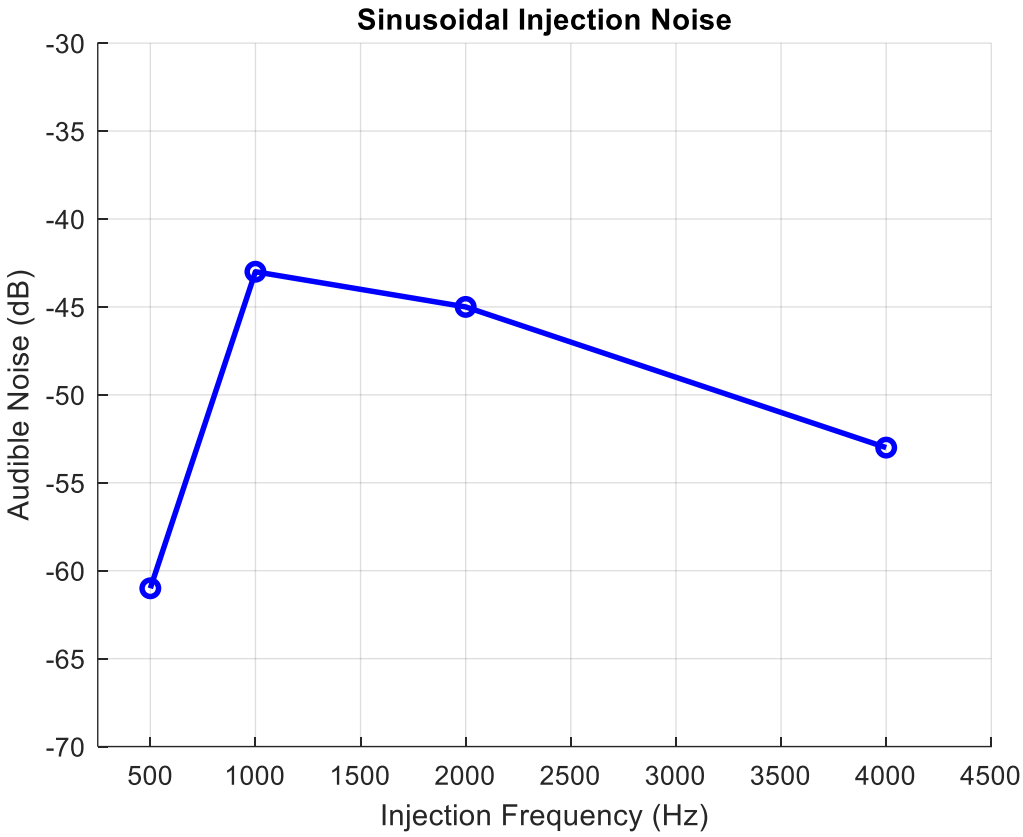

Figure 5.39. Sinusoidal Injection Noise Spectrum Summary

For the square-wave injection method, it is evident that additional harmonic content is introduced. When testing square-wave injection sensorless control, this additional noise is very palpable to the ears. Furthermore, the impact on having the inverter switching frequency below 20 kHz significantly increases the noise spectrum. Evident by increasing the switching frequency beyond 20 kHz, the benefit of utilizing SiC devices is shown. The next section will provide an analysis for the electrical angle error with respect to the inject frequency and switching frequency; an analysis was previously presented based on simulation results, so data can now be compared.

Angle Error Injection Frequency and Dynamic Response Analysis

The measured electrical angle extracted from the IPMSM resolver is compared with the electrical angle estimation to generate an angle error, with units in degrees. For Figure 5.40, the measured electrical angle is displayed in blue while the estimated electrical angle is shown in green. Figure 5.41 displays the output of the bandpass filter for a single-phase current in the HFI observer. The bandpass filter output demonstrates the induced current onto the motor windings from the injected voltage. Ideally, this induced current only appears on the d-axis when the angle error is driven to zero. Figure 5.42 provides data for the speed reference (orange), speed measurement (green), and speed estimation (yellow). The reference speed for this set of experiments is 150 RPM and 300 RPM in the clockwise direction (resulting in a negative speed value).

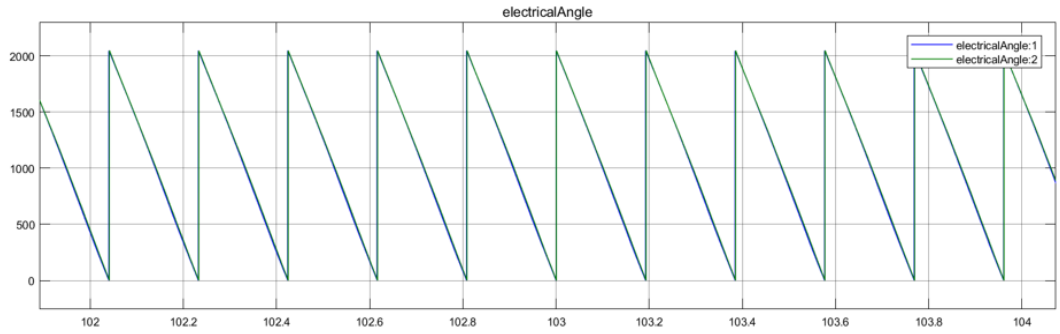

Figure 5.40. Electrical Angle Data from Resolver and HFI Observer

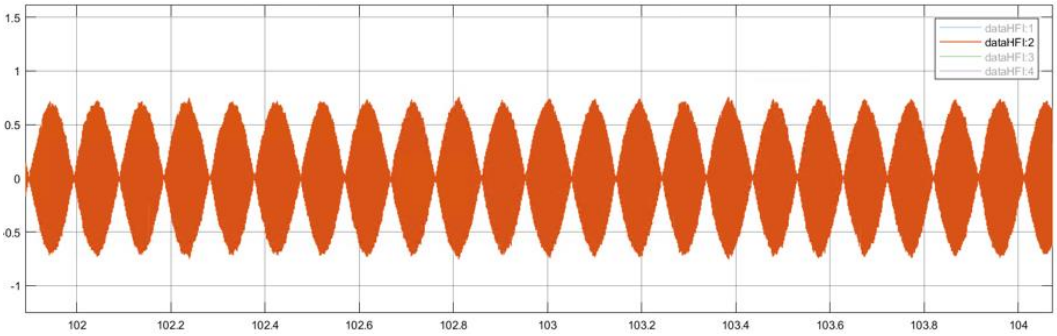

Figure 5.41. 500 Hz Injection Bandpass Filter Current Output

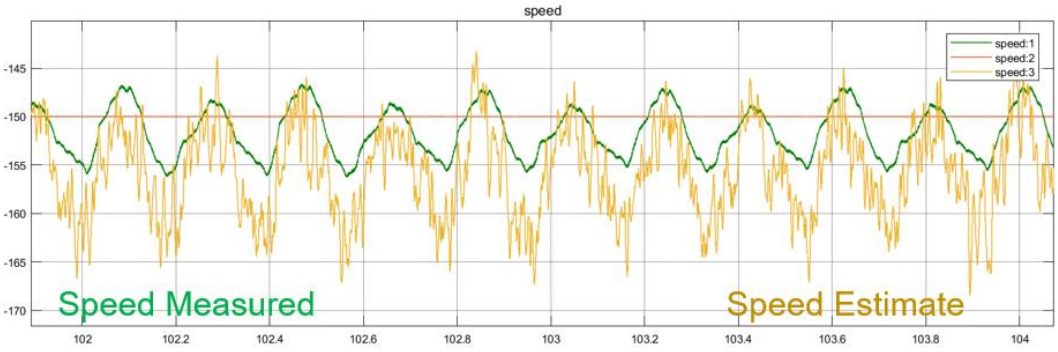

Figure 5.42. IPMSM Speed Measurement and HFI Observer Estimation

The following figures display the calculated angle error, with the units in degrees, and speed information for a sinusoidal and square-wave injection frequency at 500 Hz, 1 kHz, and 2 kHz. The switching frequency for each test is 20 kHz. Furthermore, the amplitude of the injection voltage is 25 Volts. Figure 5.43 compares the speed estimation with the measured speed and shows the calculated electrical angle for a 500 Hz sinusoidal injection signal at 150 RPM. Figure 5.44 shows 1 kHz sinusoidal injection data while Figure 5.45 displays 2 kHz sinusoidal injection data. Figure 5.45, Figure 5.46, and Figure 5.47 display data for the square-wave injection method at 500 Hz, 1 kHz, and 2 kHz. The peak to peak angle error ranges from 5 degrees to 8.5 degrees for sinusoidal and square-wave injection while a steady-state angle error offset is present. Additionally, the previously stated figures correlate speed data and the calculated angle error with the same tests shown in the audible noise section. Supplemental experiments were then conducted at 300 RPM. The sinusoidal injection method at 500 Hz is shown in Figure 5.49 and the sinusoidal injection method at 1 kHz is shown in Figure 5.50. Figure 5.51 presents speed data and angle error calculations for a 2 kHz sinusoidal injection signal. The peak to peak angle error ranges from 8 degrees to 12 degrees for the sinusoidal injection method at 300 RPM.

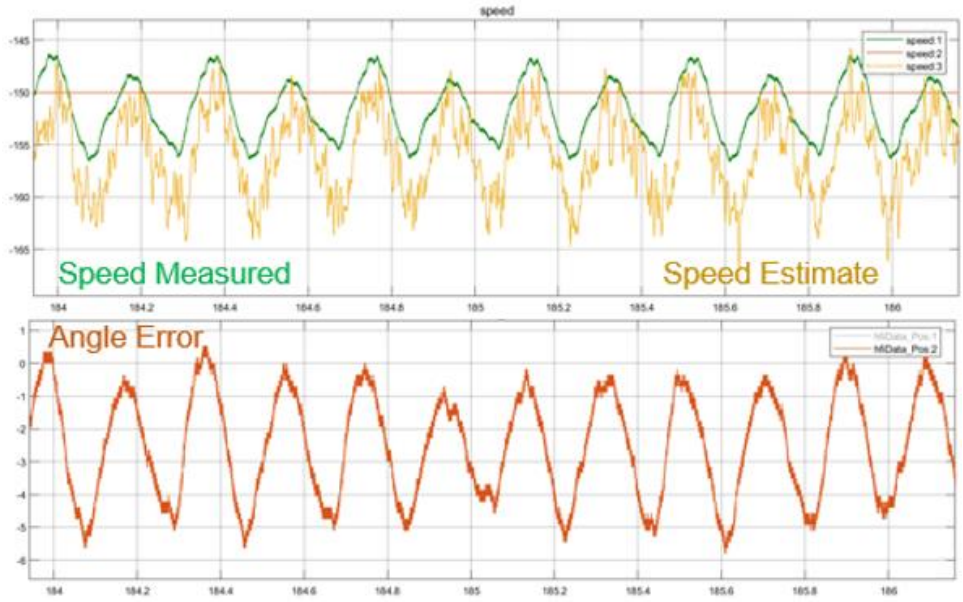

Figure 5.43. 500 Hz Sinusoidal Injection Speed and Angle Error Data

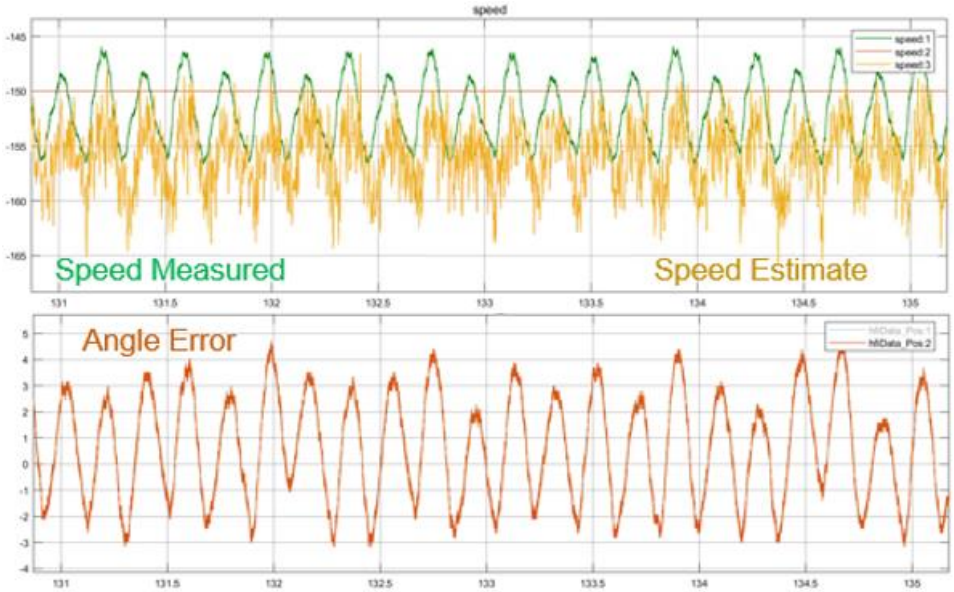

Figure 5.44. 1 kHz Sinusoidal Injection Speed and Angle Error Data

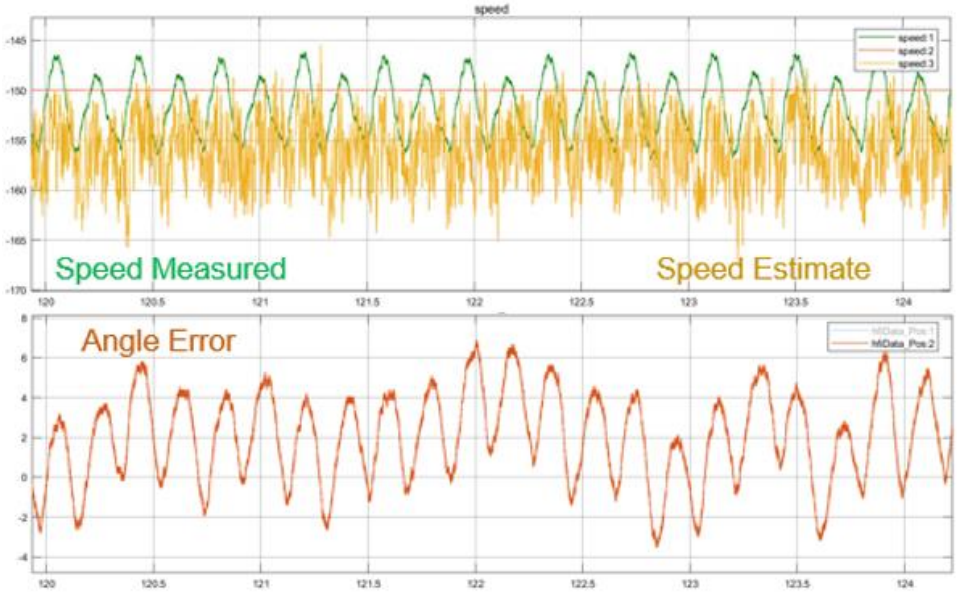

Figure 5.45. 2 kHz Sinusoidal Injection Speed and Angle Error Data

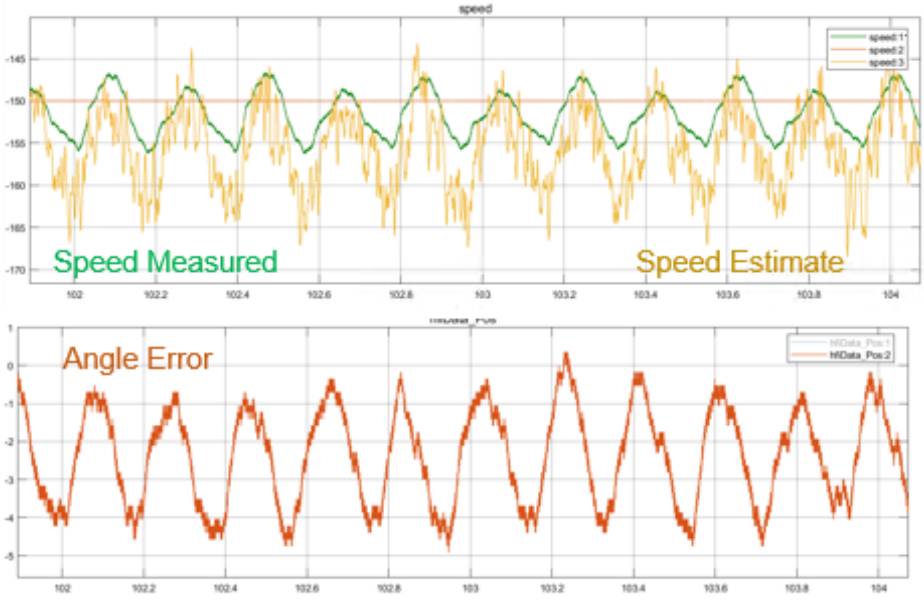

Figure 5.46. 500 Hz Square Wave Injection Speed and Angle Error Data

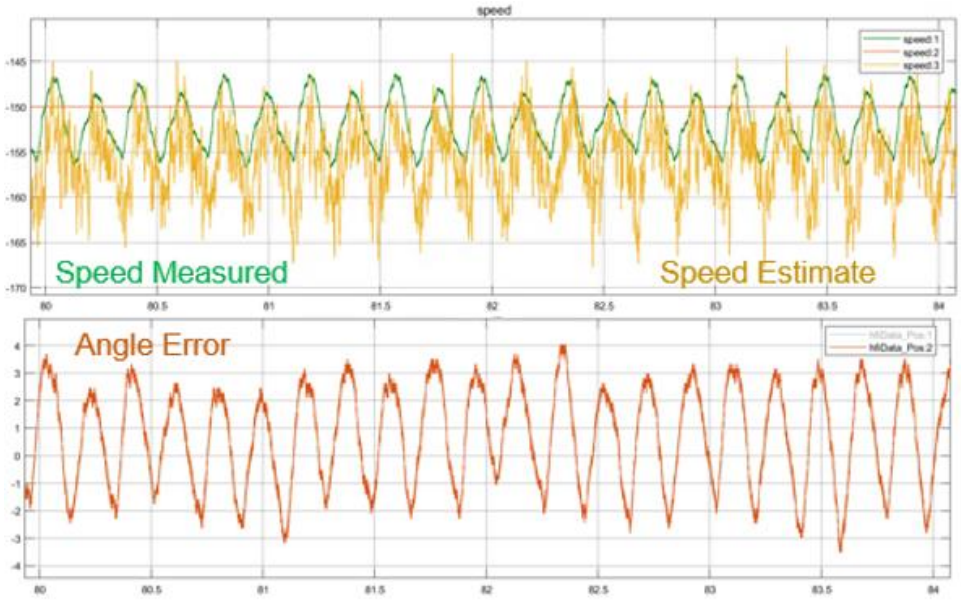

Figure 5.47. 1 kHz Square Wave Injection Speed and Angle Error Data

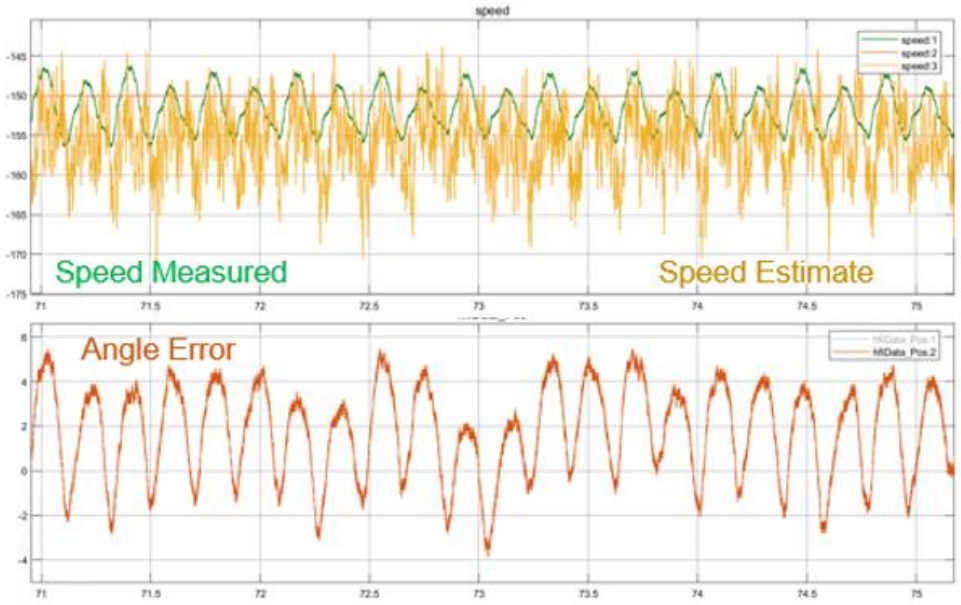

Figure 5.48. 2 kHz Square Wave Injection Speed and Angle Error Data

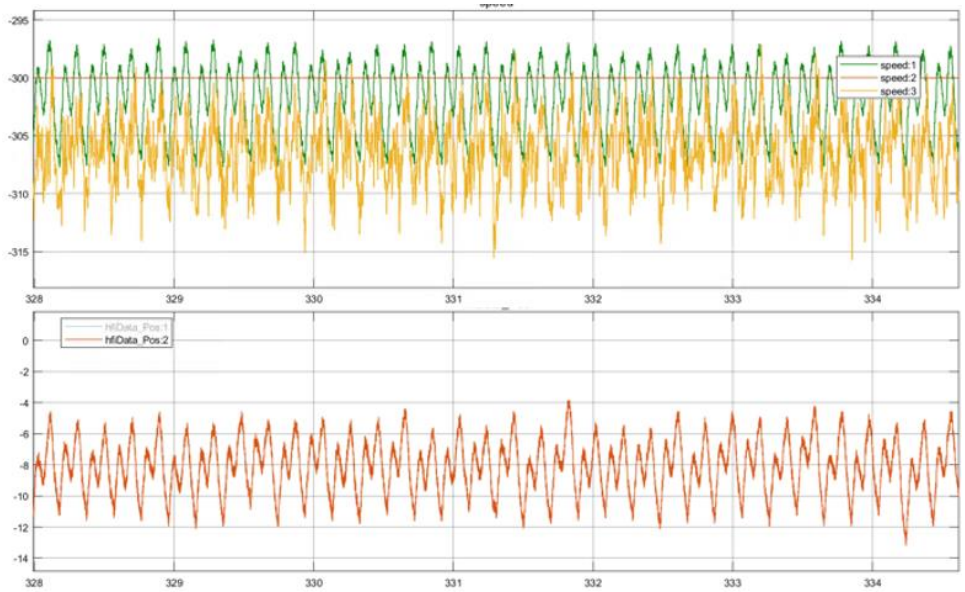

Figure 5.49. 300 RPM 500 Hz Sinusoidal Injection Speed and Angle Error Data

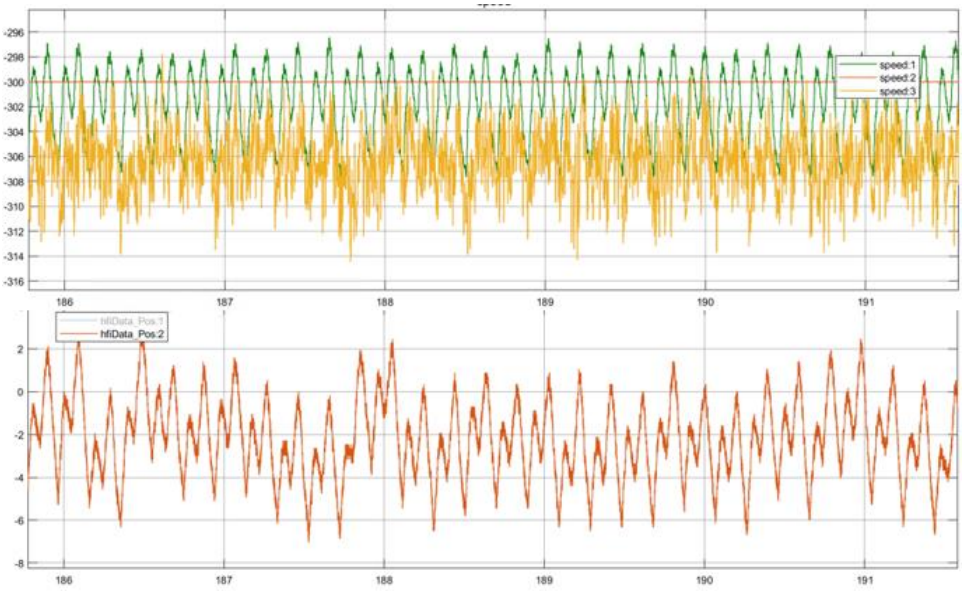

Figure 5.50. 300 RPM 1 kHz Sinusoidal Injection Speed and Angle Error Data

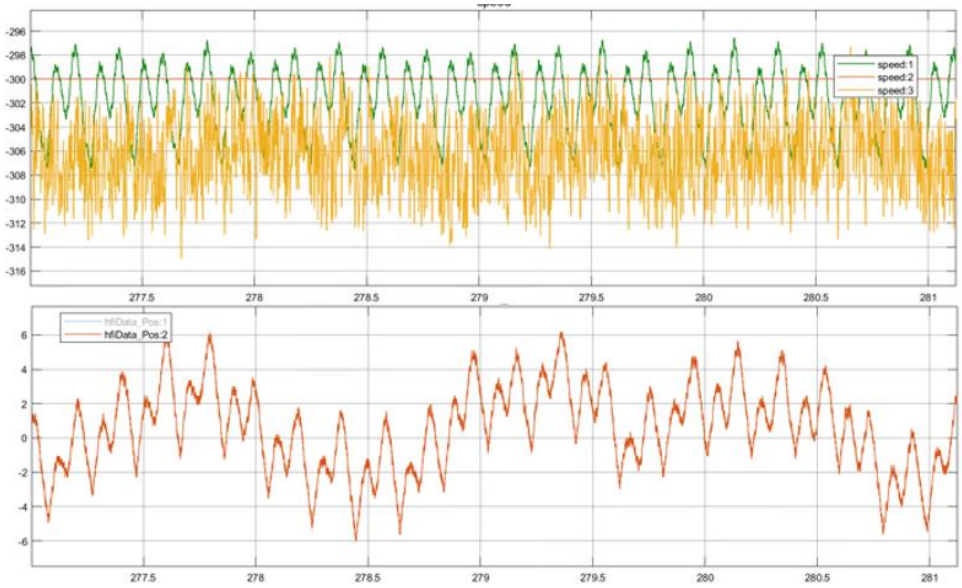

Figure 5.51. 300 RPM 2 kHz Sinusoidal Injection Speed and Angle Error Data

Peak to peak angle error data at 150 RPM can be summarized in Figure 5.52 in which the only variable changing is the injection frequency, holding the switching frequency constant at 20 kHz and injection voltage to 25 Volts. The peak to peak angle error is at a maximum for a 2 kHz sinusoidal injection frequency and a minimum for 500 Hz. However, this difference is only within a few electrical degrees. A 4 kHz sinusoidal signal injection is included in Figure 5.53 to compare the sinusoidal injection method peak to peak angle error for 150 RPM tests. The 4 kHz sinusoidal injection signal at 20 kHz switching frequency provides a poor estimation for the electrical angle as the controller bandwidth begins to narrow. An observation can be made in the DC offset of the angle error. This DC offset appears to become more negative as the speed increases. At a steady-state speed, oscillations in the angle error are present as the speed controller demonstrates a fluctuation about the speed reference. Data is presented in Figure 5.54 and Figure 5.55 to show the effective DC angle error offset at varying speed references and injection frequencies. For the dynamic response of HFI sensorless control, data is presented in Figure 5.56 to validate the simulation results similar to Figure 4.34 to show the impact the voltage injection amplitude has on improving the angle error during acceleration. The injection frequency is 500 Hz and the switching frequency is 20 kHz. Furthermore, voltages labeled V_1, V_2, V_3, V_4 represent the injection voltage amplitude that subsequentially increases. As the voltage is increased, the transient angle error is reduced.

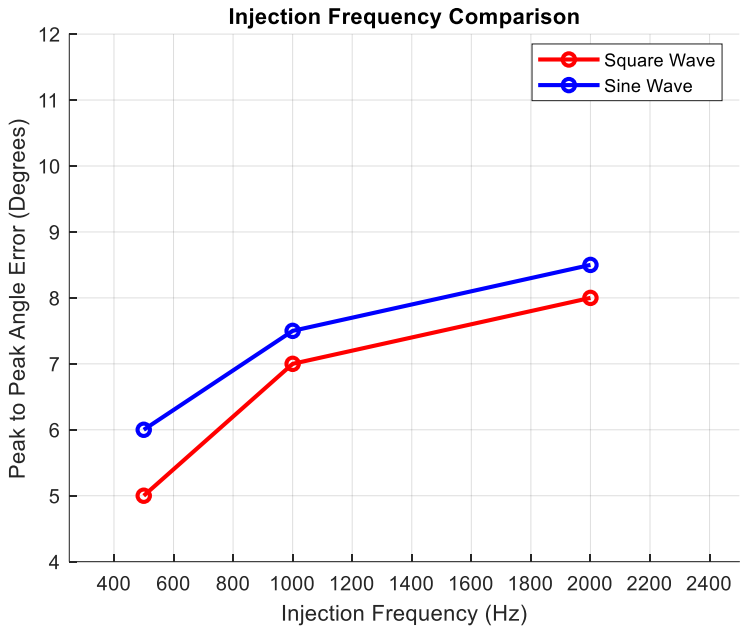

Figure 5.52. 150 RPM Injection Frequency Comparison at 20 kHz Switching Frequency

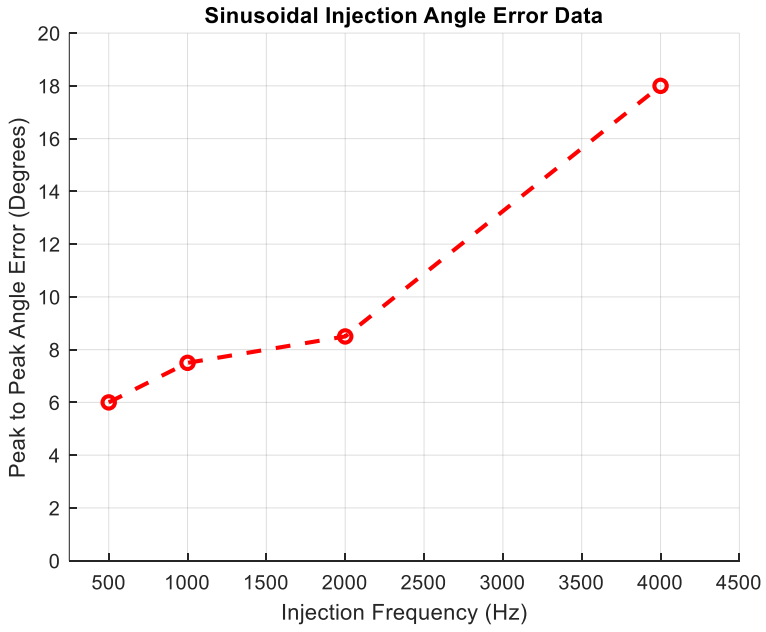

Figure 5.53. Peak to Peak Angle Error Sinusoidal Injection Summary

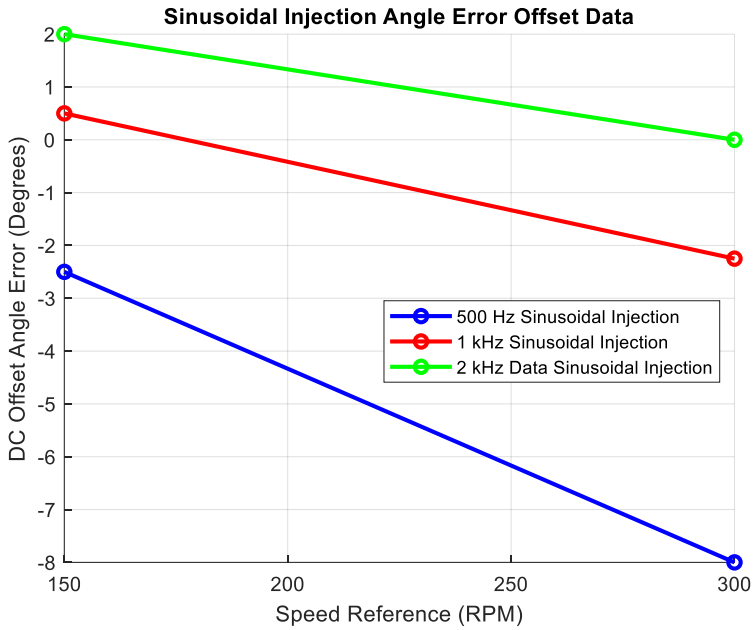

Figure 5.54. 25 V DC Offset Angle Error Sinusoidal Injection Summary

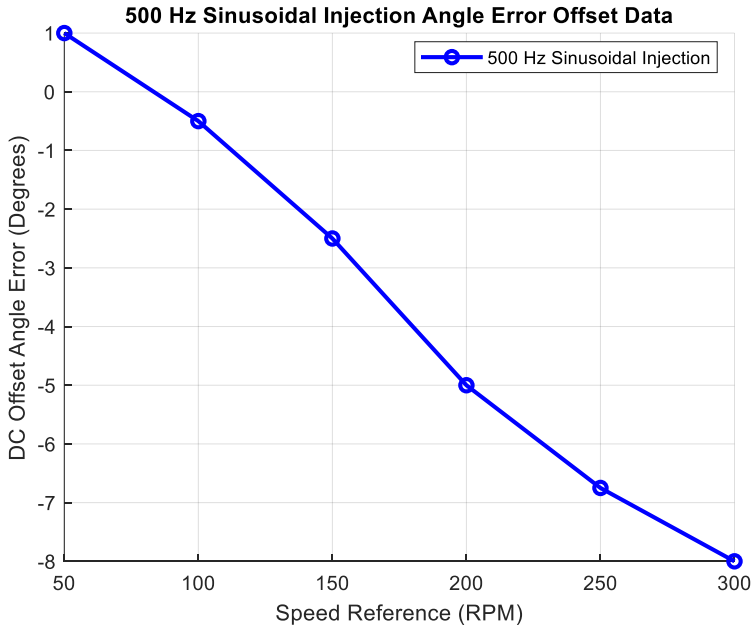

Figure 5.55. 500 Hz and 25 V DC Angle Error Offset vs. Speed Reference

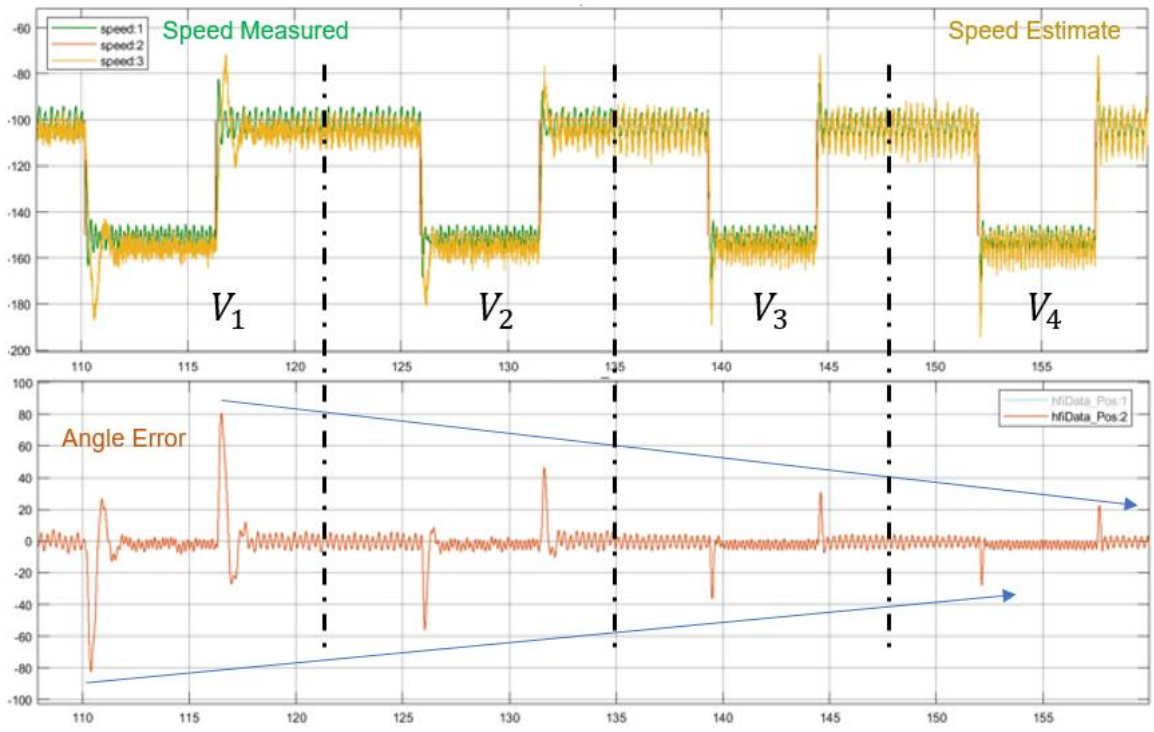

Figure 5.56. Dynamic Performance at 500 Hz Sinusoidal Injection at 20 kHz Switching Frequency

Control Bandwidth Analysis

Often, motor drive inverters operate at switching frequencies below 10 kHz and the control bandwidth is limited by the sequential instruction set of the programmed DSP. In this section, the injection frequencies will range from 500 Hz to 2 kHz. At each injection frequency, tests will be conducted at different switching frequencies. The control frequency, a defined frequency where signals are sampled by the FPGA and updated with new data, is set to the same value as the switching frequency. For a 500 Hz injection frequency, data will be presented with a 5 kHz switching frequency and 20 kHz switching frequency; for a 1 kHz injection frequency, data will be presented with a 10 kHz switching frequency and 20 kHz switching frequency; for a 2 kHz injection frequency, data will be presented with a 20 kHz switching frequency and 40 kHz switching frequency. The speed of the IPMSM is set to 150 RPM and the voltage injection amplitude is set to 25 Volts while the DC bus voltage is 150 Volts. Figure 5.57 displays angle error data for a 500 Hz sinusoidal injection while Figure 5.58 exhibits the angle error data for a 1 kHz sinusoidal injection. Figure 5.59 shows angle error data for a 2 kHz sinusoidal injection method. The peak to peak angle error is slightly reduced as the switching frequency is increased. This occurs due to an increase in sampling rates with the sensorless control algorithm and higher resolution sinusoidal voltage signal injected onto the $d-axis$.

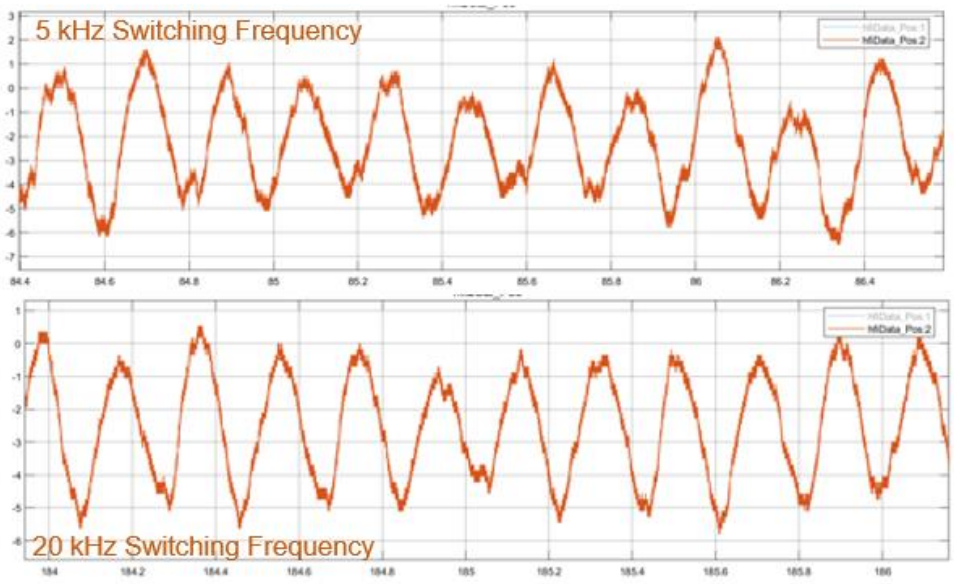

Figure 5.57. 500 Hz Sinusoidal Injection at 5 kHz and 20 kHz Switching Frequency

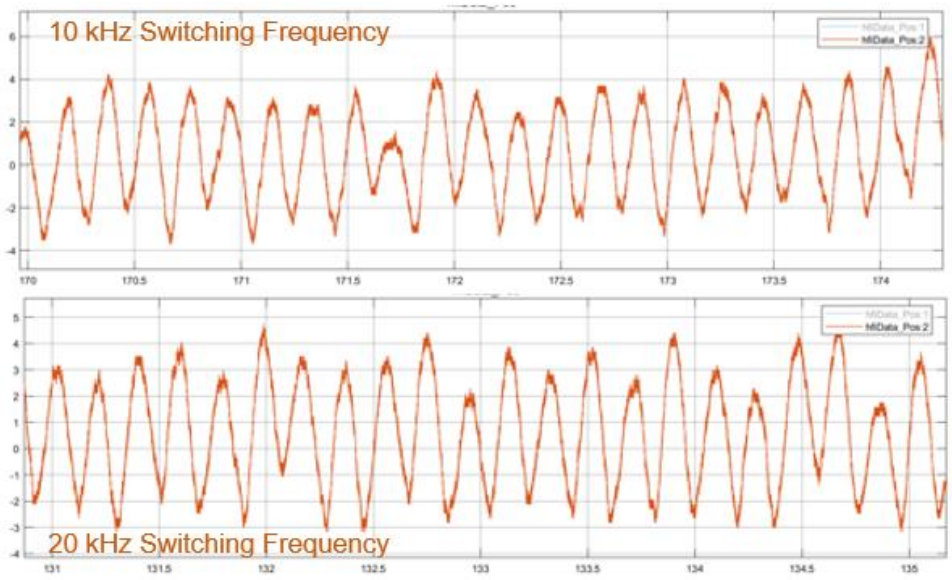

Figure 5.58. 1 kHz Sinusoidal Injection at 10 kHz and 20 kHz Switching Frequency

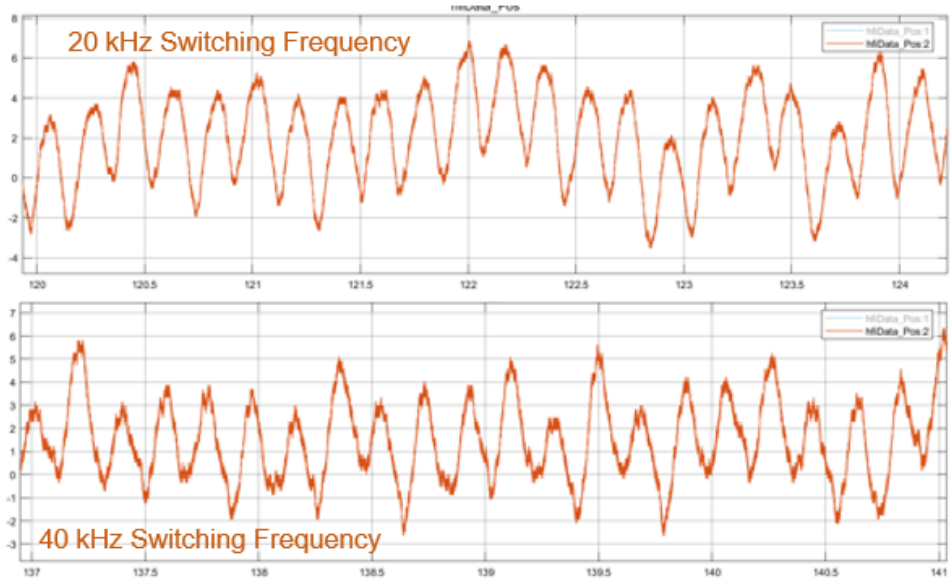

Figure 5.59. 2 kHz Sinusoidal Injection at 20 kHz and 40 kHz Switching Frequency

A summary of the resulting angle error after modifying the switching frequency can be seen in Figure 5.60. While the switching frequency adjustment may show a small improvement, the key variable for optimizing the angle error is the control frequency. Directly related to the control bandwidth, the control frequency is the rate at which one complete control loop cycle is completed. Parallel processing capabilities of an FPGA allow for a reduced execution time for one complete control loop cycle. The following test displays the peak to peak angle error results when the control frequency is modified from its maximum value, equivalent to the switching frequency, and a minimum value, equivalent to the frequency at which the control system becomes unstable. By slowing down the rate at which data is sampled and the rate at which duty cycle calculations are updated, the peak to peak angle error gets worse. Figure 5.61 displays a 500 Hz sinusoidal injection signal test with a switching frequency of 20 kHz; however, the rate at which calculations are updated is modified. When data is sampled below 3 kHz for a 500 Hz sinusoidal injection signal, the control system becomes unstable, resulting in the inability to properly control the IPMSM at a desired speed. With the ability to reach switching frequencies beyond 20 kHz, and the control bandwidth provided by the FPGA, flexible HFI sensorless control algorithms can be created to modify the injection frequency, injection voltage amplitude, and switching frequency under various speed references.

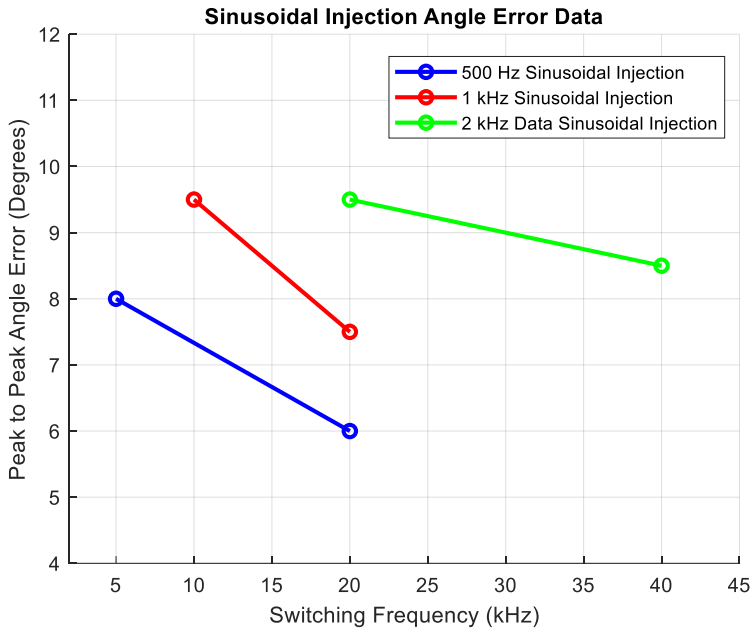

Figure 5.60. Switching Frequency Modification Data Summary

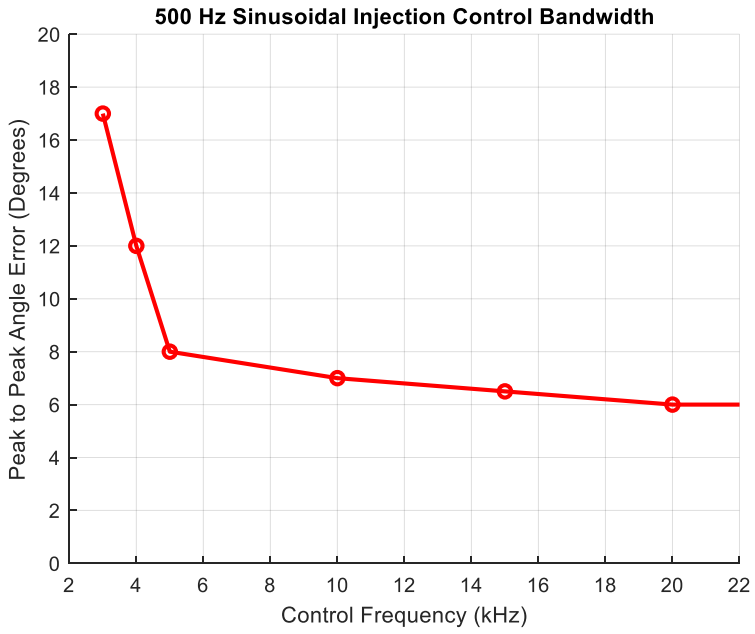

Figure 5.61. 500 Hz Injection Control Frequency Angle Error Data

Summary

Experimental results verify many simulation results for HFI sensorless control. Previous figures demonstrate experimental results, displaying the angle error as changes occur with the injection frequency, switching frequency, injection voltage, and speed reference. Furthermore, experimental data is presented for square-wave injection testing. Conclusions can then be summarized. 1) In regard to the audible noise introduced through signal injection, square-wave injection significantly increases undesirable noise in the motor drive system for each injection frequency. 2) Increasing the injection voltage amplitude during acceleration phases reduces the angle error. Also, increasing the injection voltage amplitude provides an SNR improvement when estimating the electrical angle error. 3) Oscillations in the angle error can be derived from control system tuning and response times. With a tighter control of the speed and current, the speed estimation oscillation will reduce. 4) Increasing the control bandwidth of the HFI sensorless control algorithm will reduce the angle error – demonstrating opportunities for FPGA driven sensorless control methods.

CHAPTER SIX

CONCLUSION AND FUTURE WORK

As WBG devices are utilized for power density improvements in motor drive inverters, HFI sensorless control algorithms can take advantage of high switching frequencies. However, a large control bandwidth must accompany this increase in switching frequency. In this thesis, HFI sensorless motor control is driven by an FPGA controlled SiC inverter to analyze the opportunities presented by increasing the inverter switching frequency and control bandwidth. A pulsating high frequency injection method was developed for an FPGA. The resulting algorithm allowed for the exploration of the impact a high control bandwidth FPGA has on estimating the IPMSM rotor position. Furthermore, injection frequency and injection voltage values were manipulated at different speed references to provide insight into the relationship between the angle error and HFI signals; the introduced audible noise from HFI sensorless control was also explored.

HFI Sensorless Control

Within this thesis, a SiC inverter controlled by a Xilinx FPGA was utilized. Simulation developments were made in MATLAB Simulink in which multiple speed references were set while the injection frequency, injection voltage, and switching frequency were changed. System Generator, a model-based programming environment in Simulink, was then utilized to develop the HFI

sensorless control method for the Xilinx FPGA. Experimental testing was conducted, with real-time data visualization and control made possible through the AXI4-Lite Interface in Simulink. Data presented in this thesis demonstrate several relationships that HFI sensorless control methods have on the angle error and noise spectrum. 1) The square-wave injection method significantly increases undesirable noise in the motor drive system for each injection frequency compared to the sinusoidal injection method independent of the switching frequency. 2) The switching frequency must go beyond 20 kHz to further reduce the presence of undesirable noise in the motor drive system. 3) The control bandwidth of the FPGA offers an improved angle error as the rate at which the control system responds can reduce oscillations in the speed estimation. 4) Increasing the injection voltage amplitude during acceleration phases will reduce the angle error assuming the injection frequency and switching frequency are held constant. The transient response of the speed tracking controller will be amplified with this voltage increase. 5) Increasing the injection frequency can offer a solution to compensating for the steady-state angle error offset as speed references are increased.

Future Work

Future research routes have been identified upon the completion of this thesis. While experimental data focuses on speed controller references, the load torque is not adjusted. The load torque must now become a variable of interest, resulting in a wider range of current through the motor windings. At varying load

torque conditions, the torque ripple introduced from HFI sensorless control must be investigated. Additionally, the steady state angle error offset must be explored and compensated for to improve the HFI sensorless control method. Upon the examination of load torque variations and a steady state angle error offset, the final HFI algorithm should be compared to the high speed sensorless control methods to find the limit at which HFI should be utilized instead of the preferred high speed sensorless control methods, such as the Back EMF method.

LIST OF REFERENCES

[1] Department of Energy (DOE) Office of Energy Efficiency and Renewable Energy (EERE), "DE-FOA-0002420: Vehicle Technologies Office Fiscal Year 2021 Research Funding Opportunity Announcement," 2021.

[2] Office of Energy Efficiency and Renewable Energy, "US DRIVE Electrical and Electronics Technical Team Roadmap," 2017.

[3] Eaton Corporation, "High Voltage Traction Inverter," [Online]. Available: https://www.eaton.com/us/en-us/catalog/emobility/high-voltage-inverter.html.

[4] STMicroelectronics, "Electric Vehicle Ecosystem: Traction Inverter," [Online]. Available: https://www.st.com/content/ccc/resource/sales_and_marketing/promotional_material/brochure/group0/5f/66/06/cf/a3/85/42/90/BREVECO_Electric_vehicle_ecosystem/files/BREVECO0518.pdf/jcr:content/translations/en.BREVECO0518.pdf.

[5] R. W. Erickson and D. Maksimovic, Fundamentals of Power Electronics (Second Edition), 2001, p. 87.

[6] Infineon Technologies, "Hybrid Kit Drive 1200V," 2019. [Online]. Available: https://www.infineon.com/cms/en/product/evaluation-boards/hybrid-kit-drive-1200v/#!documents.

[7] L. M. Tolbert, B. Ozpineci, S. K. Islam and M. S. Chinthavali, "Wide Bandgap Semiconductors for Utility Applications," *IASTED International*

Conference on Power and Energy Systems, 2003.

[8] A. Q. Huang, "Power Semiconductor Devices for Smart Grid and Renewable Energy Systems," *Proceedings of the IEEE,* vol. 105, no. 11, pp. 2019-2047, November 2017.

[9] A. Lidow, M. d. Rooij, J. Strydom, D. Reusch and J. Glaser, GaN Transitors for Efficienct Power Conversion, 2020, p. 4.

[10] F. Y. Fu, "From Silicon to GaN: What Power Electronics Engineers Need to Know About GaN," in *IEEE Energy Conversion Congress & Expo (ECCE)*, 2019.

[11] Wolfspeed, "SiC Power Modules".

[12] Wolfspeed, "Discrete SiC MOSFETs".

[13] EPC (Efficient Power Conversion), "Recommended Devices for Motor Drive".

[14] GaN Systems, "GaN Transistors 100 V E-HEMT".

[15] GaN Systems, "650V 300A 3-Phase GaN Power Module".

[16] Wolfspeed, "Enabling System upgrades with SiC technology using industry standard base-plate-less packaging," 2021.

[17] H. Mohan, M. K. Pathak and S. K. Dwivedi, "Sensorless Control of Electric Drives – A Technological Review," *IETE Technical Review,* vol. 37, no. 5, pp. 504-528, 2020.

[18] Analog Devices, "Precision Resolver-to-Digital Converter Measures

Angular Position and Velocity".

[19] C. Mi and M. A. Masrur, Hybrid Electric Vehicles: Principles and Applications with Practical Perspectives, Second ed., John Wiley & Sons Ltd., 2018, p. 287.

[20] A. Glumineau and J. d. L. Morales, Sensorless AC Electric Motor Control: Robust Advanced Design Techniques and Applications, 2015, pp. 14-21.

[21] P. Krause, O. Wasynczuk, S. Sudhoff and S. Pekarek, Analysis of Electric Machinery and Drive Systems, 2013.

[22] A. Glumineau and J. d. L. Morales, "Sensorless AC Electric Motor Control: Robust Advanced Design Techniques and Applicaitons," 2015.

[23] R. T. Ramamoorthy, B. Larimore and M. Bhardwaj, "Sensored Field Oriented Control of 3-Phase Permanent Magnet Synchronous Motors Using TMS320F2837x," 2016.

[24] A. Glumineau and J. d. L. Morales, Sensorless AC Electric Motor Control: Robust Advanced Design Techniques and Applicaitons, 2015, pp. 12-13.

[25] MathWorks, "Field-Oriented Control," [Online]. Available: https://www.mathworks.com/solutions/power-electronics-control/field-oriented-control.html.

[26] F. Genduso, R. Miceli, R. Rando and G. Galluzzo, "Back EMF

Sensorless-Control Algorithm for High-Dynamic Performance PMSM," *IEEE Trans. Ind. Electron,* vol. 57, no. 6, pp. 2092-2100, 2010.

[27] B. Nahid-Mobarakeh, F. Meibody-Tabar and F. Sargos, "Back EMF Estimation-Based Sensorless Control of PMSM: Robustness With Respect to Measurement Errors and Inverter Irregularities," *IEEE Trans. on Ind. Applicat.,* vol. 43, no. 2, p. 485–494, 2007.

[28] B. Nahid-Mobarakeh, F. Meibody-Tabar and F. Sargos, "Mechanical Sensorless Control of PMSM with Online Estimation of Stator Resistance," *Conference Record of the 2002 IEEE Industry Applications Conference. 37th IAS Annual Meeting,* pp. 628-635, 2002.

[29] F. Lin, Y. Hung, J. Chen and C. Yeh, "Sensorless IPMSM Drive System Using Saliency Back-EMF-Based Intelligent Torque Observer With MTPA Control," *IEEE Transactions on Industrial Informatics,* vol. 10, no. 2, p. 1226–1241, 2014.

[30] C. Zhiqian, M. Tomita, S. Ichikawa, S. Doki and S. Okuma, "Sensorless control of interior permanent magnet synchronous motor by estimation of an extended electromotive force," *Conference Record of the 2000 IEEE Industry Applications Conference,* vol. 3, pp. 1814-1819, 2000.

[31] H. Kim, M. Harke and R. Lorenz, "Sensorless control of interior permanent-magnet machine drives with zero-phase lag position estimation," *IEEE Transactions on Industry Applications,* vol. 39, no. 6,

2003.

[32] H. Zhu, X. Xiao and Y. Li, "A simplified high frequency injection method for PMSM sensorless control," *IEEE 6th International Power Electronics and Motion Control Conference,* pp. 401-405, 2009.

[33] Z. Wang, K. Lu, Y. Ye, Y. JIn and W. Hong, "Analysis of influence on back-EMF based sensorless control of PMSM due to parameter variations and measurement errors," *International Conference on Electrical Machines and Systems,* pp. 1-6, 2011.

[34] M. Hamida, J. Leon, A. Glumineau and R. Boisliveau, "An Adaptive Interconnected Observer for Sensorless Control of PM Synchronous Motors With Online Parameter Identification," *IEEE Transactions on Industrial Electronics,* vol. 60, no. 2, pp. 739-748, 2013.

[35] F. Chen, X. Jiang, X. Ding and C. Lin, "FPGA-based sensorless PMSM speed control using adaptive sliding mode observer," *IECON 2017 - 43rd Annual Conference of the IEEE Industrial Electronics Society,* p. 4150–4154, 2017.

[36] H. M. D. Habbi and A. A. Al-Khazraji, "FPGA based vector control of PM motor using sliding mode observer," *Modern Electric Power Systems (MEPS),* pp. 1-5, 2015.

[37] Y. Zhao, W. Qiao and L. Wu, "Position extraction from a discrete sliding-mode observer for sensorless control of IPMSMs," *IEEE International*

Symposium on Industrial Electronics, pp. 725-730, 2012.

[38] Y.-S. Han, J.-S. Choi and Y.-S. Kim, "Sensorless PMSM drive with a sliding mode control based adaptive speed and stator resistance estimator," *IEEE Transactions on Magnetics,* vol. 36, no. 5, p. 3588–3591, 2000.

[39] N. Quang, N. Hieu and Q. P. Ha, "FPGA-Based Sensorless PMSM Speed Control Using Reduced-Order Extended Kalman Filters," *IEEE Trans. Ind. Electron,* vol. 61, no. 12, p. 6574–6582, 2014.

[40] N. Quang, D. D. Tung and Q. P. Ha, "FPGA-based sensorless PMSM speed control using adaptive extended Kalman filter," *IEEE International Conference on Automation Science and Engineering (CASE),* p. 1650–1655, 2015.

[41] J.-S. Jang, B. Park, T.-S. Kim, D. M. Lee and D.-S. Hyun, "Parallel reduced-order Extended Kalman Filter for PMSM sensorless drives," *34th Annual Conference of IEEE Industrial Electronics,,* p. 1326–1331, 2008.

[42] Y.-H. Kim and Y.-S. Kook, "High performance IPMSM drives without rotational position sensors using reduced-order EKF," *IEEE Transactions on Energy Conversion,* vol. 14, no. 4, p. 868–873, 1999.

[43] W. Wenjie, Z. Min and W. Qinghai, "Application of Reduced-Order Extended Kalman Filter in Permanent Magnet Synchronous Motor

Sensorless Regulating System," *International Conference on Digital Manufacturing Automation,* 2010.

[44] H. Yang, R. Yang, W. Hu and Z. Huang, "FPGA-Based Sensorless Speed Control of PMSM Using Enhanced Performance Controller Based on the Reduced-Order EKF," *IEEE J. Emerg. Sel. Topics Power Electron,* 2019.

[45] Z. Ma and X. Zhang, "FPGA-based sensorless control for PMSM drives using the stator/rotor frame extended Kalman filter," in *Chinese Control And Decision Conference (CCDC)*, 2018.

[46] P. Kumar, O. Bottesi, S. Calligaro, L. Alberti and R. Petrella, "Self-Adaptive High-Frequency Injection Based Sensorless Control for Interior Permanent Magnet Synchronous Motor Drives," *Energies,* vol. 12, no. 19, 2019.

[47] P. L. Jansen and R. D. Lorenz, "Transducerless position and velocity estimation in induction and salient AC machines," IEEE Transactions on Industry Applications," *IEEE Transactions on Industry Applications,* vol. 31, no. 2, pp. 240-247, 1995.

[48] J. Cilia, G. M. Asher and K. J. Bradley, "Sensorless position detection for vector controlled induction motor drives using an asymmetric outer-section cage," in *IEEE Industry Applications Conference*, 1996.

[49] N. Teske, G. M. Asher, M. Sumner and K. J. Bradley, "Encoderless

position estimation for symmetric cage induction machines under loaded conditions," *IEEE Transactions on Industry Applications,* vol. 37, no. 6, pp. 1793-1800, 2001.

[50] A. Arias, C. A. Silva, G. M. Asher, J. C. Clare and P. W. Wheeler, "Use of a matrix converter to enhance the sensorless control of a surface-mount permanent-magnet AC motor at zero and low frequency," *IEEE Transactions on Industrial Electronics,,* vol. 53, no. 2, pp. 440-449, 2006.

[51] C. Silva, G. M. Asher and M. Sumner, "Hybrid rotor position observer for wide speed-range sensorless PM motor drives including zero speed," *IEEE Transactions on Industrial Electronics,* vol. 53, no. 2, p. 373–378, 2006.

[52] S. Damkhi, M. S. N. Said and N. N. Said, "Slotting effects and high frequency signal injection for induction machine rotor speed estimation," in *International Conference and Exposition on Electrical and Power Engineering*, 2012.

[53] G. Zhang, G. Wang and D. Xu, "Saliency-based position sensorless control methods for PMSM drives - A review," *Chin. J. Electr. Eng,* vol. 3, no. 2, pp. 14-23, 2017.

[54] S. Medjmadj, D. Diallo, M. Mostefai, C. Delpha and A. Arias, "PMSM Drive Position Estimation: Contribution to the High-Frequency Injection Voltage Selection Issue," *IEEE Trans. Energy Convers.,* vol. 30, no. 1,

pp. 349-358, 2015.

[55] Y. Zhao, Z. Zhang, C. Ma, W. Qiao and L. Qu, "Sensorless control of surface-mounted permanent-magnet synchronous machines for low-speed operation based on high-frequency square-wave voltage injection," *IEEE Industry Applications Society Annual Meeting,* pp. 1-8, 2013.

[56] W. Qian, X. Zhang, F. Jin, H. Bai, D. Lu and B. Cheng, "Using High-Control-Bandwidth FPGA and SiC Inverters to Enhance High-Frequency Injection Sensorless Control in Interior Permanent Magnet Synchronous Machine," *IEEE Access,* 2018.

[57] Y. Yoon, S. Sul, S. Morimoto and K. Ide, "High-bandwidth sensorless algorithm for AC Machines based on square-wave-type voltage injection," *IEEE Trans. Ind Appl.,* vol. 47, no. 3, pp. 1361-1370, 2011.

[58] G. Ellis, Control System Design Guide: Using Your Computer to Understand and Diagnose Feedback Controllers, 4th ed., 2012.

[59] Xilinx, "Vivado Design Suite Tutorial: Model-Based DSP Design Using System Generator".

[60] Avnet, "ZedBoard: Zynq Evaluation and Development Hardware User's Guide," 2012.

[61] K. Shirabe, "Advantages of high frequency PWM in AC motor drive applications," *2012 IEEE Energy Conversion Congress and Exposition*

(ECCE), pp. 2977-2984, 2012.

APPENDIX

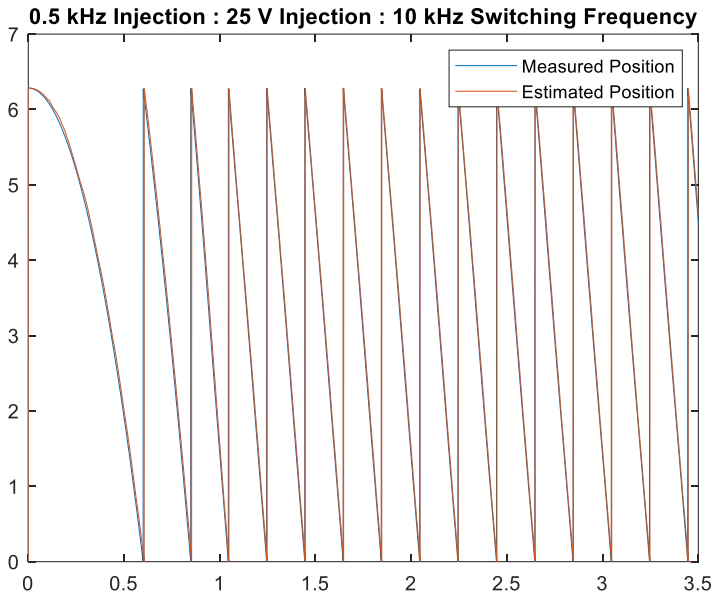

Figure A.1. 500 Hz, 25 V Sine Injection at 10 kHz Switching: Position Data

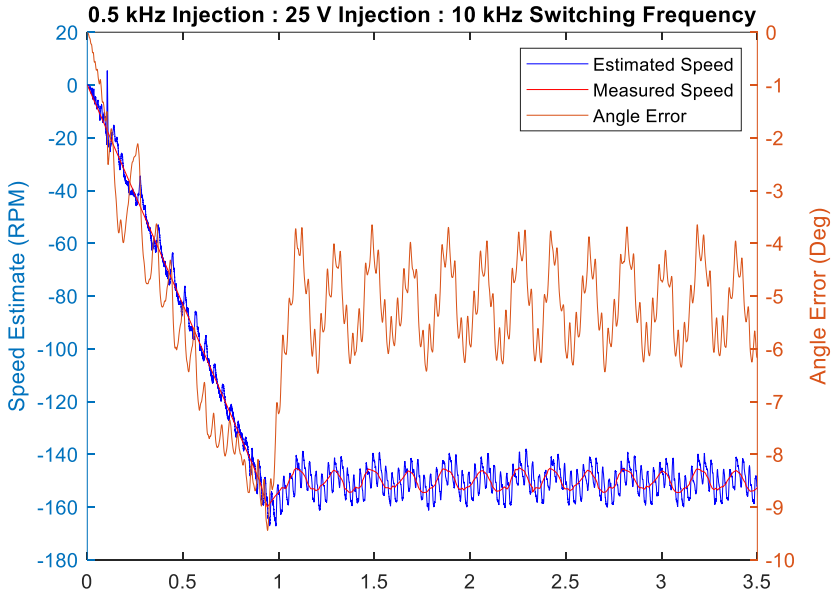

Figure A.2. 500 Hz, 25 V Sine Injection at 10 kHz Switching: Speed and Angle Error

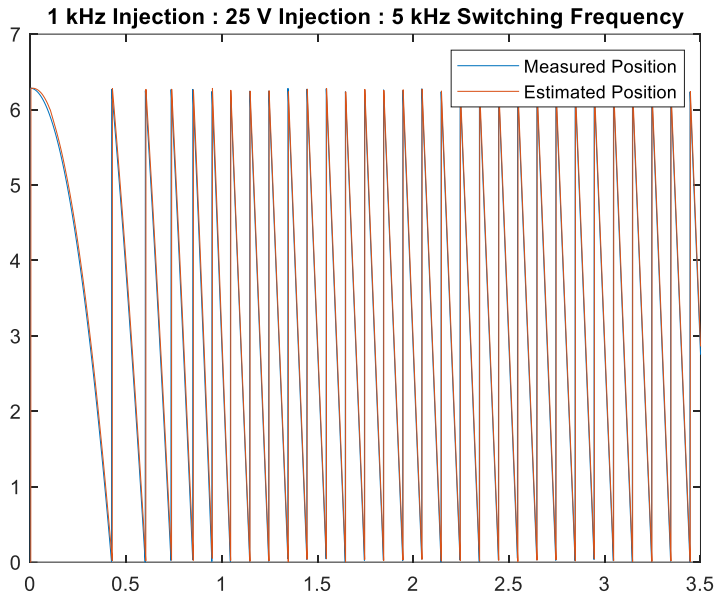

Figure A.3. 1 kHz, 25 V Sine Injection at 5 kHz Switching: Position Data

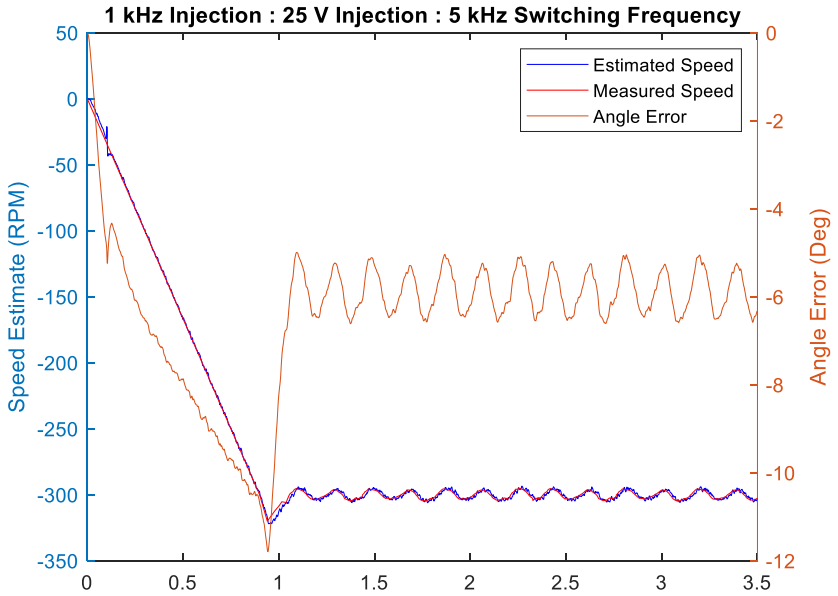

Figure A.4. 1 kHz, 25 V Sine Injection at 5 kHz Switching: Speed and Angle Error

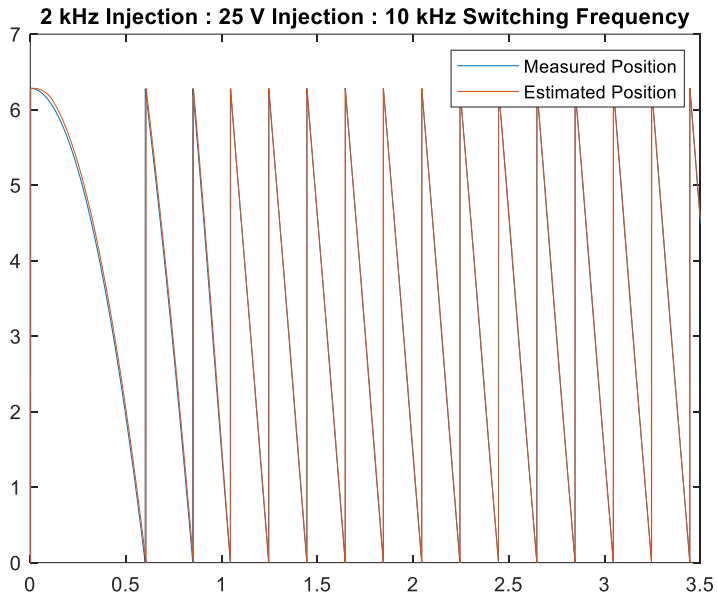

Figure A.5. 2 kHz, 25 V Sine Injection at 10 kHz Switching: Position Data

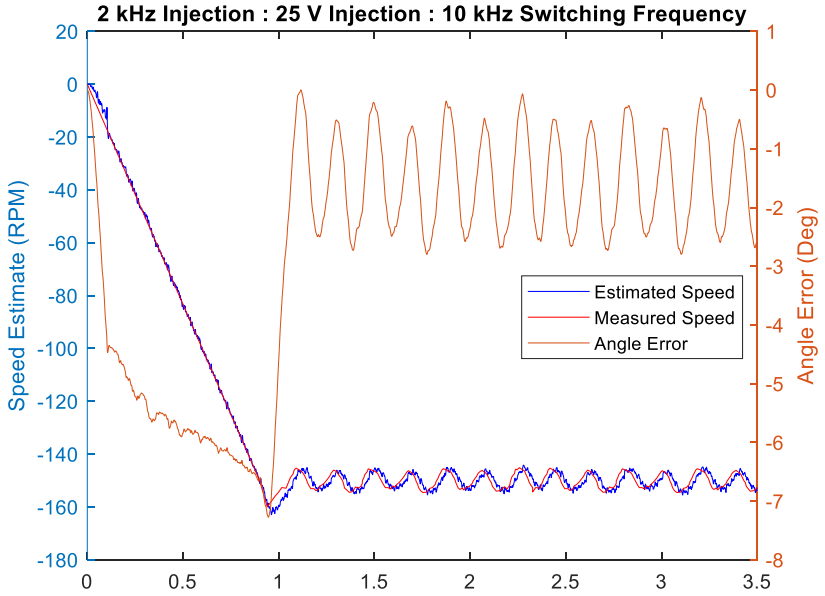

Figure A.6. 2 kHz, 25 V Sine Injection at 10 kHz Switching: Speed and Angle Error

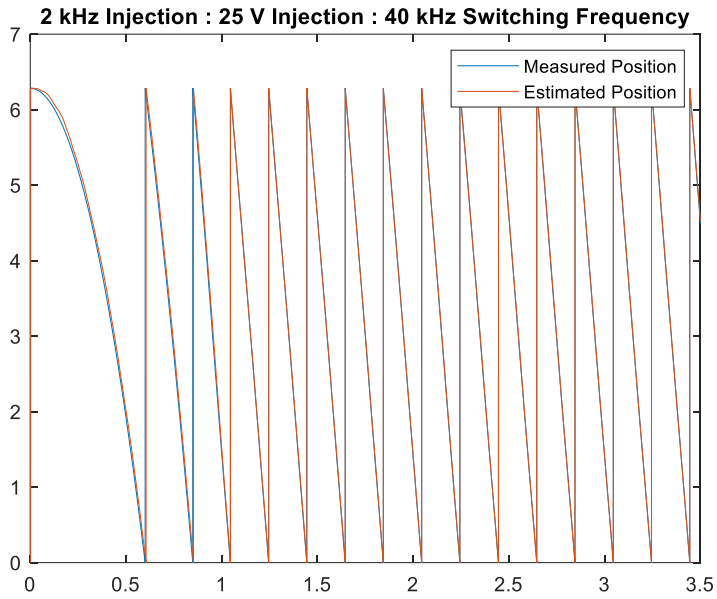

Figure A.7. 2 kHz, 25 V Sine Injection at 40 kHz Switching: Position Data

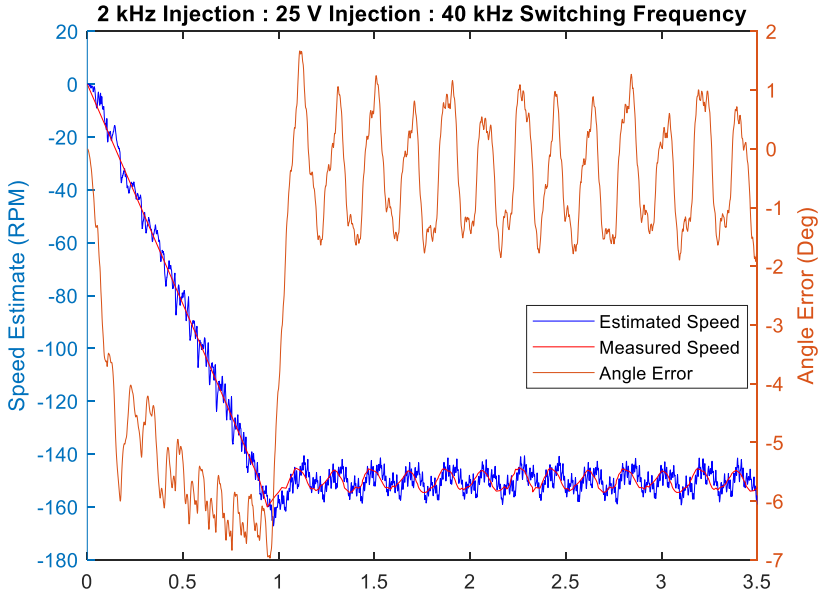

Figure A.8. 2 kHz, 25 V Sine Injection at 40 kHz Switching: Speed and Angle Error

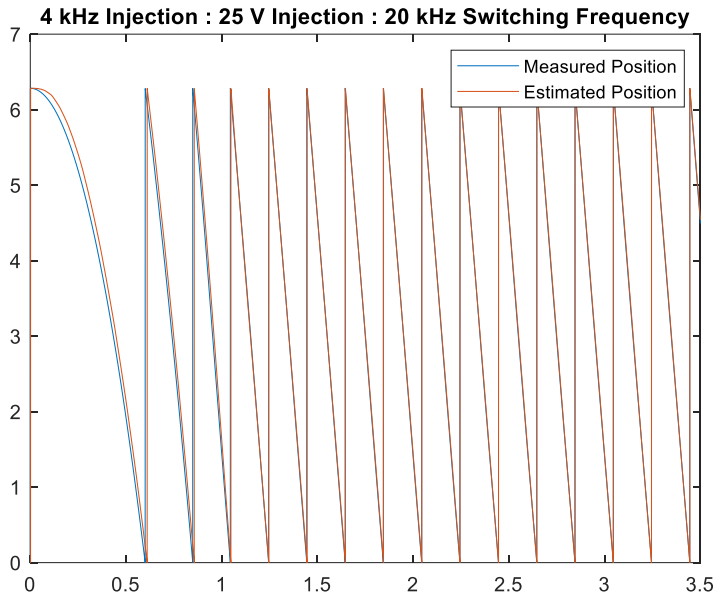

Figure A.9. 4 kHz, 25 V Sine Injection at 20 kHz Switching: Position Data

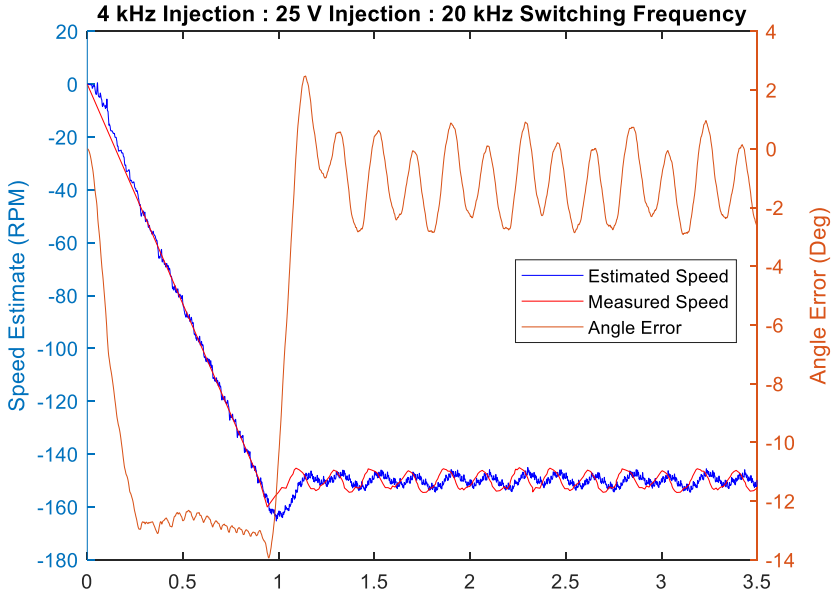

Figure A.10. 4 kHz, 25 V Sine Injection at 20 kHz Switching: Speed and Angle Error

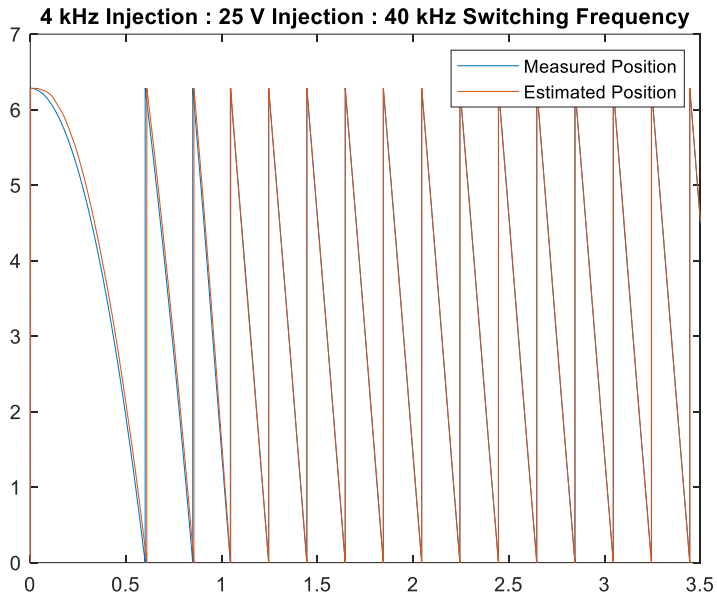

Figure A.11. 4 kHz, 25 V Sine Injection at 40 kHz Switching: Position Data

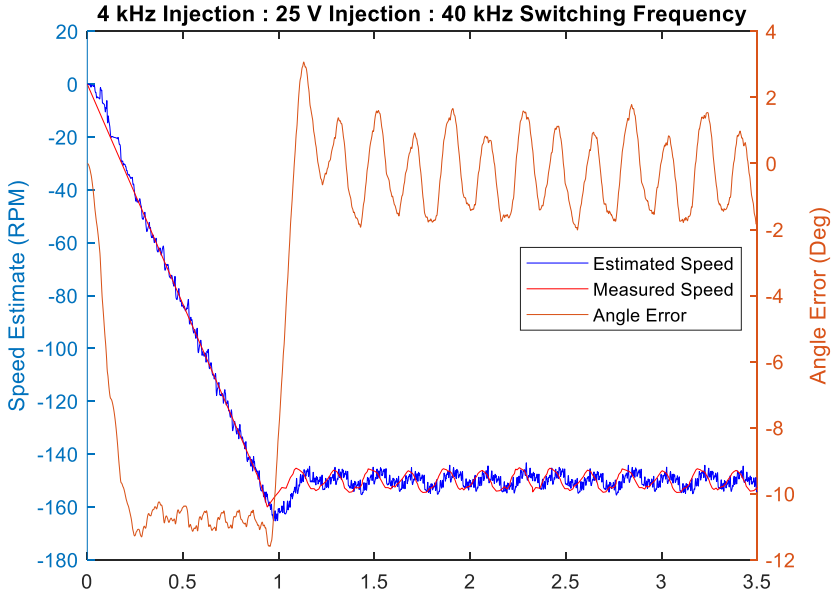

Figure A.12. 4 kHz, 25 V Sine Injection at 40 kHz Switching: Speed and Angle Error

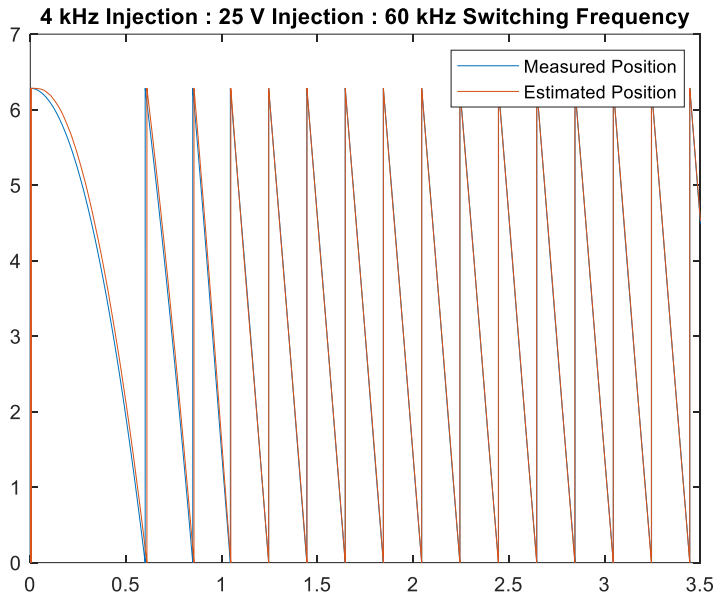

Figure A.13. 4 kHz, 25 V Sine Injection at 60 kHz Switching: Position Data

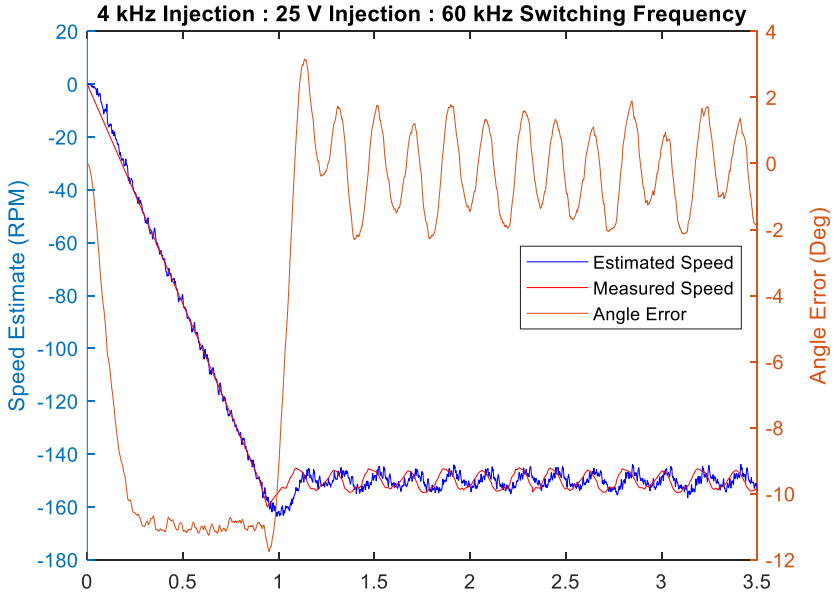

Figure A.14. 4 kHz, 25 V Sine Injection at 60 kHz Switching: Speed and Angle Error

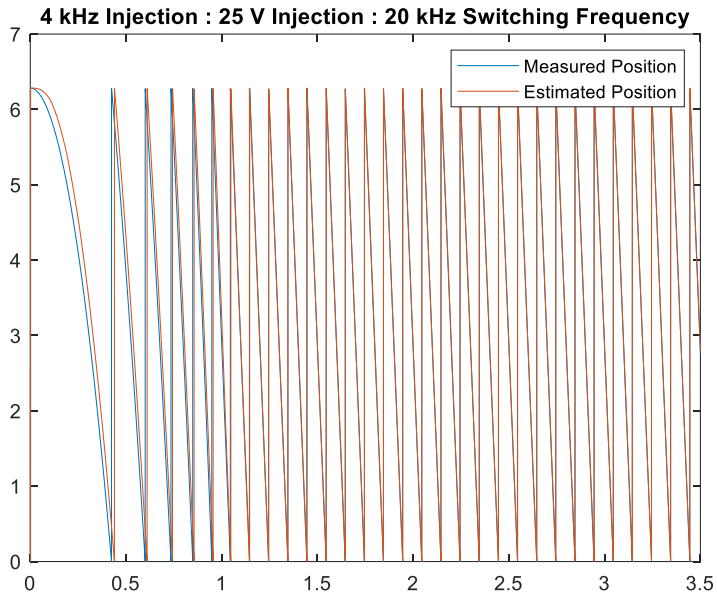

Figure A.15. 4 kHz Injection, 300 RPM at 20 kHz Switching: Position Data

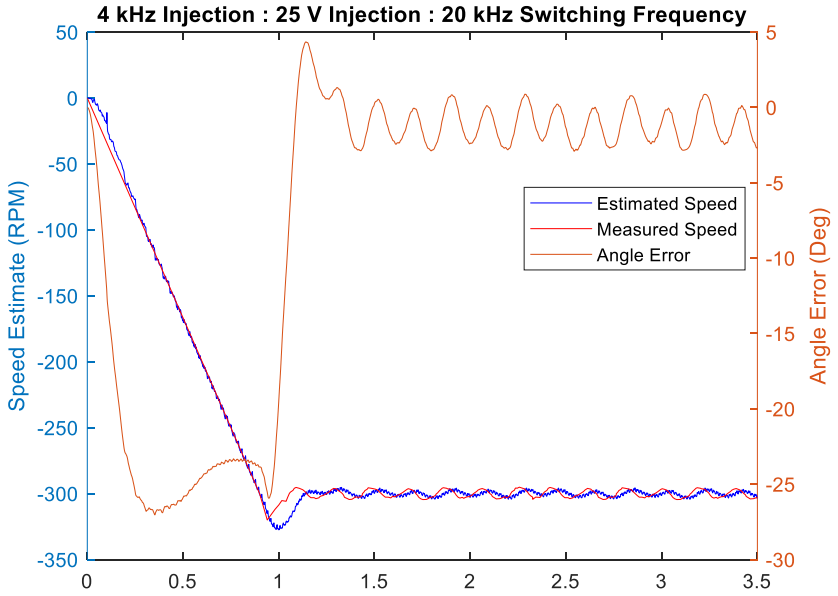

Figure A.16. 4 kHz Injection, 300 RPM at 20 kHz Switching: Speed and Angle Error

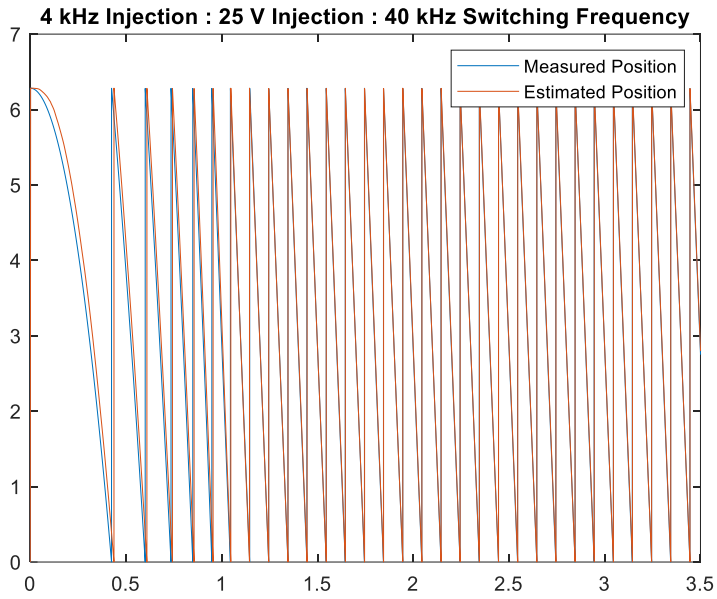

Figure A.17. 4 kHz, 300 RPM at 40 kHz Switching: Position Data

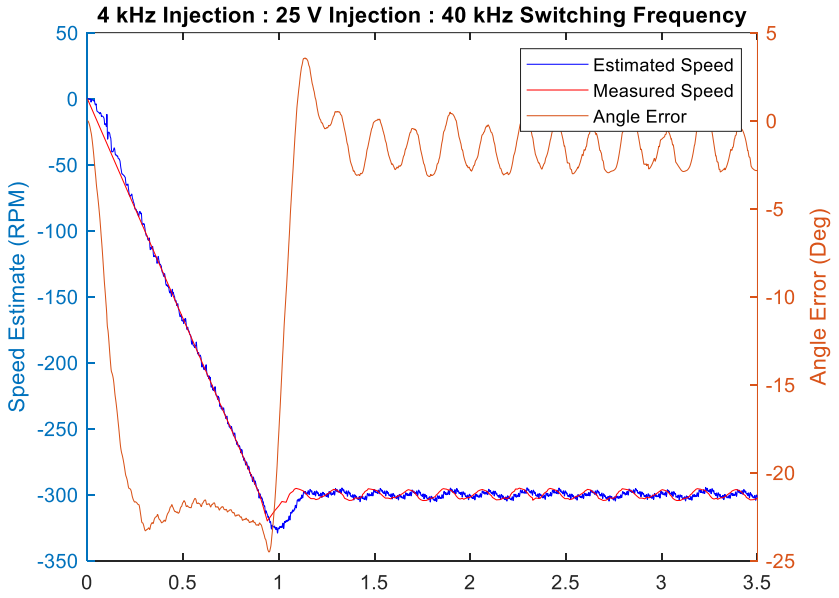

Figure A.18. 4 kHz, 300 RPM at 40 kHz Switching: Speed and Angle Error

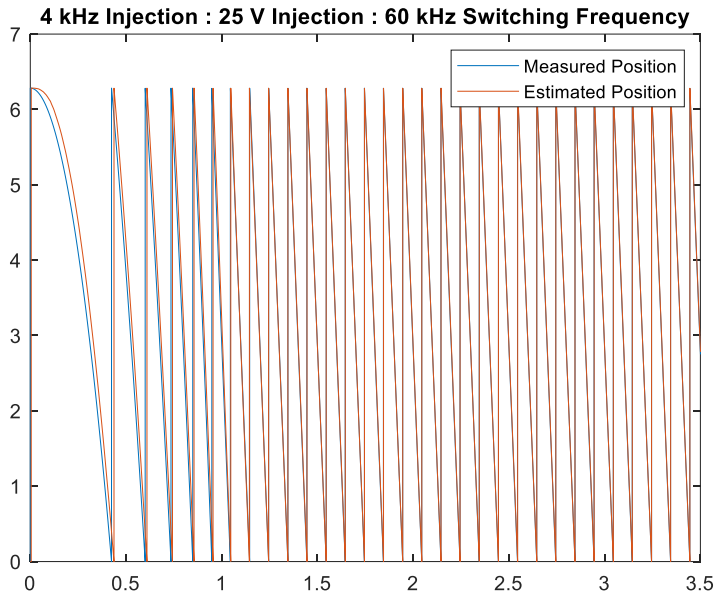

Figure A.19. 4 kHz, 300 RPM at 60 kHz Switching: Position Data

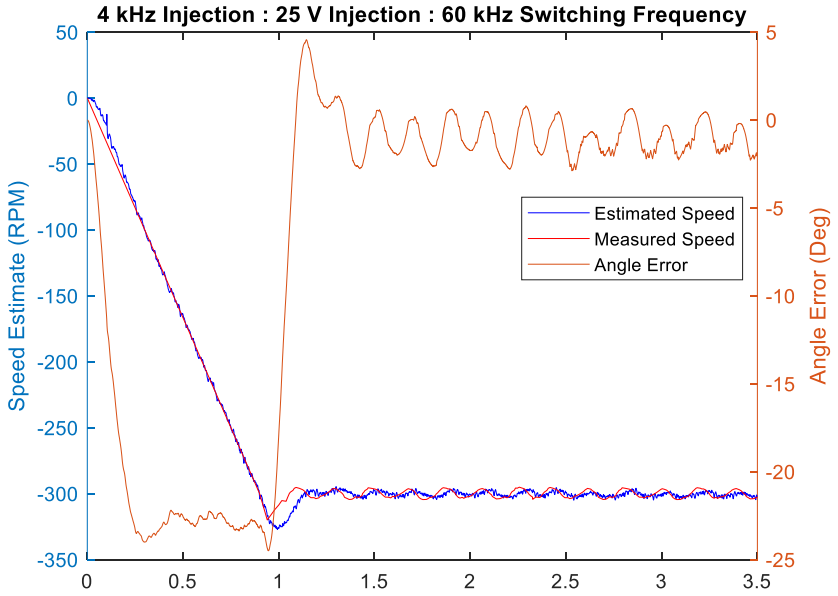

Figure A.20. 4 kHz, 300 RPM at 60 kHz Switching: Speed and Angle Error

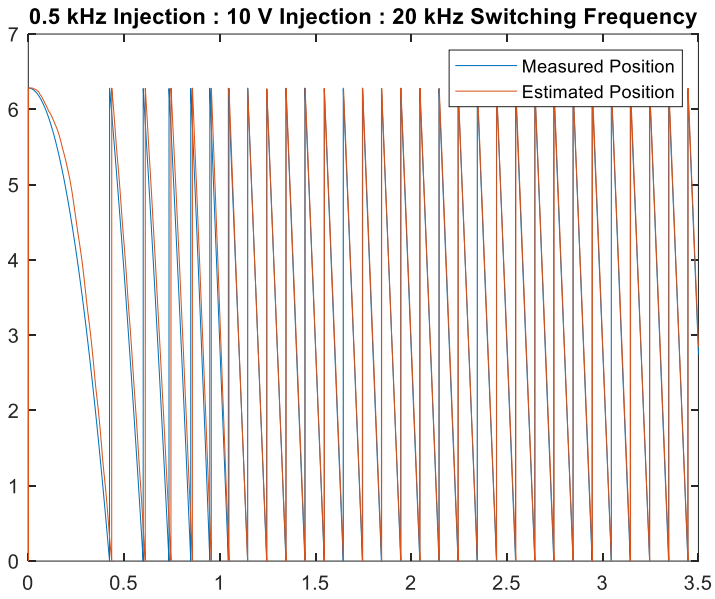

Figure A.21. 500 Hz, 10V Injection, 300 RPM at 20 kHz Switching: Position Data

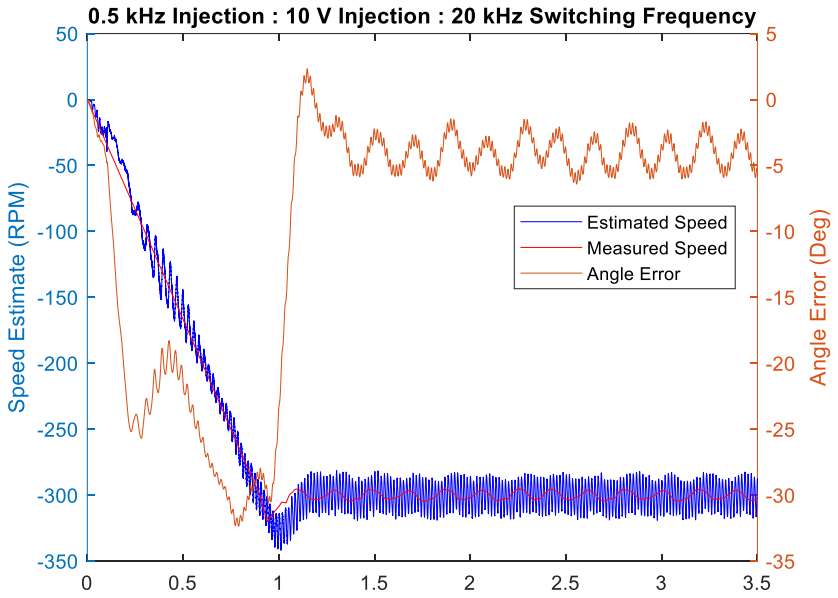

Figure A.22. 500 Hz, 10V Injection, 300 RPM at 20 kHz Switching: Speed and Angle Error

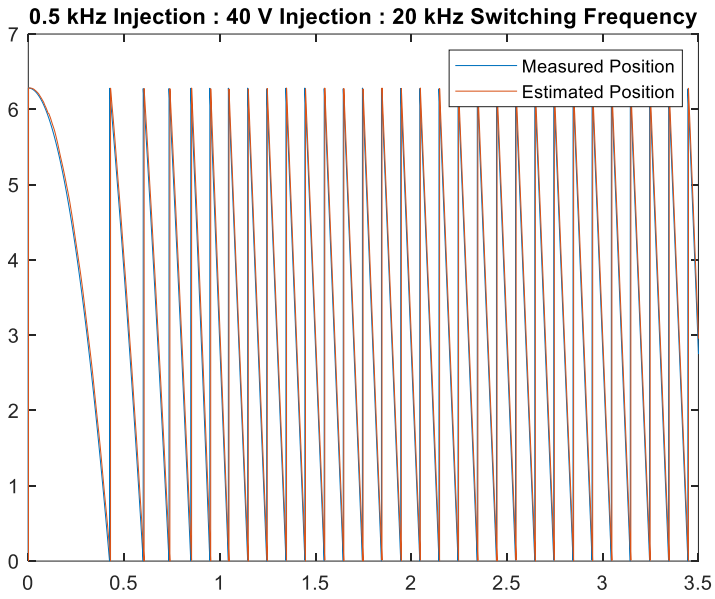

Figure 6. 500 Hz, 40V Injection, 300 RPM at 20 kHz Switching: Position Data

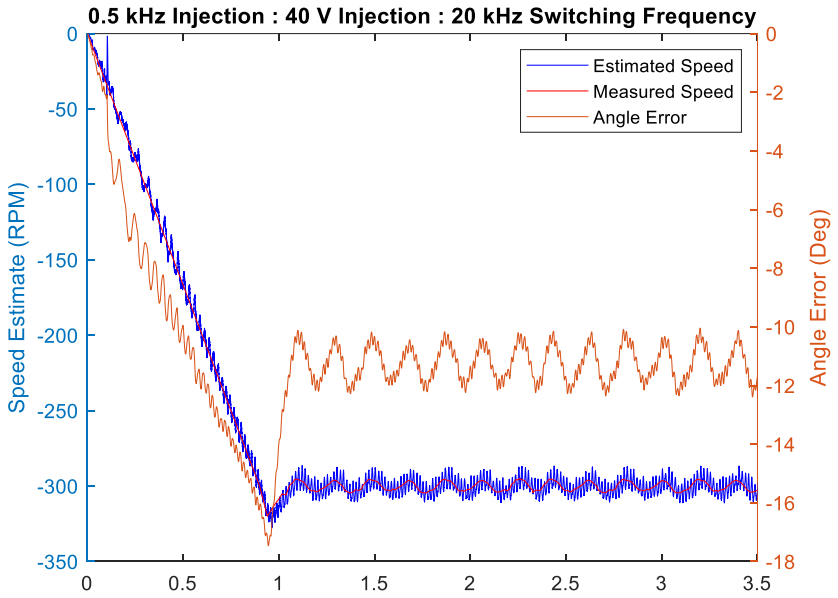

Figure A.23. 500 Hz, 40V Injection, 300 RPM at 20 kHz Switching: Speed and Angle Error

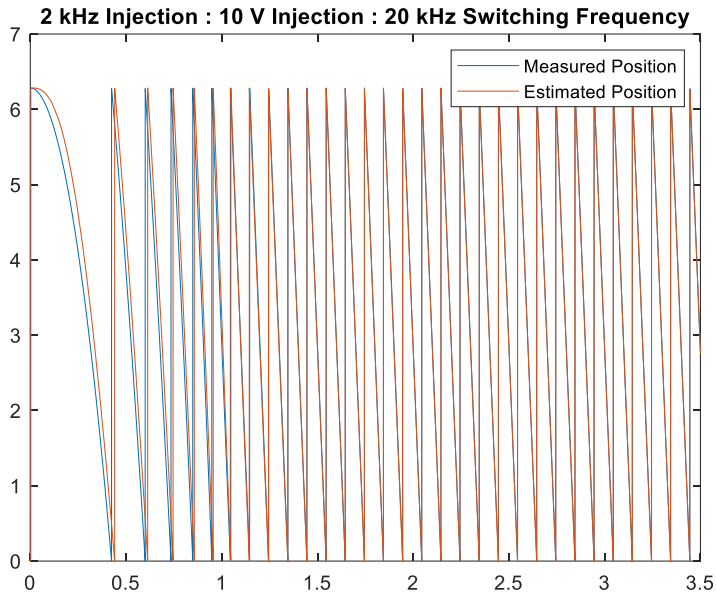

Figure A.24. 2 kHz, 10V Injection, 300 RPM at 20 kHz Switching: Position Data

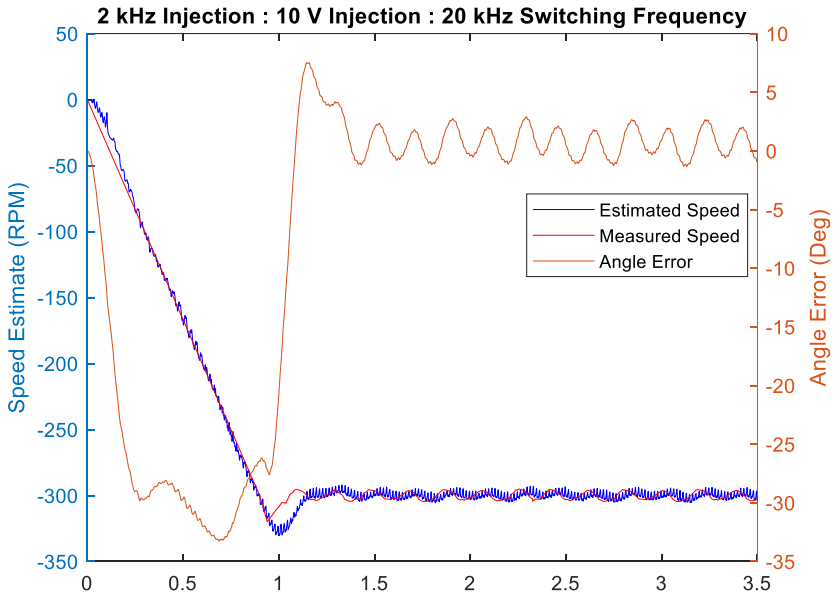

Figure A.25. 2 kHz, 10V Injection, 300 RPM at 20 kHz Switching: Speed and Angle Error

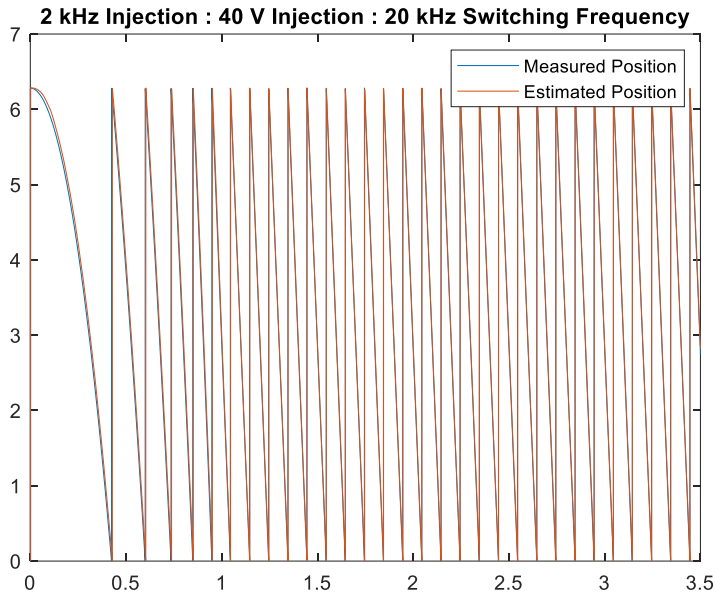

Figure A.26. 2 kHz, 40V Injection, 300 RPM at 20 kHz Switching: Position Data

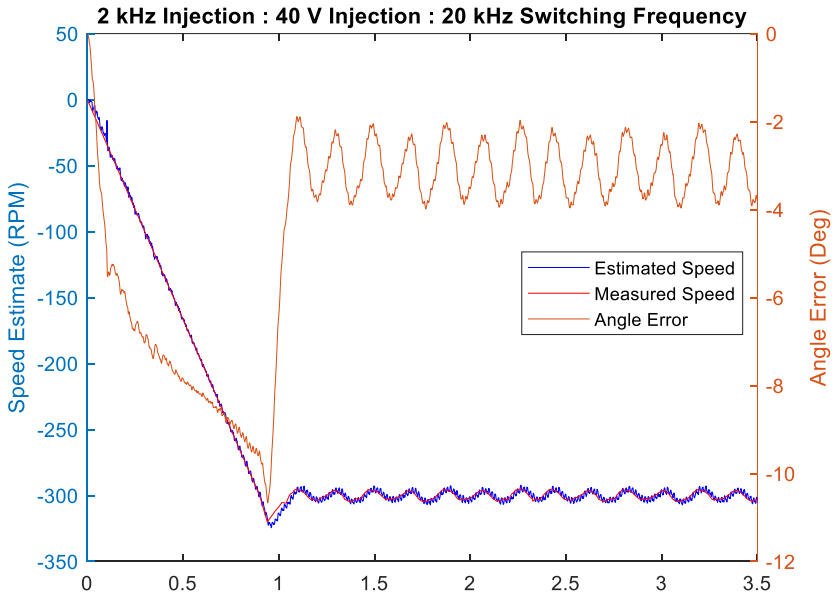

Figure A.27. 2 kHz, 40V Injection, 300 RPM at 20 kHz Switching: Speed and Angle Error

VITA

Jared Walden was born in Bowling Green, Kentucky and raised in Scottsville, Kentucky. He attended Western Kentucky University as an undergraduate. He worked as an undergraduate research assistant in the physics department as a freshman and sophomore. During his sophomore and junior year, he worked as an electrical engineering intern at Heath-Zenith. As a senior undergraduate, he worked as an undergraduate research assistant at the Center for Energy Systems, located at Western Kentucky University. Upon graduation, he accepted a position as a research engineer at the Center for Energy Systems for one year.

Jared accepted a graduate research assistantship under Dr. Hua Bai through the Wide Bandgap Traineeship as he pursued his Master of Science degree. Throughout his time as a graduate student, he researched motor control strategies. After graduation, he plans to stay in Knoxville and work as a power electronics engineer at Oak Ridge National Laboratory.